POLITECNICO DI TORINO

Master of Science
in Electronics Engineering

Master's Thesis

Nanoscale simulation of the Atomic Layer Deposition process of Hafnium Dioxide

Supervisor
Prof. Gianluca PICCININI
Co-supervisors
Yuri ARDESI, *Ph.D.*
Fabrizio MO, *M.Eng.*
Chiara Elfi SPANO, *M.Eng.*

Candidate
Duc Tan TRAN

Academic Year 2022 - 2023

Abstract

Miniaturisation has been the driving force of the microelectronics industry for the past few decades to achieve more powerful devices. Scaling rules indicate that as the transistor's channel length is shortened, the gate oxide thickness must also shrink to maintain the electrostatic control of the gate stack while mitigating undesired short-channel effects. However, a thinner insulator layer between the gate and the channel risks amplifying the gate tunnelling current, and thus, increases the power consumption and deteriorates the reliability of the device. Therefore, scaled-device manufacturers have switched to utilising high permittivity materials, for example, hafnium dioxide or zirconium dioxide, in substitution of silicon dioxide as the gate dielectrics to prevent excessive gate currents.

Furthermore, the downsizing of the gate oxide brings new challenges to film deposition technologies. Traditional vapour deposition techniques either suffer from poor conformality and thickness control of the film or are performed at high temperatures, which exacerbates short-channel effects by diffusing the doping profile near the channel region. Therefore, Atomic Layer Deposition (ALD) was introduced as a superior solution. By building thin films one atomic layer at a time, ALD attains a very uniform, conformal and nanometre-precise film.

There have been many experimental studies into the ALD process of hafnium dioxide. Nonetheless, computer simulations of this process remain little known, leaving a gap between experiments and mathematical models. In this thesis, a novel reactive force field was developed to describe interactions between five atom types Si/O/H/Hf/Cl. Then, the same force field was employed to perform Molecular Dynamics (MD) simulations of the growth process. The Growth per Cycle (GPC) obtained from the simulation was 1.42 Hf/nm^2, which is in good agreement with experimental data. Observations from the simulation also confirmed the theoretical growth mechanism of the ALD process.

Lastly, the deposited HfO_2 film was characterised by its electrical properties. Technology Computer-Aided Design (TCAD) simulations of a scaled transistor with a High-κ/Metal-gate (HKMG) stack were conducted, which demonstrated an improved performance over the conventional silica gate oxide.

Acknowledgements

I would like to express my deepest gratitude to my supervisor, *Prof.* Gianluca Piccinini, for his indispensable guidance and support during the course of this work. His expertise, patience, and inspiration encouraged me to complete and write this thesis.

I would also like to give my thanks to Yuri Ardesi, Fabrizio Mo, Chiara Elfi Spano, and Federico Ravera, for dedicating their time and effort as my co-supervisors, and for providing valuable suggestions and feedback. Without them, I would have not been able to finish this work.

I particularly thank the VLSI Lab at the Department of Electronics and Telecommunication, Politecnico di Torino for allowing me to use their resources to carry out this work.

I also sincerely thank all professors at the Politecnico di Torino who have instructed me throughout my master's program and equipped me with the necessary skills and knowledge to do this thesis.

I am grateful to my friends at the Politecnico di Torino, from the Alta Scuola Politecnica program, and also to friends I met off-campus, for they have become an important part of this chapter of my life and helped with my physical and mental wellness.

My sincere gratitude also goes to my family - my father, mother, and brother - for their unconditional understanding and support from the beginning of this enduring journey.

Lastly, from the bottom of my heart, I would like to show my appreciation to my girlfriend, Tiff, who has been by my side through the most difficult times; who has always believed in me and motivated me to move forward. And to our doggie, *Bò*, 'You will never be forgotten'.

Acronyms

ALD Atomic Layer Deposition.

CI-NEB Climbing-image Nudged Elastic Band.

CMA-ES Covariance Matrix Adaptation Evolution Strategy.

CMOS Complementary Metal-Oxide-Semiconductor.

CVD Chemical Vapour Deposition.

DFT Density Functional Theory.

EAM Embedded Atom Model.

ECP Effective Core Potentials.

EOT Equivalent Oxide Thickness.

FET Field Effect Transistor.

GGA Generalised Gradient Approximation.

GPC Growth per Cycle.

GUI Graphical User Interface.

HKMG High-κ/Metal-gate.

IEEE Institute of Electrical and Electronics Engineers.

IRDS International Roadmap for Devices and Systems.

LAMMPS Large-scale Atomic/Molecular Massively Parallel Simulator.

LDA Local-density Approximation.

MD Molecular Dynamics.

MLIP Machine-Learned Interatomic Potentials.

MOS Metal-Oxide-Semiconductor.

PBC Periodic Boundary Conditions.

PBE Perdew-Burke-Ernzerhof.

PEALD Plasma-Enhanced Atomic Layer Deposition.

PES Potential Energy Surface.

PVD Physical Vapour Deposition.

RMG Replaced Metal Gate.

SC-1 Standard Clean 1.

SS Sub-threshold Swing.

TCAD Technology Computer-Aided Design.

TST Transition State Theory.

Contents

List of Figures

List of Tables

Chapter 1

Introduction

Over the past few decades, we have been witnessing enormous improvements in the computational power and memory capacity of electronic devices. Thanks to the advancement in microelectronics, a mobile phone is now stronger and faster than a computer from ten years ago; a coin-sized storage card can hold more data than a full-sized hard drive; a modern video camera can even perform on-the-spot facial recognition and real-time training of its Artificial Intelligence model, which was impossible in the past. There is still a myriad of applications in which microelectronics has permeated and become a crucial part of our life.

The guideline for the advancement of microelectronics has been the prediction by Gordon Moore in 1965, in which he said that the number of components on a microchip would double every 18 to 24 months. The IEEE International Roadmap for Devices and Systems (IRDS) in 2022 still articulates that, by the end of this decade, the minimum feature size of the Complementary Metal-Oxide-Semiconductor (CMOS) technology will continue to shrink as stated by Moore's law, before reaching physical limits. Any further improvement in functionality can only be made by three-dimensional power scaling, or by switching to other technologies [1].

1.1 Gate dielectrics scaling

Following the scaling rule of CMOS devices, the thickness of SiO_2 gate oxide has been constantly reduced over the years. It has gone from $300nm$ at the $10\mu m$ technology node down to less than a nanometre at the $45nm$ node. In fact, it is the first feature size of the MOSFET (Metal-Oxide-Semiconductor Field Effect Transistor) that has entered the atomic regime.

The main reason for this aggressive scaling is to combat short-channel effects [2]. When the channel is shortened, the threshold voltage of the device also decreases due to a phenomenon called *Roll-off*. Since the off-state leakage current increases at an exponential rate as the threshold voltage decreases, short-channel devices would have unacceptably large leakage current and power dissipation. Thus, to tackle *Roll-off*, the gate oxide capacitance must be raised to compensate for the scaling factor of the channel length. In a MOSFET device, the gate oxide capacitance can be computed as a parallel-plate capacitance:

$$C = \frac{\kappa \epsilon_0}{t},$$

where κ is the relative permittivity of the dielectric material, t is the thickness of the dielectric layer, and ϵ_0 is the permittivity of free space. Hence, the easiest way to amplify the capacitance is to reduce the oxide thickness. However, this solution comes with several challenges.

1.1.1 Limitations of Silicon Dioxide

Experimental results have found that the thinnest layer of SiO_2 to be considered a bulk material is approximately 7Å, which corresponds to four layers of Si atoms across the dielectric. For any layer thinner than this, the influence of interfacial Si atoms between the substrate and the oxide becomes more pronounced. Oxide traps are introduced around the conduction band energy levels of the substrate, drastically lowering the dielectric's potential barrier [3]. This effect makes the gate dielectric conductive, i.e., electrons can easily tunnel through the oxide layer, resulting in a substantial leakage current. Therefore, the down-scaling of SiO_2 gate oxide could never surpass the physical limit of 7Å.

Although the thickness of ultra-thin SiO_2 film can reach the sub-nanometre regime in theory, its technologically achievable thickness is quite larger. Conventionally, SiO_2 film is grown on Si substrates by thermal oxidation or Chemical Vapour Deposition (CVD) process. Both these processes are performed at very high temperatures and with poor control over the thickness and uniformity of the film. For thicker oxide, the film thickness fluctuation obtained from these processes only accounts for a small fraction of the total thickness and is still within the acceptable limit. However, as oxide dimensions shrink, the fluctuation becomes greater than 8% - 10% of the total thickness, which is too large to be considered usable [4].

Reliability is also a major issue concerning ultra-thin SiO_2 film. At around $3nm$ thick, direct tunnelling starts to occur through the oxide barrier, which gives rise to the gate leakage current of MOSFETs. At $1.5nm$ thick, the gate current has reached the value of $10A/cm^2$ [5], which is the largest gate current accepted for low-power devices. Since the tunnelling transmission coefficient scales exponentially as the barrier width decreases [6],

further downsizing of the oxide thickness would make the gate current eventually exceed the upper limit of $1{,}000 A/cm^2$ for high-performance devices. Additionally, ultra-thin gate oxide also accounts for higher interface trap density and trapped charges, contributing to the threshold voltage fluctuation. Devices having up-shifted threshold voltage suffer from lower saturation currents, while ones with down-shifted threshold voltage experience more stand-by power dissipation due to higher leakage currents.

Those limitations in the advancement of the CMOS technology could be addressed by taking two approaches: adopting new materials with a higher dielectric constant for gate dielectrics and employing deposition techniques with better control of the film's thickness.

1.1.2 High-κ dielectrics

Another solution to scale up the gate oxide capacitance without cutting its thickness too aggressively is to substitute SiO_2 with a dielectric material having higher relative permittivity. If t_{hk} is the thickness of the high-κ dielectrics, then Equivalent Oxide Thickness (EOT) is defined as the thickness of the SiO_2 layer to obtain the same capacitance [7]:

$$EOT = \frac{\kappa_{SiO_2}}{\kappa_{hk}} \cdot t_{hk} = \frac{3.9}{\kappa_{hk}} \cdot t_{hk}\,.$$

Early work has found structures such as oxynitrides or oxide/nitride stacks that provide slightly higher κ values than SiO_2 (pure Si_3N_4 has $\kappa \approx 7$). Such material can achieve an EOT of $1.5nm$ with the gate current density around $10^{-3} A/cm^2$ at $1.0V$ bias [8]. However, because the dielectric constant is not so high, achieving less than $1.3nm$ EOT with these materials is impractical.

Several other high-κ materials were proposed, especially for memory applications, such as tantalum oxide (Ta_2O_5), strontium titanate ($SrTiO_3$), or aluminium oxide (Al_2O_3). Although having high dielectric constant values of up to 80, these materials are known to be thermodynamically unstable when deposited directly on Si, and may even react with Si to form undesirable species. Thus, they have not been widely used in CMOS technology.

Recently, zirconium dioxide (ZrO_2) and hafnium dioxide (HfO_2) have emerged as the most promising candidates for SiO_2 alternatives. Both ZrO_2 and HfO_2 have a decent dielectric constant (around 20). They also possess a relatively large band gap with good band offsets with respect to Si [9]. More importantly, ZrO_2 and HfO_2 have been proven to be thermally stable when deposited on Si substrates. At the EOT of $1.2nm$, gate current density as low as $10^{-3} A/cm^2$ at $1.0V$ gate voltage was observed [10].

Among many deposition techniques to grow high-κ dielectrics onto Si substrates, Atomic Layer Deposition (ALD) has been chosen over Chemical Vapour Deposition (CVD)

or Physical Vapour Deposition (PVD) as the primary method thanks to its excellent quality in dealing with ultra-thin film. Briefly speaking, ALD is a process based on the self-extinguishing reaction principle, where only one reactant species is introduced to the surface at a time. Thus, the film can be grown very precisely and uniformly, one mono-layer by one mono-layer. The superb control over the film thickness is crucial in manufacturing extremely thin gate oxide in scaled devices. Furthermore, ALD can be performed at very low temperatures, making it even more compatible with sub-micron CMOS fabrication process.

There have been numerous experimental studies into the ALD of high-κ materials; however, computer simulations of the film growth remain limited. Therefore, in this thesis, I would like to gain more insights into the deposition of HfO_2 gate oxide on Si substrates, as well as investigate its impact on the performance of highly-scaled MOSFET devices.

1.2 Structure of the thesis

This thesis is divided into 7 chapters:

Chapter 1 provides an overview of the technological trend in the microelectronics sector, as well as the objectives of the thesis.

Chapter 2 and Chapter 3 give background knowledge about the Atomic Layer Deposition (ALD) technology and the computational methods that are used in this thesis.

Chapter 4 explains the procedure employed to develop an empirical force-field tailored for the ALD process. This force-field is required to carry out molecular mechanics simulations.

Chapter 5 discusses the MD simulation setup and results of the ALD process of HfO_2 on Si substrates.

Chapter 6 describes the characterisation of the deposited high-κ film to extract its physical and electrical properties. Device simulations are also performed to verify the influence of high-κ materials on device characteristics.

Chapter 7 is conclusions and future outlook.

Chapter 2

The Atomic Layer Deposition technology

Atomic Layer Deposition (ALD) has recently become the norm in the semiconductor industry for growing thin films of various materials. As its name suggests, ALD is a deposition technique that grows films atomic layer by atomic layer.

The advantages of ALD over other deposition techniques are the superb conformality and uniformity of the film, as well as the ability to control the film's thickness precisely – down to a mono-layer of atoms. These advantages are crucial as semiconductor devices are continuously miniaturised. Nowadays, the thickness of the gate oxide of scaled CMOS transistors is on the order of $2nm$, which means a 10%-tolerance corresponds to the acceptable thickness variation of around 2Å to 3Å. Control of such small thicknesses of one layer of atoms can only be achieved with ALD [11]. Additionally, ALD is performed at a lower temperature than the Chemical Vapour Deposition (CVD) process, making it more suitable for processes with a low thermal budget, especially in scaled devices where strict diffusion profile control and shallow junction are required to minimise short-channel effects.

2.1 ALD process

ALD meets a high standard of conformal deposition and atomic layer control by exploiting self-limiting surface reactions. Virtually all ALD processes are carried out in pulsed mode, which is the alternation of precursor phases and purge phases until the film reaches the desired thickness. In each precursor phase, a reactive gas is introduced around the substrate, which then is chemisorbed at suitable sites on the surface. Since the number of reactive

sites on the surface is finite, once the adsorbates have saturated the surface, the reaction immediately stops, preventing the growth of more than one mono-layer. Therefore, sequences of these self-extinguishing reactions result in a very uniform and conformal layer of material deposited on the substrate's surface. Furthermore, purge phases in between two half-reactions separate two reactive gases to avoid gas phase reactions, eliminating unwanted species during the deposition process. Figure 2.1 illustrates one cycle of a general ALD process step-by-step. This procedure is carried out iteratively until a film with the desired thickness is achieved.

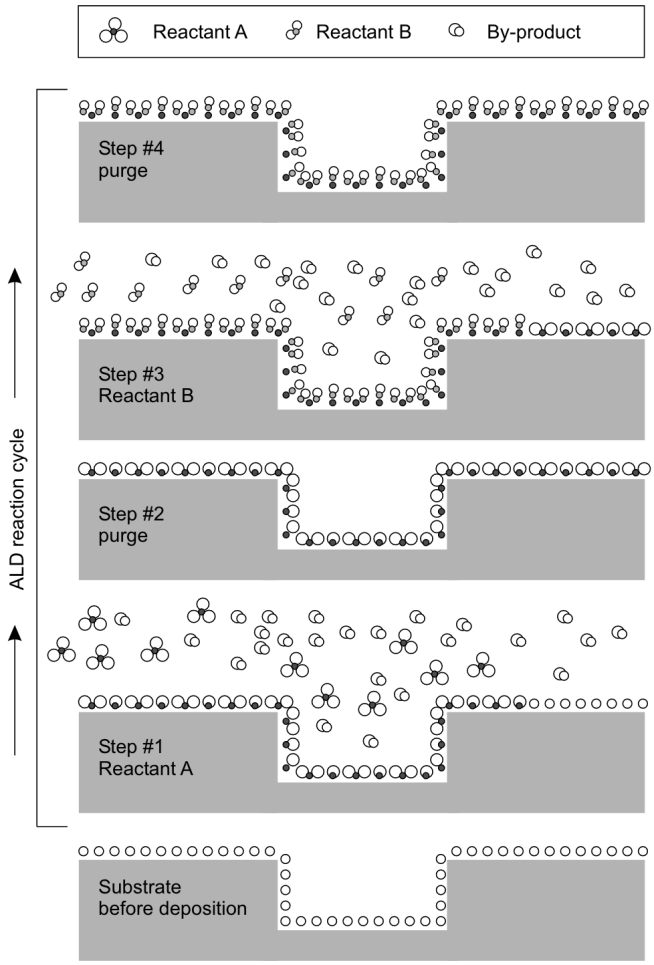

Figure 2.1 *Procedural schematic of the ALD process in one cycle [12].*

On the other hand, ALD suffers from a remarkably low growth rate due to its sequential nature. Typically, the ALD growth rate ranges from 0.1Å to a few ångström per cycle, depending on the deposited material, the precursors, and the deposition conditions. Nonetheless, because the thickness of thin films in modern microchips is usually small, the

total deposition time is not too long to achieve the desired thickness. Therefore, ALD's low growth rate is overshadowed by its superior advantages, making it the prominent deposition technology in the future of the semiconductor industry.

Ideally, the Growth per Cycle (GPC) is constant and equals one mono-layer of the desired atom no matter how long the precursor exposure is due to its self-limiting nature, as depicted in Figure 2.2. This leads to a linear growth as the number of cycles increases. However, in most cases, the interplay between reactivity, the number of surface sites, and steric hindrance[1] can lead to a slower or faster growth rate than the ideal value. They are referred to as substrate inhibition growth and substrate enhancement growth, respectively, in Figure 2.3.

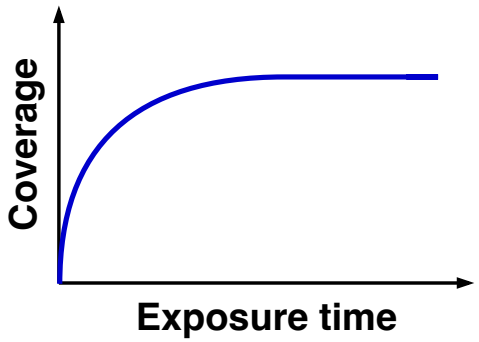

Figure 2.2 *Deposited film coverage versus exposure time.*

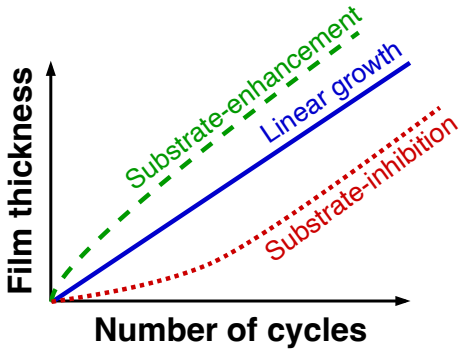

Figure 2.3 *Three types of thin film growth in an ALD process.*

Temperature is also an important factor that influences the GPC. The temperature dependency of the GPC is summarised in Figure 2.4. Every ALD process has a temperature range, called the ALD window, where conditions for self-limiting reactions are satisfied, and the controlled growth rate is approximately one mono-layer. Inside the ALD window, the GPC may equal a constant value when steric hindrance is the dominant surface-saturating phenomenon. In contrast, if the number of adsorbates depends largely on the number of reactive surface sites, the GPC slightly decreases with temperature because reactive sites are likely to dissociate from the surface as temperature increases. If the deposition is performed out of the ALD window, several cases can happen:

- Lower temperature, lower GPC: thermal energy is not high enough to provide sufficient kinetics to finish all chemical reactions on the surface.

[1]Steric hindrance is the phenomenon in which the adsorbed molecule, due to its size, physically inhibits other molecules from attaching to nearby surface sites.

- Lower temperature, higher GPC: the adsorption mechanism is not chemisorption, but weaker physisorption. Physisorption does not exhibit self-limiting behaviours; therefore, the grown film is multi-layered and non-conformal.
- Higher temperature, lower GPC: the products of the self-limiting reactions desorb from the surface due to very fast kinetics.
- Higher temperature, higher GPC: the precursors may be decomposed into other species, which induces more complex reactions on the surface.

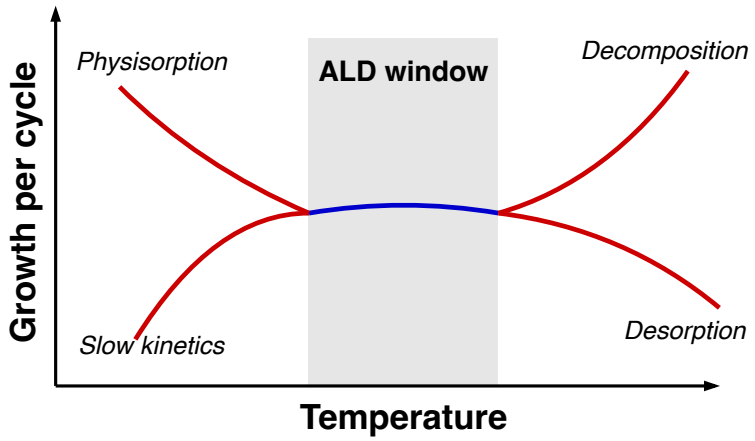

Figure 2.4 *Temperature dependency of the ALD technology.*

Many elements and their compounds can be deposited with ALD. For example, ruthenium (Ru), copper (Cu), and tungsten (W) are three metals that are ALD-compatible; while semiconductor materials, such as silicon (Si) and germanium (Ge), can also be grown using ALD. Some of the most important compounds for microelectronics applications have already been deposited with ALD, namely aluminium oxide (Al_2O_3) and hafnium dioxide (HfO_2) as high-κ gate dielectrics for CMOS transistors, or titanium nitride (TiN) as diffusion barrier layers for metal interconnects.

2.2 ALD precursors

Searching for suitable chemical precursors for those materials is not a trivial task since there are several requirements for precursors to make the ALD process feasible. ALD precursors must have sufficient volatility, high purity, high reactivity versus surface groups, and good thermal stability. They must also be non-corrosive to the substrate or the deposited film, and non-reactive versus by-products. A precursor with sufficient volatility has an adequate vapour pressure so that its molecules can saturate the surface within a practical cycle time, enabling excellent step coverage even for structures with higher

aspect ratios. The high purity and high reactivity properties ensure that no impurities and unreacted ligands, which are detrimental to electronic devices, remain in the film after each cycle. Finally, a thermally stable precursor at ALD temperatures prevents the decomposition of surface species during the surface reaction; thus, it minimises the possibility of sub-mono-layer growth, which in turn produces a non-uniform film. Of course, there are other requirements regarding the economics and safety of a precursor; however, the ones listed are the most important requirements for a precursor suitable for ALD technology [13].

Some of the most common families of precursors which contain metals and their properties are listed in Table 2.1. Precursors that source non-metal atoms (often referred to as reactants) are more limited in numbers, such as water vapour (H_2O), hydrogen peroxide (H_2O_2), or ozone (O_3) as a source of oxygen (O); ammonia (NH_3) as a source of nitrogen (N); acetylene (C_2H_2) or formic acid (HCOOH) as a source of carbon (C); hydrogen sulphide (H_2S) as a source of sulphur (S); etc. In some advanced ALD processes like Plasma-Enhanced Atomic Layer Deposition (PEALD), hydrogen radicals generated in plasma can be used as high-energy reactants.

2.3 ALD of Hafnium Dioxide

Among many precursors that can be used to deposit hafnium dioxide (HfO_2) film, hafnium tetra-chloride ($HfCl_4$) and water (H_2O) are the two most well-known substances: $HfCl_4$ serves as the metal precursor and H_2O is the oxygen source. In the most simplistic way, the mechanism of the ALD process of HfO_2 from $HfCl_4$ and H_2O can be summarised by two half-reactions [14]:

(1)
$$\mathrm{Si(OH)_n + HfCl_4 \longrightarrow SiO_nHfCl_{4-n} + n\ HCl}$$

(2)
$$\mathrm{SiO_nHfCl_{4-n} + (4-n)\ H_2O \longrightarrow SiO_nHf(OH)_{4-n} + (4-n)\ HCl}$$

In the first half-reaction, hydroxyl groups on the surface (usually present after surface treatments) exchange hydrogen atoms with chlorine atoms of the $HfCl_4$ molecule to form HCl gas products. The number n can take any integer value from 1 to 4, meaning that the $HfCl_4$ molecule may have only one or all four of its chlorine atoms reacted. In the case $n = 4$, the surface reaction stops immediately.

In the second half-reaction, oxygen-transfer reactions occur between H_2O and the Hf-containing surface species. O atoms from water attach to the surface Hf atom, forming a new layer of hydroxyl groups and releasing HCl gases. After the second half-reaction,

a new mono-layer of HfO_2 has been grown on the surface. The next ALD cycle would start on top of the newly-formed OH groups. The illustration of the two half-reactions is shown in Figure 2.5.

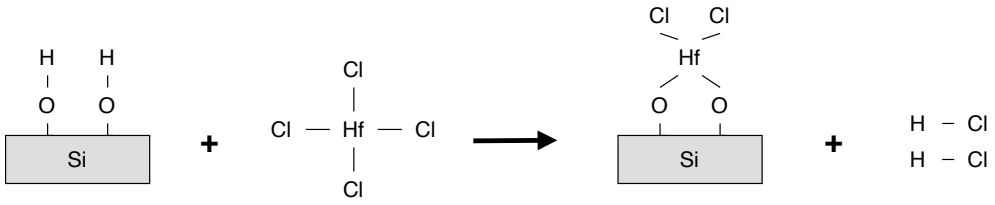

(a) *First half-reaction*

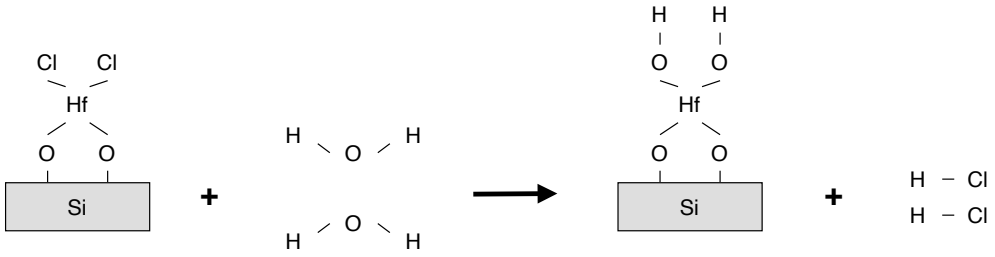

(b) *Second half-reaction*

Figure 2.5 *Illustration in the case $n = 2$ of the (a) first half-reaction and (b) second half-reaction of the ALD process of* HfO_2 *from* $HfCl_4$ *and* H_2O.

Table 2.1 *Common ALD precursors and their properties.*

Precursors / Properties	**Halides**	**Ankyls**	**Ankylamides**	**beta-diketonates**	**Ankoxides**
Example	$HfCl_4$, $ZrCl_4$	TMA, DEZ	BDEAS, TDMAT		ATIP, TEOS
Cost	Cheap	Moderate	Expensive	Expensive	Cheap
Reactivity	Moderate	High	High	Low	Moderate
Thermal stability	Very high	High	Moderate	Moderate	Moderate
Impurity	Low	Low	Low	Moderate	Moderate
Safety	Corrosive	Pyrophoric	Pyrophoric, flammable	Limited	Limited

Chapter 3

Computational methods for ALD modelling

Computational methods are extremely useful to study many quantum chemistry problems without conducting experiments or the need for advanced equipment. They are often computer programs that are equipped with mathematical models and algorithms to predict atomic and molecular structures and properties, as well as information about various quantum processes. The ALD process involves many chemical reactions and molecular formations/deformations, and thus, the use of computational chemistry tools is reasonable. In this chapter, two widely-known computational methods, which will be employed to model the ALD of HfO_2, Density Functional Theory (DFT) and Molecular Dynamics (MD), are briefly introduced.

3.1 Density Functional Theory

Density Functional Theory (DFT) is a quantum mechanical modelling method used to examine the electronic structure of atomic, molecular, or condensed-phase many-body systems. DFT differs from other exact *ab initio* methods because it does not directly solve the many-electron Schrödinger equation to obtain the complete wave function, but it approximates the electronic structure of the system in terms of one-electron Hamiltonian by introducing the concept of electron density.

For a system of M nuclei and N electrons, the electron density $n(\mathbf{r})$ is defined by:

$$n(\mathbf{r}) = N \int \cdots \int |\Psi(\mathbf{r}, \mathbf{r}_2, \ldots, \mathbf{r}_N)|^2 \, d^3\mathbf{r}_2 \ldots d^3\mathbf{r}_N \,, \tag{3.1}$$

which signifies the probability of finding any of the N electrons at position $\mathbf{r}$. Thus, the integral all over space of the electron density equals the total number of electrons:

$$\int n(\mathbf{r})d\mathbf{r} = N\,. \tag{3.2}$$

According to the Hohenberg-Kohn theorem [15], there is a unique one-to-one correspondence between an electron density function and a wave function, including the ground-state density n_0. Then, Ψ can be considered a *functional*[1] of n:

$$\Psi_0 = \Psi[n_0]\,. \tag{3.3}$$

The Hohenberg-Kohn theorem also states that the energy of a system is also a *functional* of the electron density, and only the ground-state electron density can yield the ground-state energy of the system:

$$E_0 \leq E = E[n] = T[n] + U[n] + V[n]\,, \tag{3.4}$$

where

$$V[n] = \int n(\mathbf{r})V(\mathbf{r})d\mathbf{r} = \int n(\mathbf{r}) \left[-\frac{q^2}{4\pi\epsilon_0} \sum_i^N \sum_j^M \frac{Z_j}{\|\mathbf{r}_i - \mathbf{r}_j\|} \right] d\mathbf{r} \tag{3.5}$$

is the system-dependent component, while $T[n]$ and $U[n]$ are universal *functionals* for every system.

In Equation 3.4, $T[n]$ represents the kinetic energy of the system, and it can be decomposed into a non-interacting component T_S and a residual component T_C:

$$T[n] = T_S[n] + T_C[n]\,. \tag{3.6}$$

On the other hand, $U[n]$ represents the electron-electron interactions inside the system, which contains a Coulomb repulsion contribution J and a non-classical contribution E_{ncl}:

$$U[n] = J[n] + E_{ncl}[n] = \frac{1}{2} \iint \frac{n(\mathbf{r}_1)n(\mathbf{r}_2)}{\|\mathbf{r}_1 - \mathbf{r}_2\|} d\mathbf{r}_1 d\mathbf{r}_2 + E_{ncl}[n]\,. \tag{3.7}$$

Thus, the total energy of the system becomes:

$$\begin{aligned} E[n] &= T_S[n] + T_C[n] + J[n] + E_{ncl}[n] + V[n] \\ &= T_S[n] + J[n] + V[n] + E_{XC}[n]\,, \end{aligned} \tag{3.8}$$

[1] A functional is defined as a function of functions.

in which $E_{XC}[n] = T_C[n] + E_{ncl}[n]$ contains all elements without an explicit form and is called the *exchange-correlation* energy. The ground-state energy of the system is determined by numerically solving for the eigenvalue of the one-electron Kohn-Sham Hamiltonian:

$$\mathcal{H}_{1el} = -\frac{\hbar^2}{2m}\nabla^2 + V^{\text{eff}}[n](\mathbf{r})\,, \tag{3.9}$$

where $V^{\text{eff}}[n] = J[n] + V[n] + E_{XC}[n]$. However, since the exact form of the *exchange-correlation* component is not known, approximations have to be made to permit the calculation of the electronic structure. Some of the most common approximate forms are Local-density Approximation (LDA) [16], Generalised Gradient Approximation (GGA) [17], and meta-GGA. Once the form of every component of the one-electron Hamiltonian is defined, the Kohn-Sham equations can be solved in a self-consistent loop as illustrated in Figure 3.1.

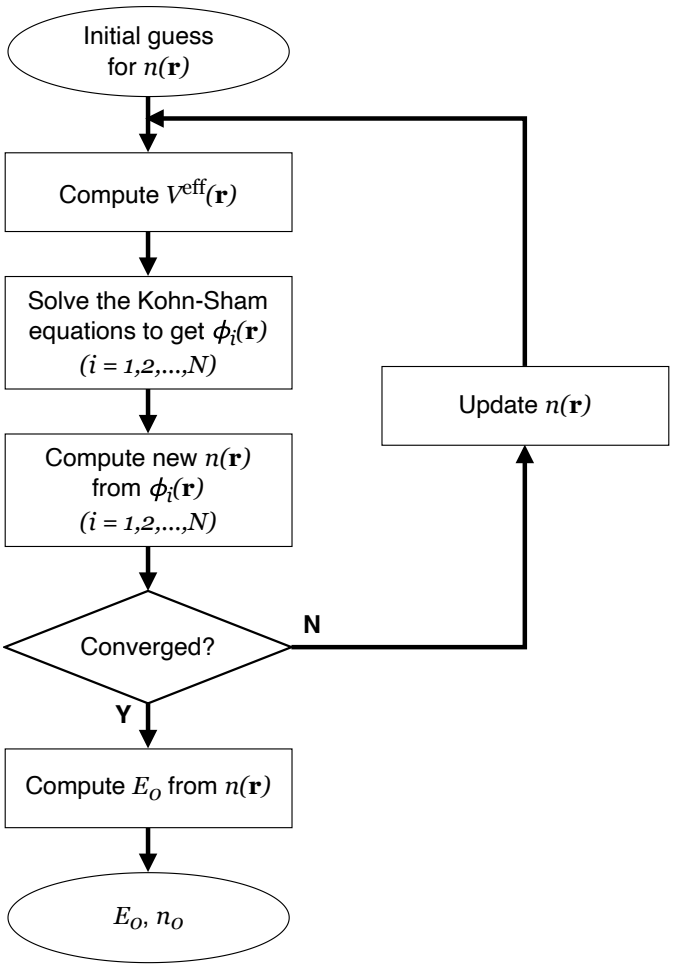

Figure 3.1 *Flowchart of a DFT program.*

Thanks to its ability to generate adequately accurate results with a fraction of computational effort compared to other first-principle methods, DFT has been used extensively among quantum chemistry scientists to compute the electronic structure of various types of systems. Nowadays, almost all *ab initio* software implements the DFT algorithm in their package, such as VASP[2], QuantumATK[3], ORCA[4], etc. In this work, QuantumATK and ORCA will be employed to study the properties of systems of interest. This section is meant only to provide a quick description of the DFT method, in-depth information should be found in more dedicated work on the subject [18, 19, 20].

3.2 Molecular Dynamics

Molecular Dynamics (MD) is a numerical method based on the generalisation of particles inside a system and classical mechanics to describe the system's state with respect to space and time. In essence, MD solves Newton's equation of motion every fixed amount of time, called time-step, to determine the physical interaction among all particles of a system. Thus, MD can provide a good approximation of the dynamic evolution of a system, facilitating studies of various complex processes in physics, chemistry, biophysics, and materials science.

3.2.1 The MD algorithm

For a system with N particles, $\mathbf{r}^N = \{\mathbf{r}_1, \mathbf{r}_2, ..., \mathbf{r}_N\}$ and $\mathbf{v}^N = \{\mathbf{v}_1, \mathbf{v}_2, ..., \mathbf{v}_N\}$ denote sets of vectors that store the coordinate and velocity of all particles. The main goal of an MD simulation is to assess the position and velocity of all particles at any instance of time. This is done by establishing the following iterative routine on the system's particles:

1. **Initialisation**: at the beginning of the simulation, initial position and velocity are assigned to all particles in the system.

2. **Forces computation**: the force that particle j exerts on particle i can be computed by the formula:

$$\mathbf{f}_{ij} = -\nabla_i V(r_{ij})\,, \tag{3.10}$$

   where $V(\cdot)$ is the potential energy function and $r_{ij} = \|\mathbf{r}_j - \mathbf{r}_i\|$ is the pair distance. According to Newton's third law, the force that particle i exerts on particle j has the same magnitude but opposite direction, i.e., $\mathbf{f}_{ji} = -\mathbf{f}_{ij}$. Hence, the interacting

[2] https://www.vasp.at

[3] https://www.synopsys.com/silicon/quantumatk.html

[4] https://orcaforum.kofo.mpg.de/app.php/portal

force has to be computed only once for each pair.

The total force acting on particle i is calculated as:

$$\mathbf{F}_i = \sum_{\substack{j=1 \\ j \neq i}}^{N} \mathbf{f}_{ij} \tag{3.11}$$

3. **Time integration**: for a particle i in the system, Newtonian mechanics states that:

$$\mathbf{F}_i = m_i \ddot{\mathbf{r}}_i = m_i \frac{d^2 \mathbf{r}_i}{dt^2}\,, \tag{3.12}$$

in which m_i denotes the mass of the particle.

At this point, time integration of the position and velocity vectors is performed by implementing numerical computations. The most simple and intuitive numerical method is the first-order Taylor expansion, expressed in the following equations:

$$\mathbf{v}_i(t + \Delta t) = \mathbf{v}_i(t) + \frac{\partial \mathbf{v}_i(t)}{\partial t} \Delta t \tag{3.13}$$

$$\mathbf{r}_i(t + \Delta t) = \mathbf{r}_i(t) + \frac{\partial \mathbf{r}_i(t)}{\partial t} \Delta t \tag{3.14}$$

However, the first-order Taylor expansion has very poor accuracy. Thus, most MD programs nowadays implement more accurate numerical methods, for example, the Verlet algorithm [21]. In the Verlet algorithm, the position of the particle in the next time-step is not computed from the velocity, but from the current and previous position of the particle:

$$\mathbf{v}_i(t) = \frac{\mathbf{r}_i(t + \Delta t) - \mathbf{r}_i(t - \Delta t)}{2\Delta t} \tag{3.15}$$

$$\mathbf{r}_i(t + \Delta t) = 2\mathbf{r}_i(t) - \mathbf{r}_i(t - \Delta t) + \frac{\mathbf{F}_i(t)}{m_i} (\Delta t)^2 \tag{3.16}$$

The velocity at the current time-step is used only to compute the kinetic energy and the instantaneous temperature of the system.

4. **Thermodynamics properties calculation**:

The total potential energy of the system is simply the sum of all pairwise potential energies:

$$U_{tot}(t) = \frac{1}{2} \sum_{i,j} V(r_{ij}) \tag{3.17}$$

The kinetic energy of the entire system is also summed up from the kinetic energy of all N particles:

$$K_{tot}(t) = \sum_{i=1}^{N} \frac{1}{2} m_i \|\mathbf{v}_i(t)\|^2 \tag{3.18}$$

The total energy of the system at any time-step is the sum of potential and kinetic energies:

$$E(t) = U_{tot}(t) + K_{tot}(t) \tag{3.19}$$

The instantaneous temperature of the system at the time-step t is related to the kinetic energy by the following formula, where k_B is the Boltzmann constant:

$$\frac{3}{2} k_B T = K_{tot}(t) \tag{3.20}$$

The pressure of the system can be computed at each time-step using the formula, where V is the volume of the space occupied by the system:

$$P = \frac{N k_B T}{V} + \frac{\sum_{i=1}^{N} \mathbf{F}_i \cdot \mathbf{r}_i}{3V} \tag{3.21}$$

After the time integration step, the position and velocity of every particle in the system have been updated to their new values at time-step $t + \Delta t$. The MD algorithm jumps back to the second step to compute the forces of the new configuration, and eventually, the new position and velocity vectors at time-step $t + 2\Delta t$. The procedure keeps on going until the current time-step reaches the final time-step of the simulation, defined from the initialisation step. The collection of position vectors of the system ordered by time is known as the MD trajectory and can be visualised with suitable software. The procedural diagram of the MD algorithm is illustrated in Figure 3.2.

Ensembles

In the aforementioned MD algorithm, besides the fixed number of particles N and the fixed volume V of the system, the total energy E is considered to be constant. In other words, the system is completely isolated from external entities. This is referred to as the micro-canonical or NVE ensemble. To model processes in the real world, running MD simulations in the micro-canonical is insufficient because we often want to have control of the thermodynamic properties of the system, such as temperature or pressure. Thus, two common non-NVE ensembles have been established: NVT and NPT.

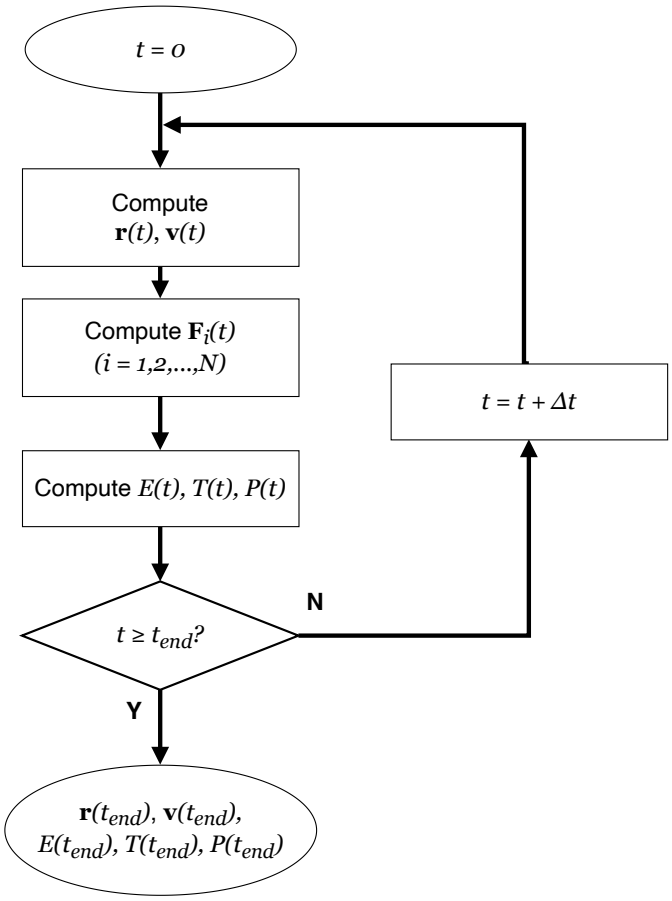

Figure 3.2 *Algorithm flowchart of a MD program.*

The NVT ensemble

The NVT or canonical ensemble allows the system of interest to have a desired temperature by coupling it to a heat bath during the simulation. It can be thought of as the system of interest exchanging kinetic energy with the system representing the heat bath, and the "big" system which comprises the two is in the micro-canonical ensemble. Thus, the average kinetic energy and temperature of the system of interest are maintained relatively constant. Actually, the instantaneous kinetic energy and temperature fluctuate around the average value [22].

The energy exchange with the heat bath is realised by means of a thermostat - an algorithm that modifies the velocity vector of particles in the system to obtain the desired temperature. Some of the most widely-used thermostats are the Andersen thermostat [23], Berendsen thermostat [24], Langevin thermostat, and Nosé-Hoover thermostat [25, 26].

The NPT ensemble

Running MD simulations at a preset volume means that the pressure of the system constantly changes. To maintain a fixed value of the pressure, the role of pressure and volume are swapped: the volume of the system is adjusted through a barostat to keep the pressure constant. In principle, a barostat works similarly to a thermostat, re-scaling or adding extra terms to the instantaneous volume. Some of the common barostats are Berendsen barostat, Hoover barostat, Parrinello-Rahman barostat [27], and Martyna barostat [28]. The NPT ensemble is also named the isothermal-isobaric ensemble.

Periodic Boundary Conditions

For a small-sized system of up to some thousands of particles, interactions among particles in the bulk are often dominated by interactions between particles and the container wall. To limit those effects, Periodic Boundary Conditions (PBC) is imposed on the simulation box. In this case, the simulation box is replicated in every direction to mimic the bulk of particles. Figure 3.3 shows PBC in a 2D simulation, where the primary cell, i.e., the simulation box is surrounded by eight image cells. Each of the cells is open-bounded so that any particle can enter and leave the cell. The number of particles in a cell is, however, constant, because when a particle enters/leaves the cell, its replica leaves/enters the cell from the opposite face.

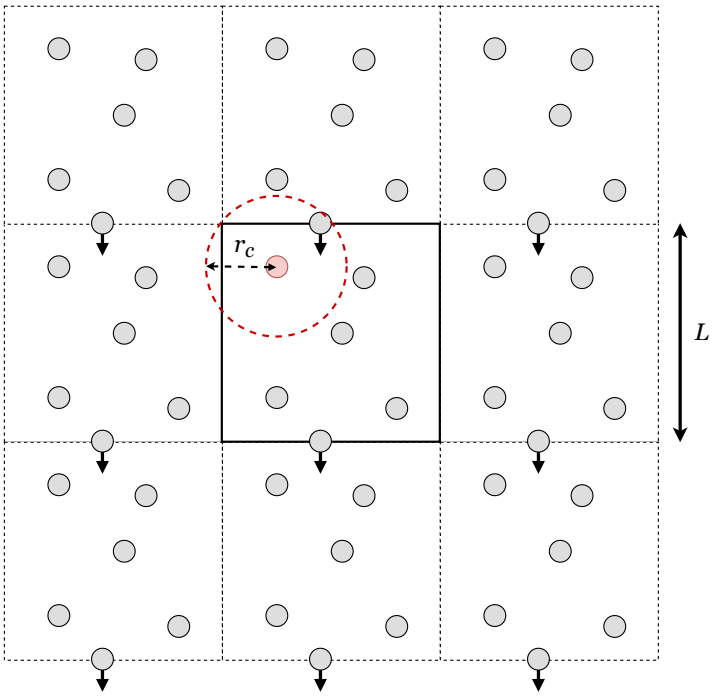

Figure 3.3 *2D Periodic Boundary Conditions in a MD simulation.*

With PBC, every step in the MD algorithm is carried out only in the primary cell. The forces acting on a particle in the primary cell are computed for all neighbouring particles within its cutoff radius r_c, even if the neighbouring particle is a replicated image. Thus, the dimension L of the simulation box must satisfy the condition $L > 2r_c$ to prevent duplicate interactions.

3.2.2 MD software - LAMMPS

LAMMPS (Large-scale Atomic/Molecular Massively Parallel Simulator)[5] is an open-source computer program that can perform dynamic simulations of particle systems [29]. Thanks to its parallelisation and multi-threading support, 2D or 3D systems of up to billions of particles can be efficiently modelled. The main advantage of LAMMPS over other MD software is that it implements various types of force fields and provides a vast number of operations. Its functionality can also be easily modified or extended to meet any specific need, provided the user is familiar with its C++ interface. LAMMPS is also cross-platform, so it can run on the most common computer architectures and many operating systems, e.g., *Linux*, *Windows*, or *macOS*.

LAMMPS does not have a Graphical User Interface (GUI), so every instruction must be given in input scripts. Another downside is that the topology definition feature of LAMMPS is very limited; therefore, molecular systems are usually created with external software and read into LAMMPS.

MD trajectories produced by LAMMPS, known as LAMMPS dump files, can be visualised by several third-party programs. In this thesis, all trajectory files are post-processed with the free version of OVITO[6] [30] because of its fast and user-friendly interface.

[5] https://www.lammps.org/

[6] https://www.ovito.org/

Chapter 4

Force field development for ALD of Hafnium Dioxide

Ab initio method is a very powerful tool to study the quantum properties of molecular systems. Together with molecular mechanics, the spatial and temporal evolution of a system of molecules can be accurately modelled from its computed electronic structure. However, running such first-principle MD simulations is computationally demanding. As a consequence, the accessible timescale of this method is rather short - less than a nanosecond, and the size of the system under study must be small. Thus, its use case is very limited.

To efficiently describe the dynamics of a molecular system on large spatial scales and long time scales, empirical force fields have been proven to be extremely useful. A force field is referred to as a collection of parameters which constitute inter-atomic potential functions. These potential functions, in turn, determine the physical interaction between particles in a molecular system. Since the interacting forces between neighbouring atoms are calculated from mathematical models, accuracy is traded for fast computation time, making it more practical to run MD simulations on larger systems and for longer time intervals.

4.1 Empirical force fields

The first group of inter-atomic potentials is known as parametric potentials. A parametric potential function describes the potential energy surface of a system through its analytical form, in which parameters have some physical interpretations. The most prominent example of this family is the Lennard-Jones pair potential [31], which can model quite accurately van der Waals interactions between particles in a fluid or between molecules of

noble gases:

$$V_{LJ}(r) = 4\epsilon \left[\left(\frac{\sigma}{r} \right)^{12} - \left(\frac{\sigma}{r} \right)^{6} \right] \tag{4.1}$$

A more general form of the Lennard-Jones potential, known as Morse potential, is also widely used due to its fast calculation and acceptable accuracy when modelling bonded atoms of a diatomic molecule:

$$V_M(r) = D_e \left[e^{-2a(r-r_e)} - 2e^{-a(r-r_e)} \right] \tag{4.2}$$

Nevertheless, being of the two-body type, both Lennard-Jones and Morse potentials fail to describe solid-state matters, for instance, metal and semiconductor crystals. Many-body potentials must be included for those applications, such as the Stillinger-Weber potential [32] originally designed for pure silicon crystal, or the Embedded Atom Model (EAM) [33, 34] for metal solids.

Another type of parametric potential is bond order potential. The common idea behind bond order potentials is that the interaction between two particles does not depend only on their inter-atomic distance, but also on the "environment" around them. The atomic environment comprises the number of bonds, types of bonding, angles, dihedrals, etc. Hence, bond order potentials can be generally expressed in the form:

$$V_{ij}(r_{ij}) = V_{repulsive}(r_{ij}) + b_{ijk} V_{attractive}(r_{ij}) \,, \tag{4.3}$$

where b_{ijk} encompasses all information about the atomic environment.

Figure 4.1 shows the effect of changing the value of b_{ijk} on the potential energy curve of a diatomic pair. The force acting on two particles ranges from being repulsive at small distances and attractive at large distances to purely repulsive as b_{ijk} approaches zero. This enables bond order potentials to model proper interactions in complex molecular systems, especially where chemical reactions are involved. To date, several bond order potentials have been developed for various materials, for example, Tersoff potential [35], Brenner potential [36], and ReaxFF [37].

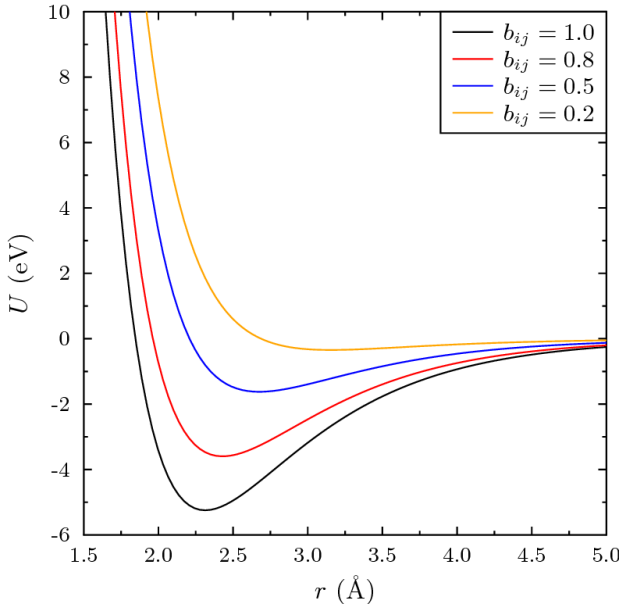

Figure 4.1 *Dependency of bond potential energy on the value of the atomic environment parameter b_{ijk} [38].*

The second group of inter-atomic potentials is non-parametric potentials. The main difference between non-parametric and parametric potentials lies in their mathematical forms. Non-parametric potentials do not have a fixed number of physically comprehensible parameters and are often expressed by the formula:

$$V = \sum_{i}^{N} E(\mathbf{q}_i)\,, \tag{4.4}$$

where $\mathbf{q}_i$, known as the "descriptor", and $E(\cdot)$, known as the regression model, are the two main components. The "descriptor" $\mathbf{q}_i$ stores the environment information surrounding atom i, and $E(\cdot)$ provides the potential computed from the "descriptor" with a complex prediction model. Due to its complex nature, the prediction model is very well-described by a suitable machine-learning model, leading to a potential set that can be systematically improvable through several machine-learning methods, such as neural networks [39], Gaussian process regression [40], or simple linear regression [41]. Thus, non-parametric potentials are often referred to as Machine-Learned Interatomic Potentials (MLIPs).

MLIPs are thought to have a level of accuracy on par with quantum mechanics but only come at a fraction of the computational cost [42]. This is due to their non-definitive form that allows this type of potential function to flexibly provide a more precise description of inter-atomic interactions. However, it is also a major problem with MLIPs. These

potentials often require a substantial amount of molecular configurations as training data, but usually fail to predict the dynamics of systems slightly different from the training data-set, i.e., they have poor extrapolability. MLIPs also lacks visualisation tools and meaningful metrics to evaluate the force field. Although there have been techniques proposed to improve the robustness and transferability of MLIPs, such as active learning [43], care must be taken when employing non-parametric potentials in a molecular mechanics study.

In this application of modelling the ALD process, bond order potentials emerge as a suitable solution thanks to their ability to describe chemical reactions. Classical non-reactive potentials do not have this feature because every bond must be explicitly defined before simulations; breaking and formation of bonds are not allowed.

Among available bond order potentials, ReaxFF is superior due to its sophisticated formalism and versatility towards diverse kinds of molecular systems. ReaxFF, abbreviated for "reactive force field", was originally developed for hydrocarbons [37]. ReaxFF is a collection of parameters that can describe two-body bonded and non-bonded interactions, as well as three-body and four-body interactions between atoms. Therefore, the total energy of a system can be written in the following form:

$$\begin{aligned} E_{system} = E_{bond} + E_{angle} + E_{torsion} + E_{vdW} + E_{Coulomb} \\ + E_{correction} + E_{specific} \end{aligned} \tag{4.5}$$

Similar to other bond order potentials, the bond order between a pair of atoms is the essence of ReaxFF and is explicitly computed by the formula:

$$\begin{aligned} BO_{ij} &= BO_{ij}^{\sigma} + BO_{ij}^{\pi} + BO_{ij}^{\pi\pi} \\ &= exp\left[p_{bo1}\left(\frac{r_{ij}}{r_0^{\sigma}}\right)^{p_{bo2}}\right] + exp\left[p_{bo3}\left(\frac{r_{ij}}{r_0^{\pi}}\right)^{p_{bo4}}\right] + exp\left[p_{bo5}\left(\frac{r_{ij}}{r_0^{\pi\pi}}\right)^{p_{bo6}}\right], \end{aligned} \tag{4.6}$$

where r_{ij} is the inter-atomic distance, while p_{bo1}, p_{bo2}, p_{bo3}, p_{bo4}, p_{bo5}, p_{bo6}, r_0^{σ}, r_0^{π}, $r_0^{\pi\pi}$ are parameters of the force field. From the bond order information, every component of the total potential energy is computed according to a set of equations defined in ReaxFF. The detailed functional forms of all equations are explained in Appendix A.

Due to the high complexity of the force field, the parameterisation procedure for ReaxFF is iterative and involves a great number of training data so that the obtained parameters can correctly describe the behaviour of the system. Training data can be geometrical properties like equilibrium bond length and bond angle, bond dissociation energy, Potential Energy Surface (PES) scan, surface energy, activation energy and reaction enthalpy, the heat of formation, partial charges, atomic forces, etc. Those data may be acquired from experimental measurements, or more and more frequently, results

from quantum chemistry computational methods which are considered to provide an exact description of the molecular system, such as *ab initio* calculations.

4.2 ReaxFF parameterisation

4.2.1 Training data

To correctly model the interaction among five elements Si/O/H/Hf/Cl in the ALD of HfO_2 on hydroxylated Si surface from $HfCl_4$ and H_2O, bond distance energies and bond angle energies of a variety of molecules were used as a source of reference data against which force field's parameters were optimised. Because there has been a ReaxFF force field developed for silicon surface and water, parameters for Si/O/H interactions were adopted from [44] with some minor tweaks. Parameters for bonds between Hf and Cl, as well as their interactions with other elements had to be fitted extensively to the reference data.

All reference data were obtained with the Density Functional Theory (DFT) method in this work. DFT calculations were performed in ORCA 5.0 program, utilising the *Perdew-Burke-Ernzerhof* Generalised Gradient Approximation (GGA-PBE) [17] exchange-correlation functionals and the *def2-TZVP* basis set [45] for all five elements. Since hafnium is a transition metal with a relatively large shell, Effective Core Potentials (ECP) method [46] was employed for DFT calculations on hafnium atoms to reduce the computational cost and basis set superposition errors [47].

Another type of training data for this application is the minimum energy transition path of possible surface reactions. There have been several first principle studies of the reaction pathway of hafnium tetra-chloride and water on various types of surfaces, for example, H-terminated Si [48], OH-terminated SiO_2 [49, 50, 51, 52, 53], Si/Ge hetero-surface [54], or stably-grown HfO_2 film [55]. However, these studies modelled the first half-reaction in the ALD process with the formation and removal of only one HCl molecule per reaction site. Willis et al. [56] conducted more sophisticated computations of the surface configuration when more than one HCl molecule is released from a $HfCl_4$ molecule chemisorbed on the hydroxylated Si(100) surface. Although the adsorption energy was reported in various scenarios, this study did not provide the reaction profile and activation energy of surface reactions that happened in the ALD process of HfO_2. Therefore, in this thesis, detailed reaction pathways of both half-reactions with up to two HCl molecules produced at a reaction site were constructed. Computations were performed on three cluster models representing the OH/Si(100)-2 $\times$ 1 reconstructed surface (see Figure 4.2):

- $Si_9H_{12}(OH)_2$: a single Si dimer with two surface OH groups.

- $Si_{15}H_{16}(OH)_4$: two adjacent Si dimers of the same dimer row with four surface OH groups.
- $Si_{23}H_{24}(OH)_4$: two adjacent Si dimers of two adjacent dimer rows with four surface OH groups.

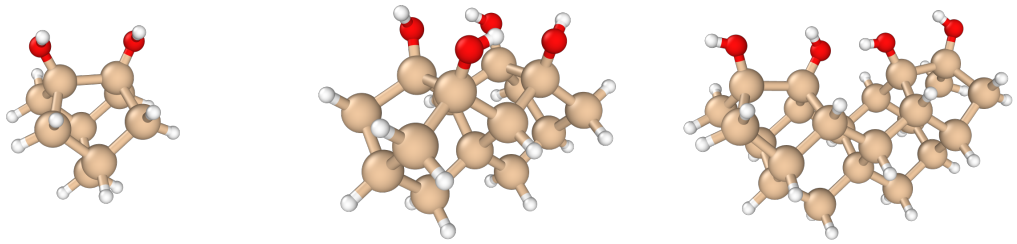

(a) $Si_9H_{12}(OH)_2$ (b) $Si_{15}H_{16}(OH)_4$ (c) $Si_{23}H_{24}(OH)_4$

Figure 4.2 *Cluster models used to construct surface reaction profiles. (Colour:* H *- white,* O *- red,* Si *- beige).*

Climbing-image Nudged Elastic Band (CI-NEB) method [57] was employed to search for the transition state and determine the activation energy of surface reactions in the ALD process. During the geometry optimisation and transition state search, every sub-surface atom was fixed in space; only surface Si atoms, hydroxyl groups, and adsorbed molecules were allowed to move. The reaction profiles of the first half-reaction on the three cluster models, from the adsorption of the $HfCl_4$ molecule to the desorption of two HCl molecules, are depicted in Figure 4.3, 4.4, and 4.5.

It can be seen that the dissociation of the $HfCl_4$ molecule is more favourable in the $Si_{23}H_{24}(OH)_4$ cluster, i.e., the position between two Si dimers, where the energy barriers to remove one and two HCl molecules are $0.44eV$ and $0.55eV$, respectively. When $HfCl_4$ is chemisorbed on top of a dimer row, more energy is required to break Cl-Hf bonds and form HCl molecules. In all cases, up to the point where two HCl molecules are released, the reaction is endothermic. In a real surface process, there could be a removal of three or four HCl molecules from one $HfCl_4$ adsorbate, and the direction of the reaction is expected to be more endothermic [58].

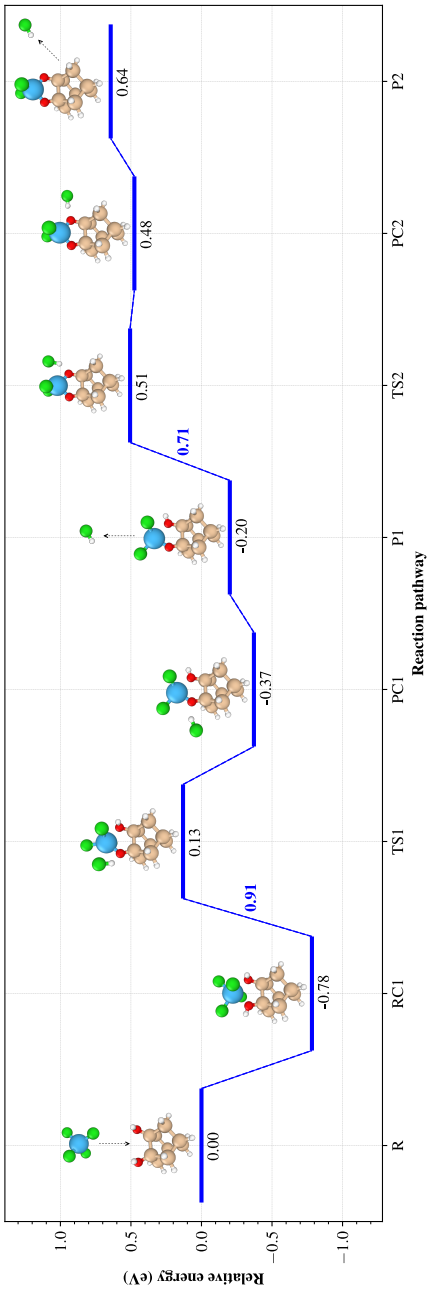

Figure 4.3 *The reaction pathway of the first half-reaction when a* $HfCl_4$ *molecule is adsorbed on the* $Si_9H_{12}(OH)_2$ *cluster. (Colour:* H - *white,* O - *red,* Si - *beige,* Cl - *green,* Hf - *azure).*

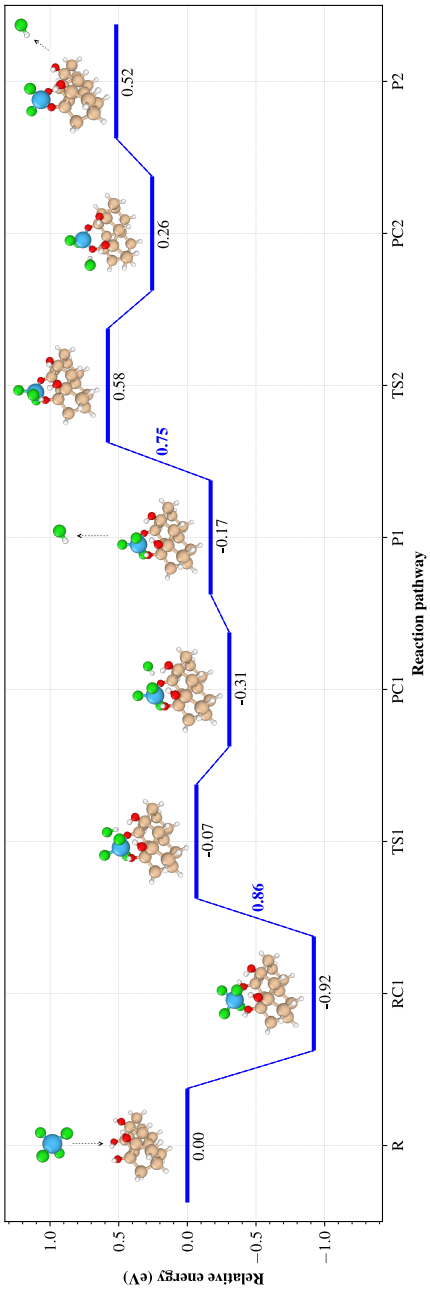

Figure 4.4 *The reaction pathway of the first half-reaction when a* $HfCl_4$ *molecule is adsorbed on the* $Si_{15}H_{16}(OH)_4$ *cluster. (Colour:* H - *white,* O - *red,* Si - *beige,* Cl - *green,* Hf - *azure).*

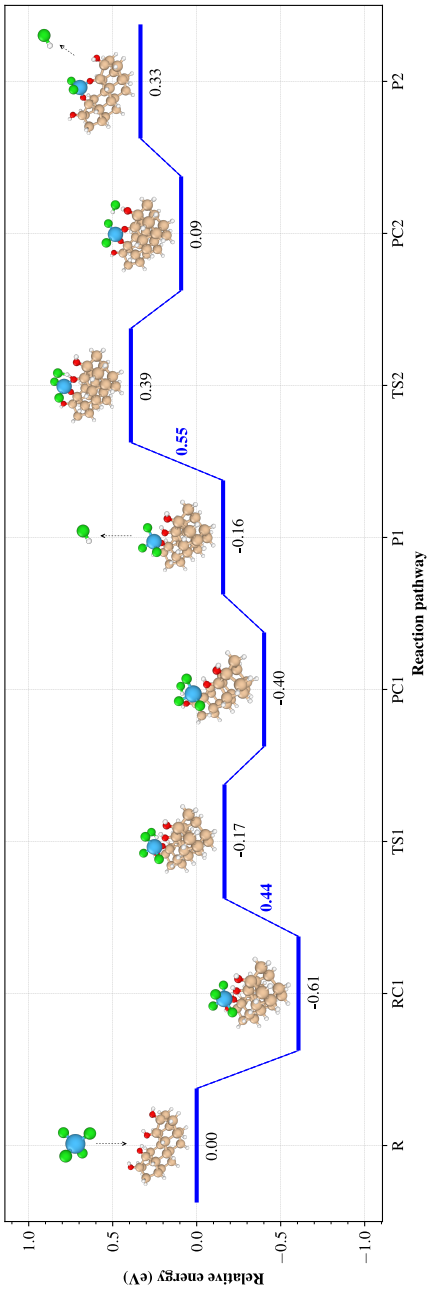

Figure 4.5 *The reaction pathway of the first half-reaction when a* $HfCl_4$ *molecule is adsorbed on the* $Si_{23}H_{24}(OH)_4$ *cluster. (Colour:* H - *white,* O - *red,* Si - *beige,* Cl - *green,* Hf - *azure).*

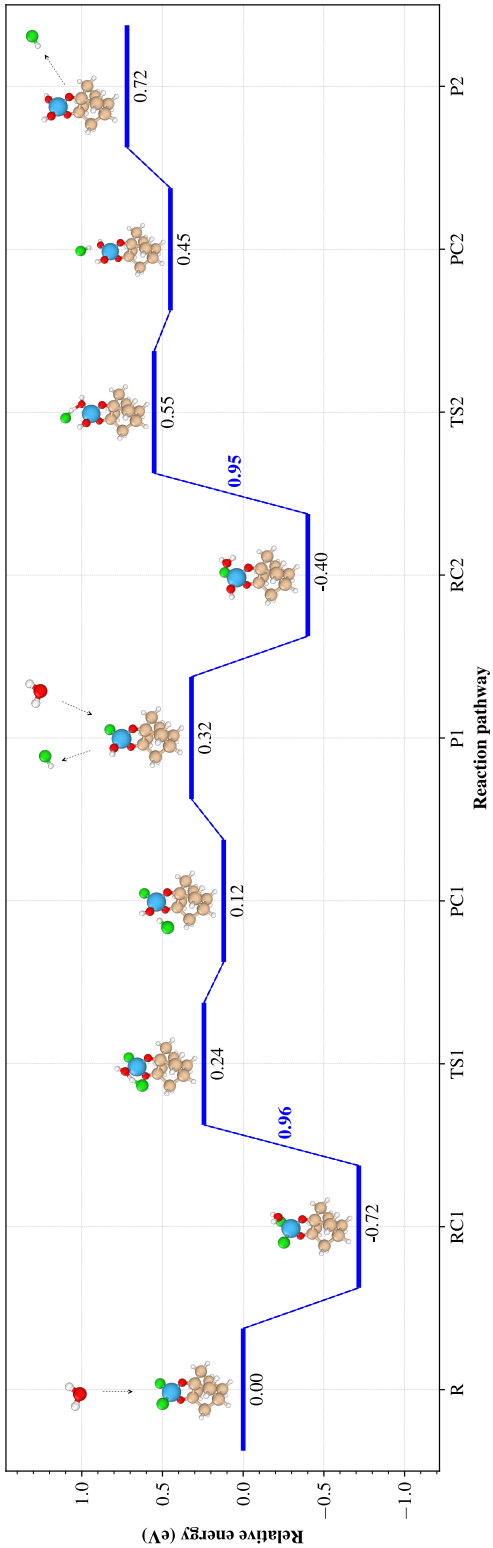

Figure 4.6 *The reaction pathway of the second half-reaction when* H_2O *molecules are adsorbed on the* $Si_9H_{12} - 2O - HfCl_2$ *cluster. (Colour:* H - *white,* O - *red,* Si - *beige,* Cl - *green,* Hf - *azure).*

In the second half-reaction, water molecules bind to the $(-2O - HfCl_2)$ species on the surface, and the surface species' adsorption site no longer plays an important role in its ligand-exchange kinetics with water. Hence, the reaction pathway is studied only for the $Si_9H_{12} - 2O - HfCl_2$ cluster (see Figure 4.6). The second half-reaction is also endothermic with even higher activation energies.

After the second half-reaction, hydroxyl groups attached to the hafnium atom will act as reaction sites for subsequent ALD cycles. For the sake of simplicity, surface reactions on stably-grown thin film and densification of HfO_2 [55, 52] are not constructed in the force field's training set. Given the good transferability of the ReaxFF force field when describing closely resembling processes, those reactions should be adequately emulated in an empirical MD simulation.

4.2.2 MD simulations and the timescale issue

MD is a deterministic method used to model the spatial and temporal evolution of a system of particles under Newton's laws of motion. The position and velocity of all particles are updated from calculated interatomic forces after every timestep of a simulation. Thanks to modern computer architectures and the parallelisation of computation units, MD simulations are feasible to model systems of up to millions of atoms [59, 60]. However, such parallelisation could not be applied to time integration, since it is inherently a sequential process, i.e., the state of the system can only be determined if its preceding state is already known. Since timesteps in an MD simulation must be short to ensure numerical stability and integrity, typically on the order of femtoseconds, it could take millions or billions of timesteps to run a microsecond-long simulation. For a complex force field like ReaxFF, the maximum recommended timestep is a quarter of a femtosecond [61, 62, 63], which makes the number of calculations more exaggerated. Hence, the accessible timescale of MD simulations is still limited to the microseconds range.

If a chemical process is assumed to follow the Transition State Theory (TST), then its transition rate can be approximated by the Arrhenius equation:

$$k = A \exp\left(-\frac{E_a}{RT}\right),$$

where k is the rate constant, A is the pre-exponential coefficient, R is the universal gas constant, T is the absolute temperature in Kelvin, and E_a is the activation energy of the reaction. Figure 4.7 plots the dependency of average transition time $1/k$ on the activation energy at $500K$ and $A = 10^{14}s^{-1}$.

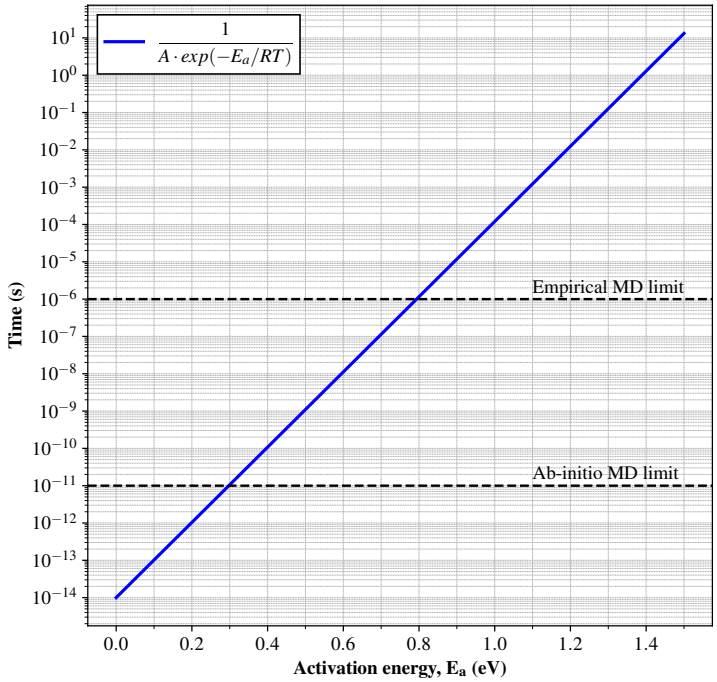

Figure 4.7 *Average transition time as a function of activation energy by the Arrhenius equation at* $A = 10^{14}s^{-1}$ *and* $T = 500K$.

For a thermally activated process ($E_a \gg RT$), the average time between events is beyond the timescale limit of empirical MD simulations, even at a high pre-exponential factor of $10^{14}s^{-1}$. Surface reactions involved in the ALD process of HfO_2, where the maximum energy barrier is slightly short of $1eV$, can be classified as such rare events. Thus it is impractical to extract useful information solely from ordinary MD simulations for a vapour deposition process.

Many techniques have been developed to extend the accessible timescale of MD simulations. Hyper-dynamics [64], Temperature-accelerated Dynamics [65], and Parallel Replica Dynamics [66] are three well-known algorithms proposed by Voter and Sorensen to accelerate the temporal evolution of MD simulations. Mees et al. [67] took on another approach which associated an average time-step to force-bias Monte Carlo methods to emulate MD simulations over a longer time span. All of these algorithms are versatile and do not require *a priori* knowledge about the transition pathway. However, their boost factor, ranging from zero to a few orders of magnitude, is heavily dependent on the characteristic of the system.

In a highly complex process such as ALD, which involves numerous surface reactions over long periods and many simulation runs, accelerated MD techniques may not be efficient to model the growth kinetics of the film. Therefore, in this work, the timescale problem was addressed by incorporating acceleration into the parameterisation procedure of the force field. This is done by deliberately decreasing the dissociation energy of H-O bonds and Cl-Hf bonds (computationally reported to be $3.77eV$ [68]) while keeping the dissociation energy of Cl-H bonds and Hf-O bonds (computationally reported to be $4.07eV$ [68]) parallel to their quantum chemistry data. In any case, the potential well is carefully fitted around the equilibrium bond distance in the ReaxFF curve. The strategy is equivalent to preserving the transition state's activation energy while lowering the reaction's potential energy landscape. Although the thermodynamic properties of the system are violated, the kinematics of the surface reaction is maintained, but with crossing of the energy barrier events become more frequent.

4.2.3 Training procedure

After ground-truth data of PES of bond distances and angles, as well as reaction activation energy, had been acquired from DFT, the training of ReaxFF parameters could be performed with a proper tool. For the purpose of this thesis, *ReParTO* (ReaxFF Parameterisation TOol)[1] - a simple software implemented with Python to fit ReaxFF parameters was exclusively developed. The fitting procedure could be described as follows:

1. Each configuration in the training set is run through a single-point calculation using the built-in ReaxFF calculator of LAMMPS. The ReaxFF calculator, at this step, is set up with the initial parameter set. At the end of this set, a collection of predicted potential energy values is produced.
2. The predicted values are compared with their corresponding reference values from DFT. A sum-of-squared-errors value is computed by aggregating all squared differences between the ground truth and prediction.
3. ReaxFF parameters are continuously varied by a single-objective optimisation algorithm to minimise the sum of squared errors. The tool used in this work employs the Covariance Matrix Adaptation Evolution Strategy (CMA-ES) optimisation algorithm [69].
4. The procedure stops when the sum of squared errors does not improve after a predefined number of iterations of step *3*. The parameter value that yields the smallest error is the optimised ReaxFF parameter set.

[1] https://gitlab.com/dt.tran/reparto.git

In practice, the ReaxFF parameter set is large, containing hundreds of parameters; therefore, it is impossible to refine all parameters at once. Parameters are often optimised in small batches, for example, a group of closely related parameters that affect a certain type of bond. The training workflow is performed one to a few times for each batch until the entire parameter set is tuned.

The reference DFT and fitted ReaxFF potential energy curve of bond lengths and angles are shown in Figure 4.8 and 4.9. The reference DFT and fitted ReaxFF activation energy of ALD surface reactions are listed in Table 4.1. The ReaxFF file with all optimised parameters can be accessed from Appendix B.

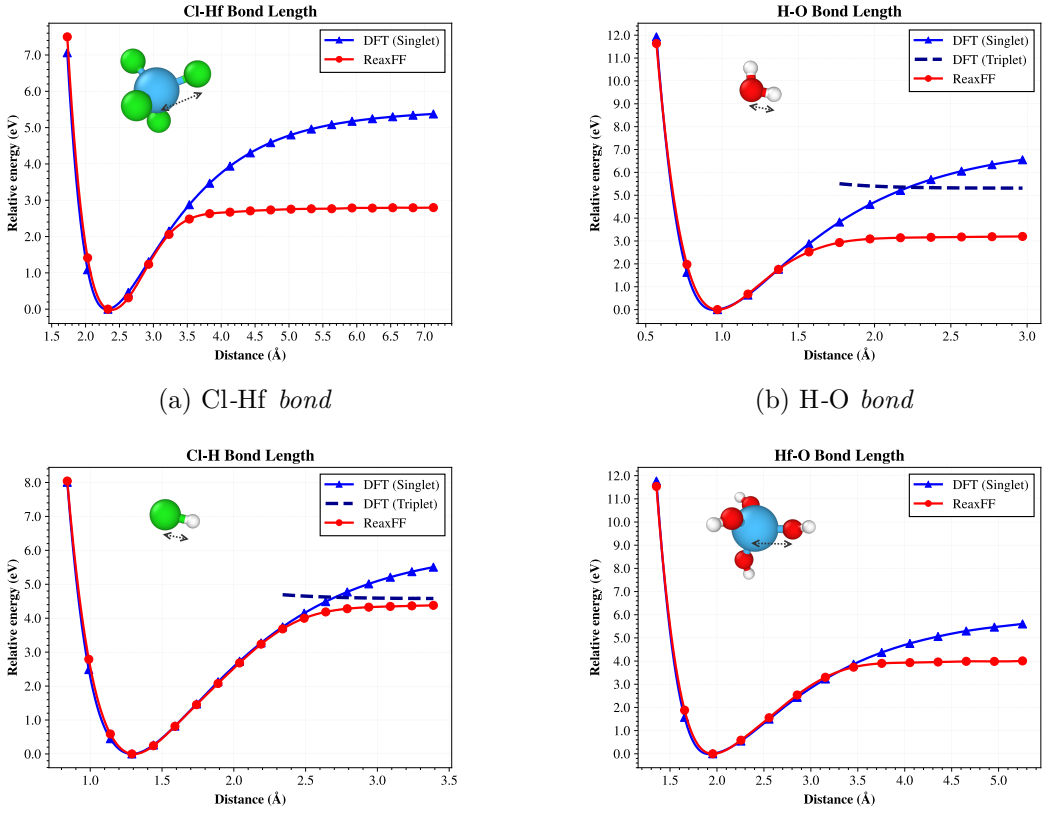

(a) Cl-Hf *bond*

(b) H-O *bond*

(c) Cl-H *bond*

(d) Hf-O *bond*

Figure 4.8 *PES curve of bond lengths, fitted ReaxFF versus reference DFT. (Inset image colour:* H - *white,* O - *red,* Cl - *green,* Hf - *azure).*

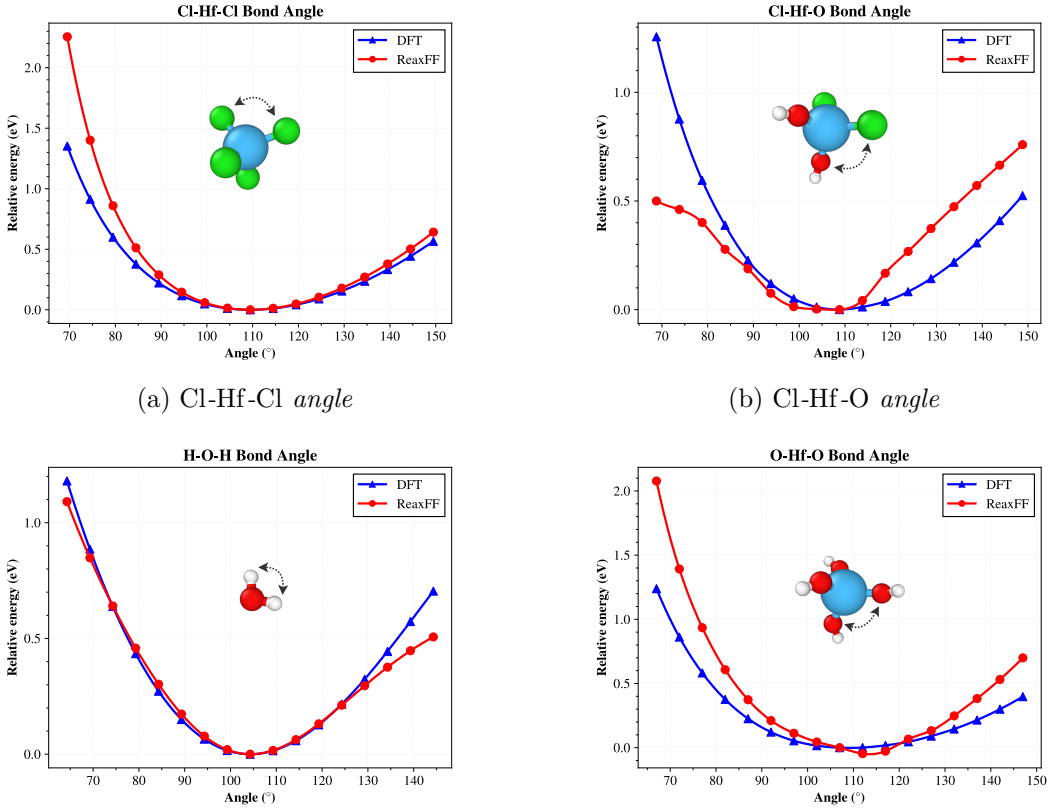

(a) Cl-Hf-Cl *angle*

(b) Cl-Hf-O *angle*

(c) H-O-H *angle*

(d) O-Hf-O *angle*

Figure 4.9 *PES curve of bond angles, fitted ReaxFF versus reference DFT. (Inset image colour:* H *- white,* O *- red,* Cl *- green,* Hf *- azure).*

Table 4.1 *Activation energy E_a of surface reactions, ReaxFF versus DFT.*

Reaction	**E_a (eV)**	
	DFT	**ReaxFF**
$Si_9H_{12}(OH)_2 + HfCl_4 \rightarrow Si_9H_{12}(OH) - O - HfCl_3 + HCl$	0.91	1.11
$Si_9H_{12}(OH) - O - HfCl_3 \rightarrow Si_9H_{12} - 2O - HfCl_2 + HCl$	0.71	0.46
$Si_{15}H_{16}(OH)_4 + HfCl_4 \rightarrow Si_{15}H_{16}(OH)_3 - O - HfCl_3 + HCl$	0.86	1.03
$Si_{15}H_{16}(OH)_3 - O - HfCl_3 \rightarrow Si_{15}H_{16}(OH)_2 - 2O - HfCl_2 + HCl$	0.75	1.35
$Si_{23}H_{24}(OH)_4 + HfCl_4 \rightarrow Si_{23}H_{24}(OH)_3 - O - HfCl_3 + HCl$	0.44	0.62
$Si_{23}H_{24}(OH)_3 - O - HfCl_3 \rightarrow Si_{23}H_{24}(OH)_2 - 2O - HfCl_2 + HCl$	0.55	0.60
$Si_9H_{12} - 2O - HfCl_2 + H_2O \rightarrow Si_9H_{12} - 2O - HfCl(OH) + HCl$	0.96	1.26
$Si_9H_{12} - 2O - HfCl(OH) + H_2O \rightarrow Si_9H_{12} - 2O - Hf(OH)_2 + HCl$	0.95	0.77

Chapter 5

MD simulation of ALD of Hafnium Dioxide

HfO_2 is a dielectric material that is substituting SiO_2 as gate oxide in Metal-Oxide-Semiconductor (MOS) transistors thanks to its superior electrical properties that meet the criteria of device scaling. HfO_2 is usually deposited in an ALD process, which can be thought of as a sequential CVD where vapour-phase reactants are separated into alternating pulses to have perfect control of the thickness of the grown film.

There have been lots of experimental investigations into the deposition of HfO_2 from two common precursors: $HfCl_4$ and H_2O [70, 71, 72, 73, 74, 75, 76]. However, atomic-scale research into the growth kinetics received so much less interest, probably due to difficulties in computationally describing ALD-related surface processes, e.g., chemisorption, desorption, chemical reaction, diffusion, and densification. Most of the computational studies into ALD of HfO_2 to date only report simplistic reaction mechanisms using first-principle methods [49, 51, 53]. Dkhissi et al. [52] took a step further by modelling HfO_2 thin film growth with an on-lattice kinetic Monte Carlo approach. Although the model was able to predict the growth kinetics in the first cycle, it failed to correctly simulate the growth in subsequent cycles due to the stochastic nature of the algorithm. Deterministic MD simulations of the ALD process have been successfully attempted by Zheng et al. [77] and Romine et al. [78], but the model was developed for Al_2O_3 film. Therefore, in this thesis, I want to gain more insights into the atomistic behaviour of the ALD process of HfO_2 thin film via the molecular mechanics method, utilising the ReaxFF force field prepared in Chapter 4.

5.1 Simulation setup

In this work, a thin HfO_2 film was deposited on an OH-terminated Si(100) slab from pulses of $HfCl_4$ and H_2O. The silicon slab was constructed from six atomic layers, each layer was an 8×8 grid of Si atoms. This results in a square 384-atom Si(100) slab with lateral dimensions of 30.7Å. Any MD simulation involving this silicon slab from this point on would force its bottom 2-layer to stay fixed in position to represent the underlying silicon bulk; other atoms were free to move. Periodic Boundary Conditions (PBC) were applied to the x and y directions of the simulation box. The time-step was set to $0.25fs$.

First, the Si slab was thermalised at $500K$ in a Berendsen NVT ensemble for $25ps$. Snapshots of the slab at the end of the MD run are shown in Figure 5.1. We can see that the ReaxFF force field can correctly model the reconstruction of dimers on the Si(100) surface [79, 80]. Two adjacent Si atoms on the surface have the tendency to form a dimer bridge to minimise the number of dangling bonds, thus resorting to a more stable surface configuration.

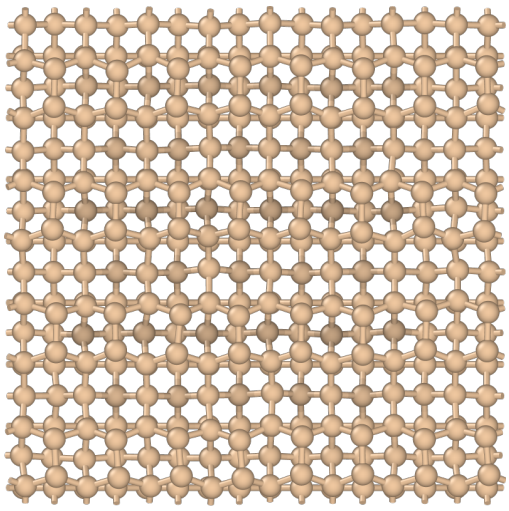

(a) *Top view*

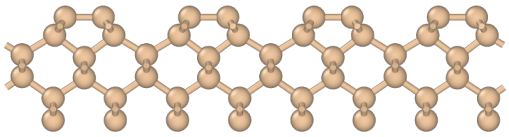

(b) *Side view*

Figure 5.1 Si *slab after thermalisation at* $500K$. *(Colour:* Si - *beige).*

Next, hydroxyl groups were randomly added to the surface so that oxygen atoms were attached directly above silicon atoms. Three slab models with different levels of OH concentration were prepared (see Figure 5.2):

- 10% OH coverage (7 hydroxyl groups or 0.74 OH/nm^2): this level is comparable with the OH concentration on a Si surface treated with HF to remove native oxide [72].
- 50% OH coverage (32 hydroxyl groups or 3.40 OH/nm^2): half of the dangling bonds on the surface are passivated with OH groups. This level is similar to the OH concentration on a thermally-grown wet oxide [72].
- 100% OH coverage (64 hydroxyl groups or 6.79 OH/nm^2): the surface is fully saturated with OH groups, representing a chemical oxide Si-O-H surface often achieved by piranha solution or Standard Clean 1 (SC-1) procedure [72].

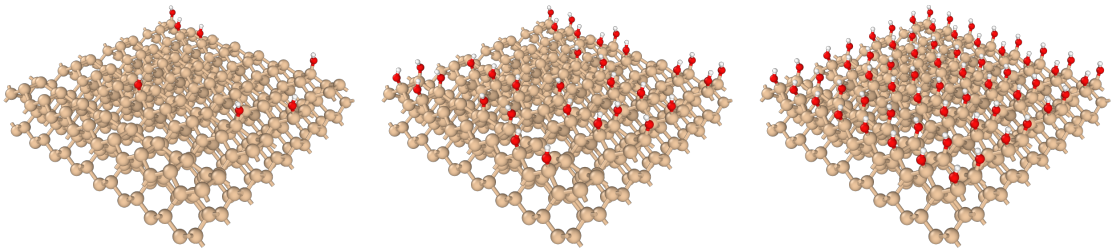

(a) 10% OH *coverage* (b) 50% OH *coverage* (c) 100% OH *coverage*

Figure 5.2 Si *slab at various* OH *surface concentration levels. (Colour:* H - *white,* O - *red,* Si - *beige).*

The simulation of a single cycle of ALD of HfO_2 was carried out in two runs representing the two precursor phases:

- $HfCl_4$ phase: A $HfCl_4$ molecule was injected into the simulation box at a random position 20Å - 40Å above the surface every $1ps$, up to a total of 150 molecules.
- H_2O phase: A H_2O molecule was injected into the simulation box at a random position 20Å - 40Å above the surface every $0.25ps$, up to a total of 200 molecules.

All inserted molecules were directed toward the surface at the velocity computed from their thermal energy at $500K$ - the simulated deposition temperature. In each phase, before the deposition occurs, the entire slab was thermalised for $10ps$ at $500K$; temperature was controlled by a Berendsen thermostat. During the deposition, only two Si layers immediately above the fixed bottom layers were coupled to a heat bath i.e. the NVT

ensemble, while other atoms were kept in the NVE ensemble. This setup allows for high-temperature local spots when molecules collide with and adsorb to the surface, making surface reactions more likely to happen. Non-reacted precursor and product molecules were removed when they reach the ceiling of the simulation box. Then, the system was kept running continuously with the same settings for 15ps without any newly inserted molecules. After the deposition period, the substrate and deposited film were annealed at 1,000K for 20ps to get rid of residuals on the surface and stabilise the film, while every gas molecule was drawn out to mimic the purge process. Then, everything was equilibrated again at 500K for 5ps. The total simulation time was 200ps and 100ps for each $HfCl_4$ and H_2O pulse, respectively.

5.2 Simulation results

5.2.1 Surface reactions

The ReaxFF force field employed in this work is a bond order potential and the bond information among atoms is computed on-the-fly during the simulation [37]. Indeed, the kinetics of some surface reactions demonstrated by cluster models in Chapter 4 were adequately reproduced in the first cycle of the MD simulation of ALD of HfO_2.

Figure 5.3 illustrates the simplest surface reaction in which only one ligand-exchange reaction occured between the $HfCl_4$ molecule and the OH group on the surface, releasing one HCl molecule. Additionally, since there was another OH group within a short distance, the chemisorbed species continued to react with the second OH group, producing one more HCl molecule. In this case, the two OH groups were on the same side of two adjacent Si dimers of the same dimer row. The close-up snapshots of the second reaction are shown in Figure 5.4.

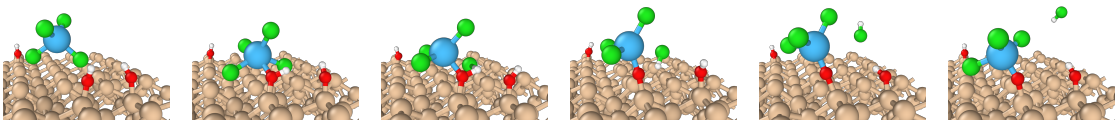

Figure 5.3 *MD snapshots of the first half-reaction with the first* HCl *molecule released. (Colour:* H - *white,* O - *red,* Si - *beige,* Cl - *green,* Hf - *azure).*

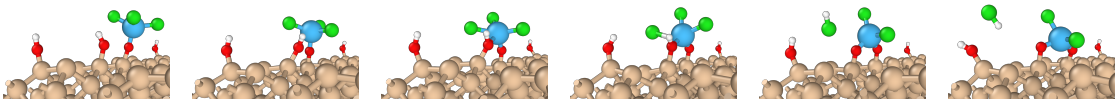

Figure 5.4 *MD snapshots of the first half-reaction with the second* HCl *molecule released. (Colour:* H - *white,* O - *red,* Si - *beige,* Cl - *green,* Hf - *azure).*

The ReaxFF force field also did really well in describing situations similar to but are not included in the training data. When the density of surface OH groups increased, there could be cases when more than two OH groups were closely located to each other. The energy barrier of further oxidation of the surface species could be overcome, leading to having its third Cl atom removed as shown in Figure 5.5, or even the loss of all four Cl atoms in Figure 5.6.

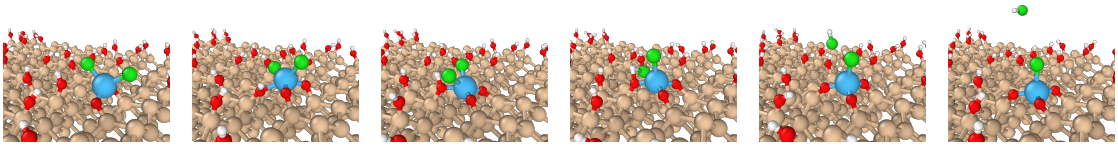

Figure 5.5 *MD snapshots of the first half-reaction with the third* HCl *molecule released. (Colour:* H - *white,* O - *red,* Si - *beige,* Cl - *green,* Hf - *azure).*

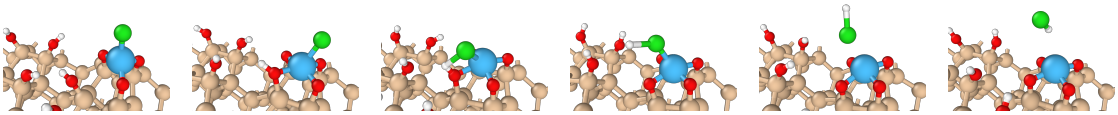

Figure 5.6 *MD snapshots of the first half-reaction with the fourth* HCl *molecule released. (Colour:* H - *white,* O - *red,* Si - *beige,* Cl - *green,* Hf - *azure).*

The reaction mechanisms between the adsorbed surface species with H_2O were also correctly recreated during the water pulse. Figure 5.7 and Figure 5.8 depict the adsorption of H_2O molecules, the transition state, and the desorption of HCl products until all Cl atoms of the $(-2O - HfCl_2)$ surface species were replaced with two new OH groups. These new OH groups would serve as reaction sites for the growth of subsequent mono-layers. In this idealistic case, a perfect stoichiometric HfO_2 film would be achieved.

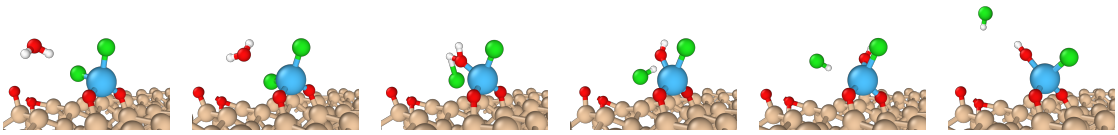

Figure 5.7 *MD snapshots of the second half-reaction with the first* HCl *molecule released. (Colour:* H - *white,* O - *red,* Si - *beige,* Cl - *green,* Hf - *azure).*

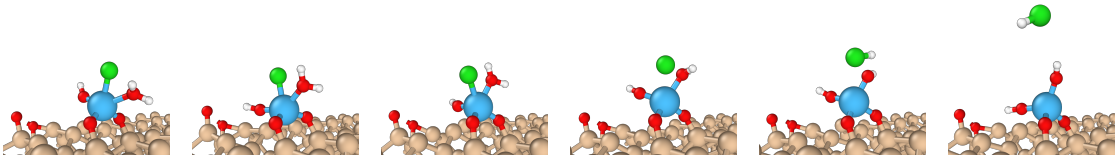

Figure 5.8 *MD snapshots of the second half-reaction with the second* HCl *molecule released. (Colour:* H - *white,* O - *red,* Si - *beige,* Cl - *green,* Hf - *azure).*

In addition, MD simulations with the ReaxFF force field predicted a more sophisticated reaction where one H_2O molecule hydrolysed both Cl atoms of the $(-2O - HfCl_2)$ surface species, leaving a single surface O atom bonded to the Hf centre by a double bond [58] (see Figure 5.9). This situation might result in a HfO_x film with poor stoichiometry and lower O-content. The oxygen concentration is a crucial factor in determining the structural and electrical properties of the hafnium oxide film: low oxygen concentration lessens the band gap, making the film exhibit metallic behaviours [81, 82], while excessive O-content introduces more interface traps [83] and degrades electron mobility in the channel [84].

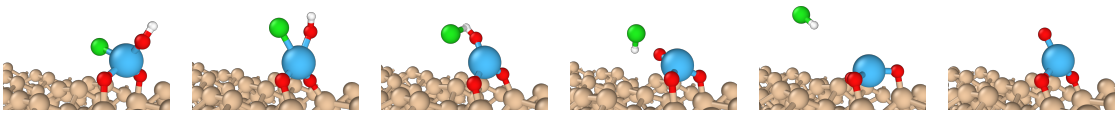

Figure 5.9 *MD snapshots of the second half-reaction with the second* HCl *molecule released from one* H_2O *molecule. (Colour:* H - *white,* O - *red,* Si - *beige,* Cl - *green,* Hf - *azure).*

5.2.2 Growth rate and dependency on initial OH coverage

Although various surface reactions in the ALD process of HfO_2 on Si from $HfCl_4/H_2O$ have been reported above, the definitive structure of the deposited film is still of interest. Thus, in this part, the overall growth mechanism and growth rate will be evaluated corresponding to three initial surfaces with different OH densities.

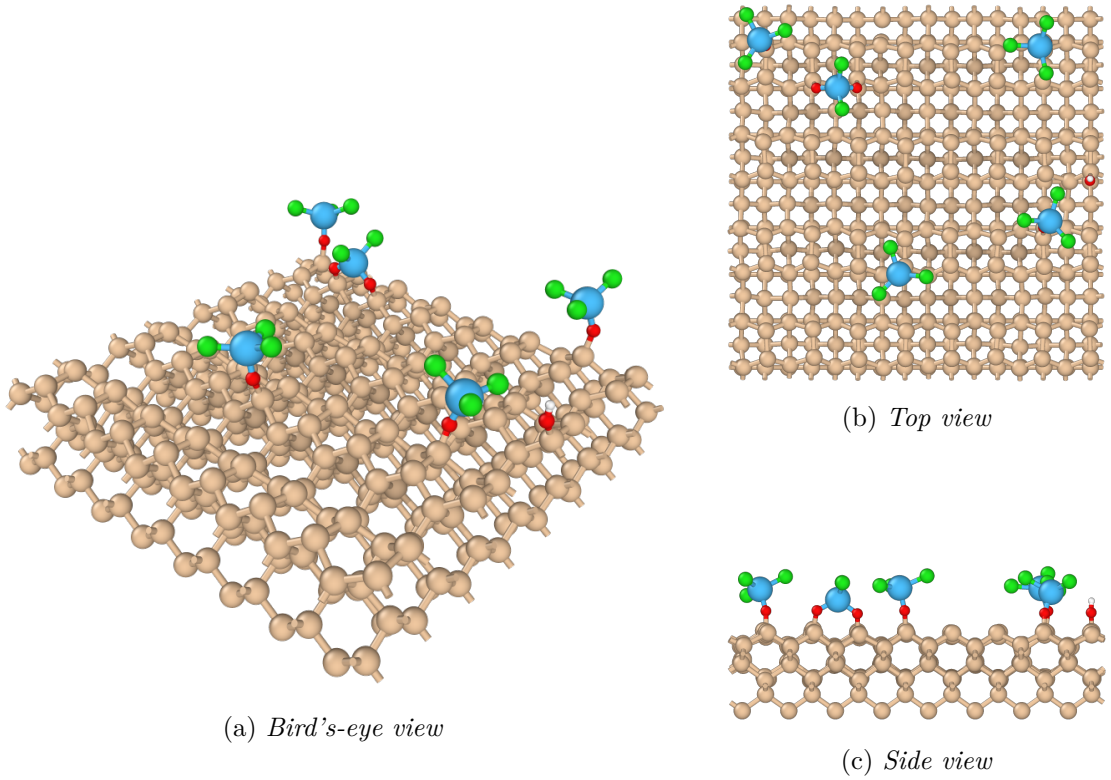

(a) *Bird's-eye view*

(b) *Top view*

(c) *Side view*

Figure 5.10 *The* 10% OH *coverage surface after the* $HfCl_4$ *pulse, first cycle. (Colour:* H - *white,* O - *red,* Si - *beige,* Cl - *green,* Hf - *azure).*

Figure 5.10 shows the Si surface at 10% OH coverage after the $HfCl_4$ pulse of the first cycle. Since OH groups were sparsely distributed, chemisorbed species were isolated from each other. Chemisorbed species also had at maximum two chlorine atoms removed during reactions due to the scarcity of hydrogen moieties on the initial surface. The surface area uncovered by OH groups remained nonreactive, showing no trace of physisorbed $HfCl_4$ molecules.

When the OH concentration increased, more $HfCl_4$ molecules adsorbed and reacted with reactive groups on the surface (see Figure 5.11). A greater number of reaction sites also caused more uniform distribution of the film, as seen from the 50% OH coverage surface to the 100% OH coverage surface. Additionally, with an abundant supply of

hydrogen in both cases, hafnium-containing surface species started to lose more than two chlorine atoms in a single adsorption event.

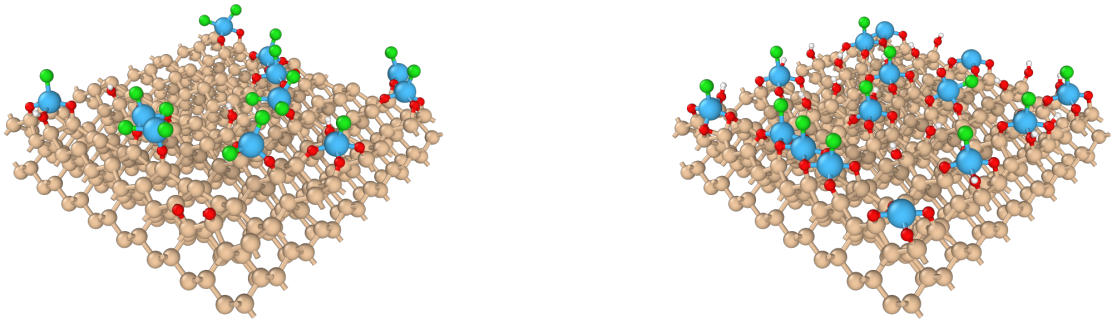

(a) 50% OH *coverage* (b) 100% OH *coverage*

Figure 5.11 *The (a)* 50% OH *coverage and (b)* 100% OH *coverage surface after the* $HfCl_4$ *pulse, first cycle. (Colour:* H - *white,* O - *red,* Si - *beige,* Cl - *green,* Hf - *azure).*

In all three slabs, it is noticeable that there were unreacted OH groups on the surface after precursor exposure. It suggests that in one cycle, the growth of a full mono-layer cannot be achieved due to several reasons, such as steric hindrance or unsuccessful reactions [12]. This sub-mono-layer growth behaviour of ALD of HfO_2 was experimentally reported by Green et al. [72], stating that only 14% coverage of an oxide mono-layer could be achieved each cycle in the most favourable conditions.

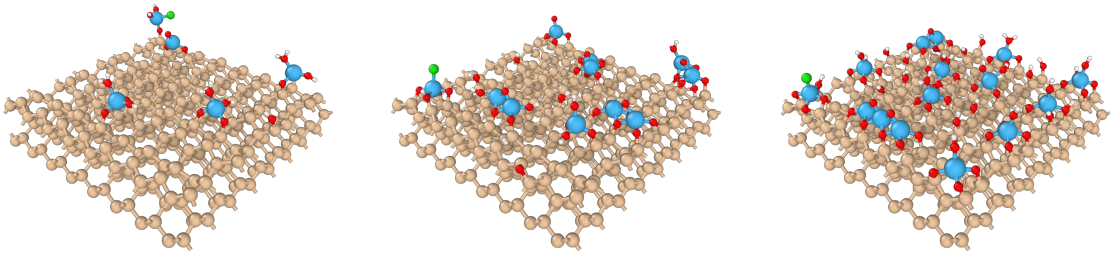

(a) 10% OH *coverage* (b) 50% OH *coverage* (c) 100% OH *coverage*

Figure 5.12 *The (a)* 10% OH *coverage, (b)* 50% OH *coverage and (c)* 100% OH *coverage surface after the* H_2O *pulse, first cycle. (Colour:* H - *white,* O - *red,* Si - *beige,* Cl - *green,* Hf - *azure).*

Next, after the first H_2O pulse, the surface configurations of the three slabs are illustrated in Figure 5.12. Almost all chlorine atoms were replaced with either OH groups or double-bonded O atoms. Additionally, water molecules could be physisorbed on surface Si atoms or deposited Hf atoms, becoming new reaction sites in subsequent ALD cycles. Another growth phenomenon that was observed, especially when surface species were densely packed, is the densification of the film: OH groups of nearby $Hf(OH)_x$ species react to form oxygen bridges between Hf atoms [55, 52]. This mechanism is demonstrated more clearly when juxtaposing surface configurations before the deposition, after the $HfCl_4$ phase, and after the H_2O phase of the first ALD cycle (see Figure 5.13 and Figure 5.14).

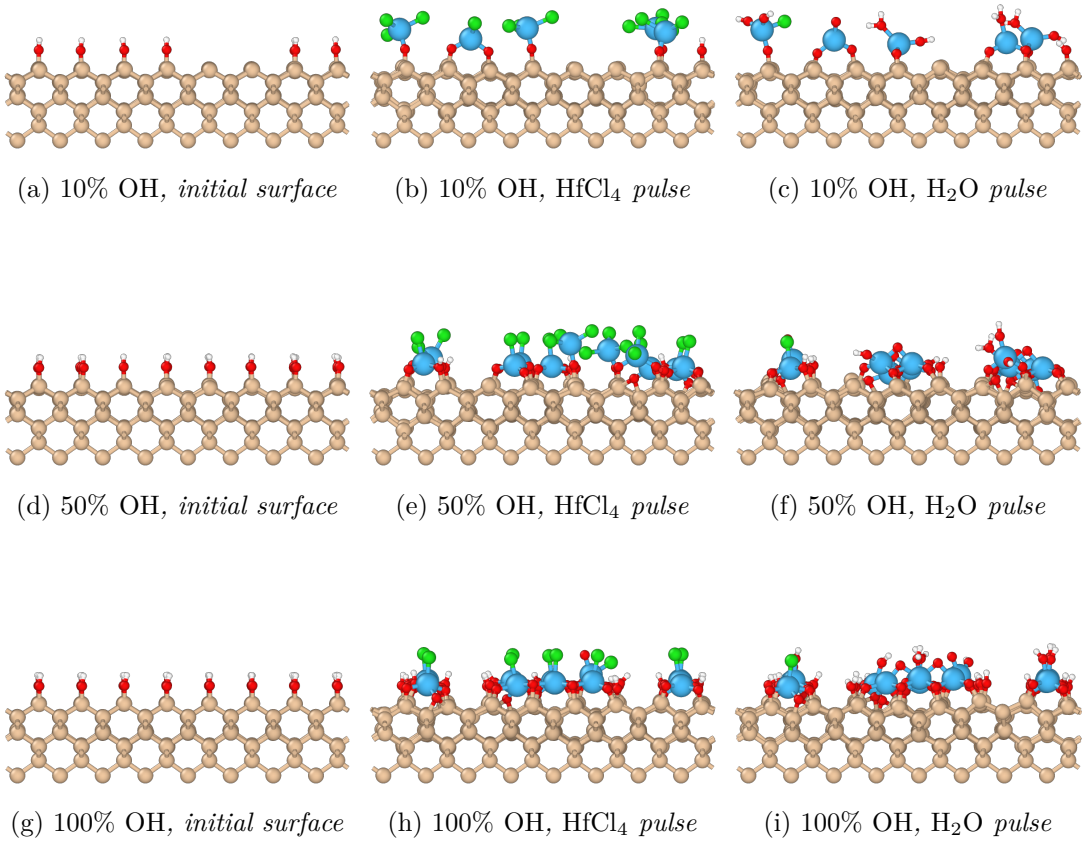

(a) 10% OH, *initial surface* (b) 10% OH, $HfCl_4$ *pulse* (c) 10% OH, H_2O *pulse*

(d) 50% OH, *initial surface* (e) 50% OH, $HfCl_4$ *pulse* (f) 50% OH, H_2O *pulse*

(g) 100% OH, *initial surface* (h) 100% OH, $HfCl_4$ *pulse* (i) 100% OH, H_2O *pulse*

Figure 5.13 *Side view of the initial surface and the surface after each pulse of the first cycle. (Colour:* H - *white,* O - *red,* Si - *beige,* Cl - *green,* Hf - *azure).*

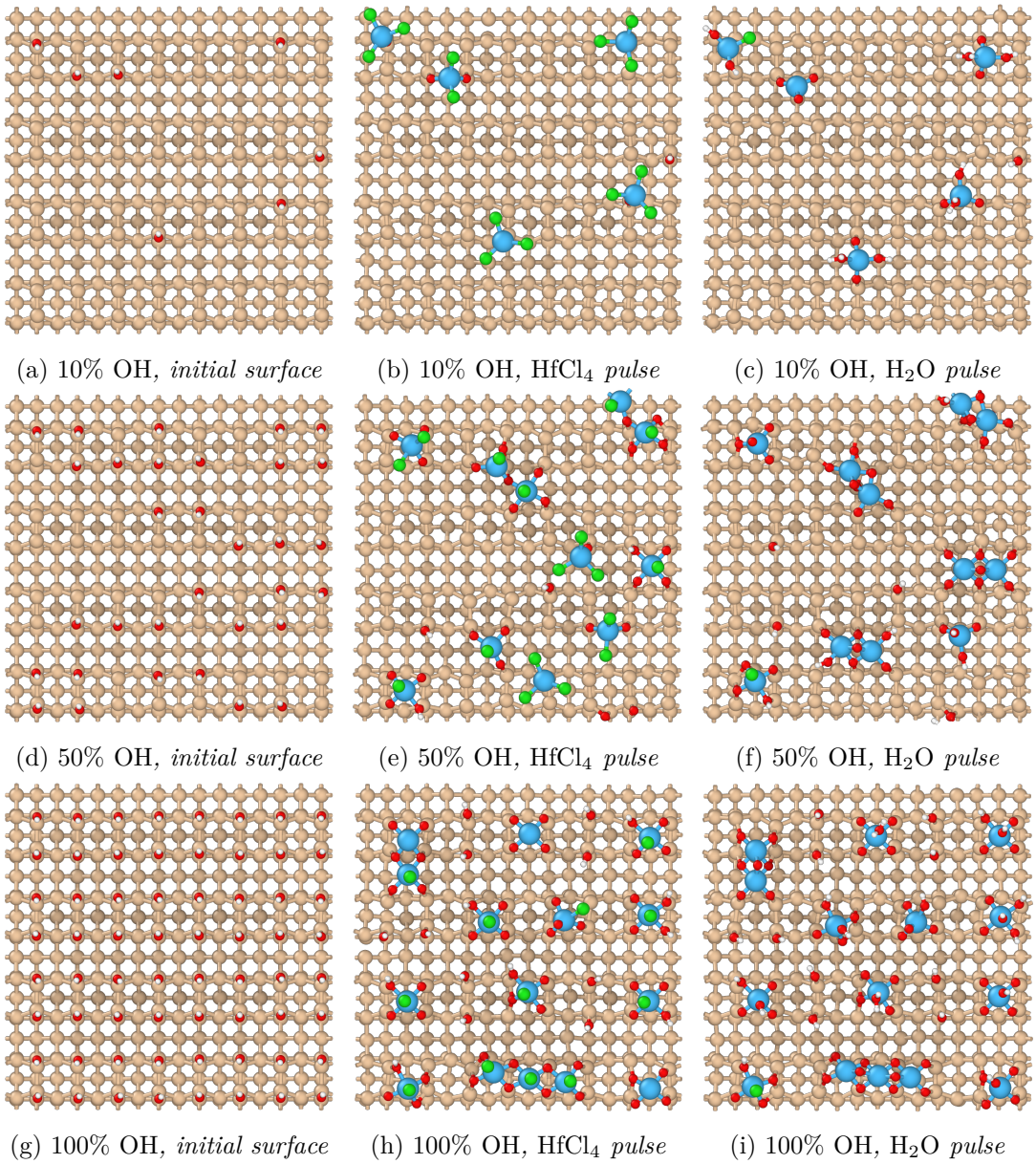

(a) 10% OH, *initial surface* (b) 10% OH, $HfCl_4$ *pulse* (c) 10% OH, H_2O *pulse*

(d) 50% OH, *initial surface* (e) 50% OH, $HfCl_4$ *pulse* (f) 50% OH, H_2O *pulse*

(g) 100% OH, *initial surface* (h) 100% OH, $HfCl_4$ *pulse* (i) 100% OH, H_2O *pulse*

Figure 5.14 *Top view of the initial surface and the surface after each pulse of the first cycle. (Colour:* H - *white,* O - *red,* Si - *beige,* Cl - *green,* Hf - *azure).*

After the first cycle, simulations of the ALD process were carried out for four more cycles. The surface and thin film configurations after each of the five cycles are shown in Figure 5.15, Figure 5.16, and Figure 5.17 for the 10%, 50%, and 100% OH-covered surfaces, respectively.

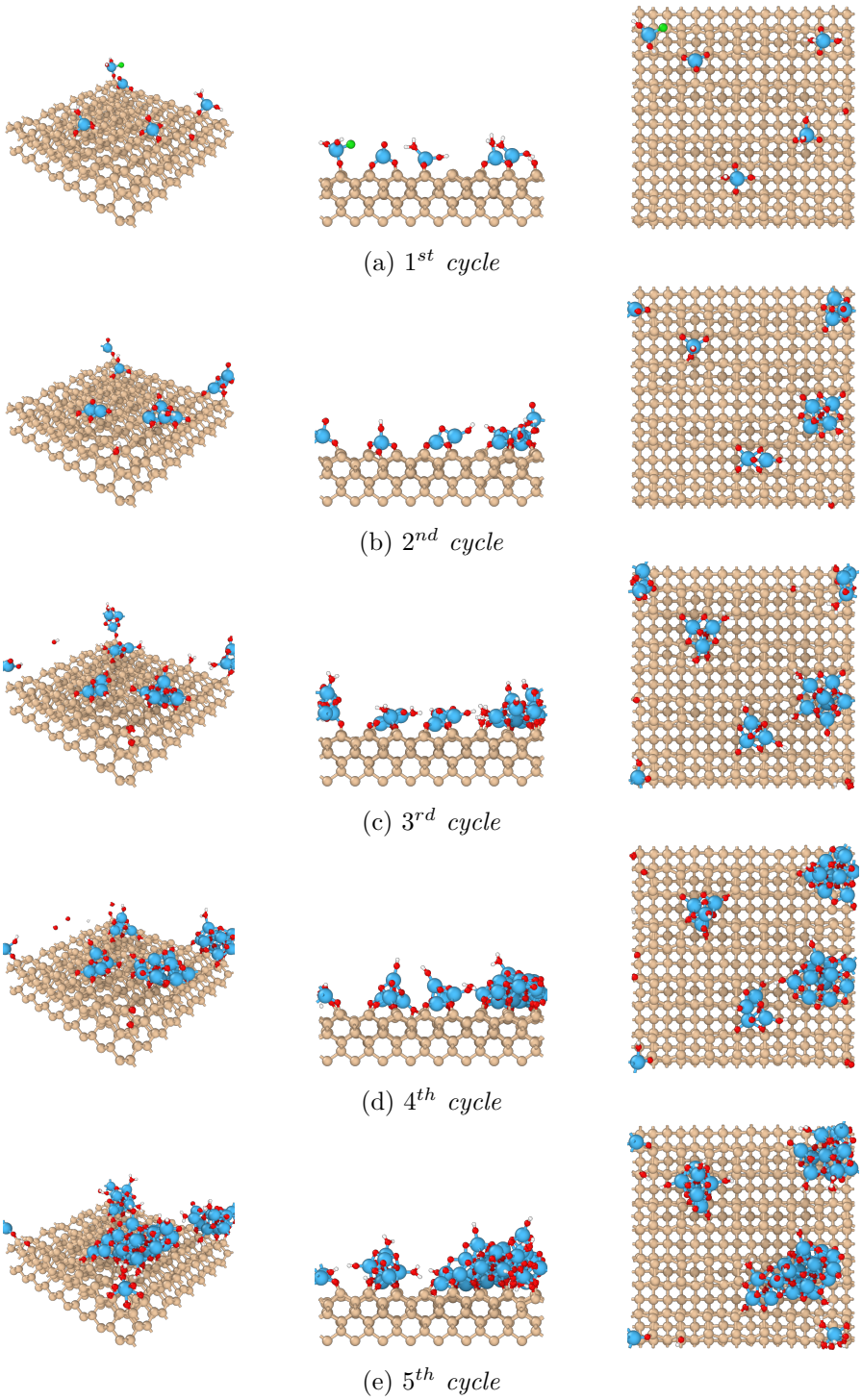

(a) 1^{st} *cycle*

(b) 2^{nd} *cycle*

(c) 3^{rd} *cycle*

(d) 4^{th} *cycle*

(e) 5^{th} *cycle*

Figure 5.15 *The surface configuration after each of the first five ALD cycles,* 10% OH *coverage. (Colour:* H - *white,* O - *red,* Si - *beige,* Cl - *green,* Hf - *azure).*

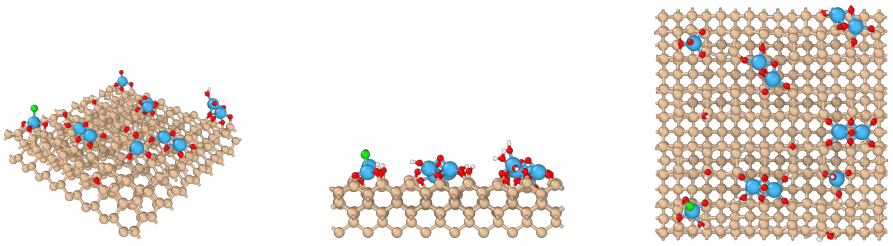

(a) 1^{st} *cycle*

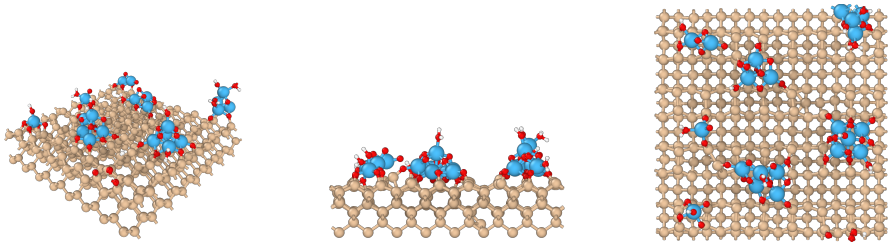

(b) 2^{nd} *cycle*

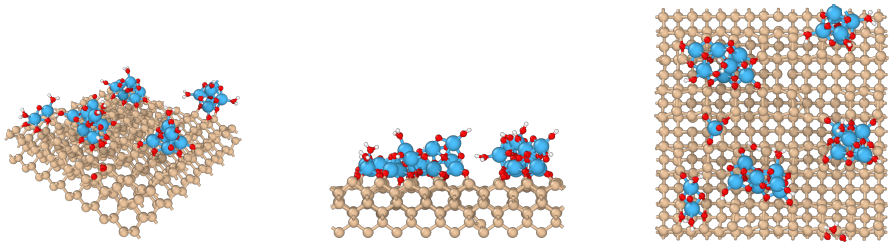

(c) 3^{rd} *cycle*

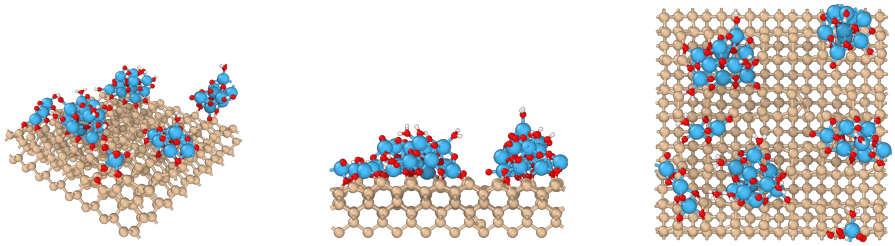

(d) 4^{th} *cycle*

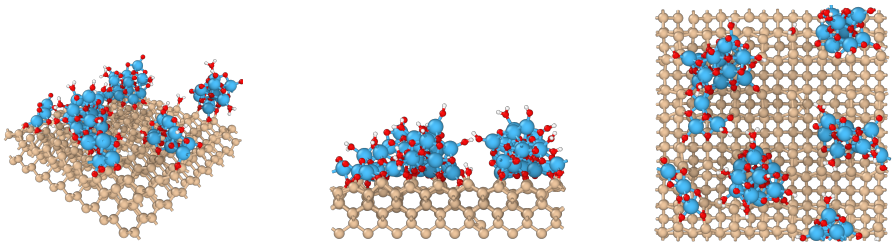

(e) 5^{th} *cycle*

Figure 5.16 *The surface configuration after each of the first five ALD cycles,* 50% OH *coverage. (Colour:* H - *white,* O - *red,* Si - *beige,* Cl - *green,* Hf - *azure).*

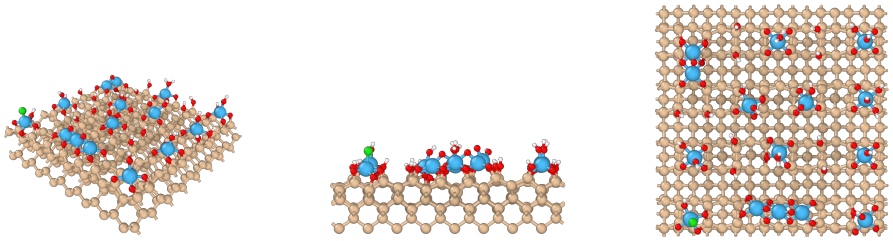

(a) 1^{st} *cycle*

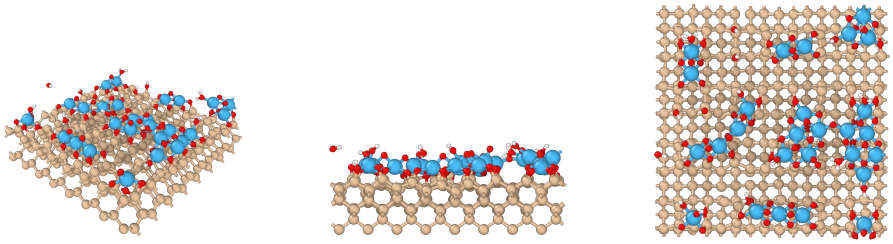

(b) 2^{nd} *cycle*

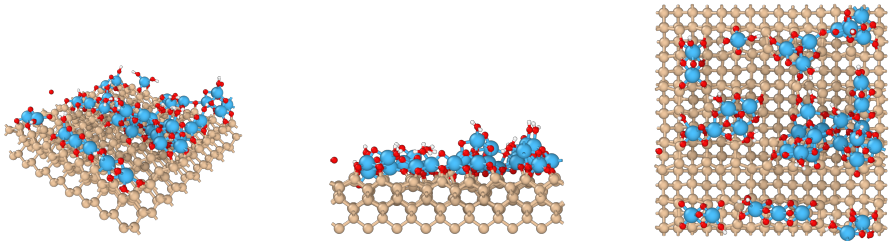

(c) 3^{rd} *cycle*

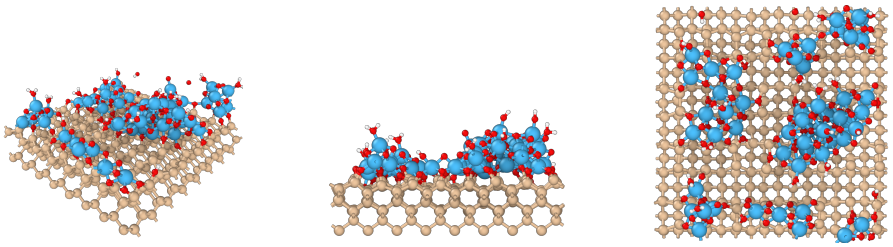

(d) 4^{th} *cycle*

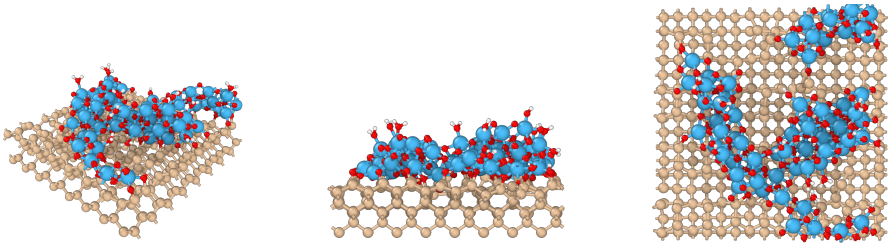

(e) 5^{th} *cycle*

Figure 5.17 *The surface configuration after each of the first five ALD cycles,* 100% OH *coverage. (Colour:* H - *white,* O - *red,* Si - *beige,* Cl - *green,* Hf - *azure).*

In the case where OH groups were scarce on the initial surface (see Figure 5.15), a very three-dimensional growth was observed. Because the nucleation barrier on already grown $Hf(OH)_x$ surface species is much lower than on Si atoms, $HfCl_4$ precursors favoured chemisorption on previously deposited HfO_2 islands. Furthermore, geographical isolation among these islands exaggerated this non-uniform growth, resulting in a rugged, non-conformal thin film. This observation agrees with experimental data on Si surface with low OH coverage, typical of the HF-last treatment [72]. In cases where more OH groups were present on the initial surface, the deposited film exhibited a less three-dimensional, more uniform growth all over the surface, albeit island growth was still evident.

The film thickness expressed in the Hf concentration level after each simulation cycle is plotted in Figure 5.18. As predicted by the growth mechanism, deposition on the 50% and 100% OH coverage surface demonstrates linear growth, with the growth rate slightly higher in the latter case. The 10% OH-covered surface, on the other hand, exhibits a non-linear growth due to the lack of reaction sites and high nucleation barrier during the first few cycles of the ALD process. This is in accordance with the results obtained from experiments by Green et al. [72], presented in Figure 5.19. Although the non-linear growth will eventually slow down and enter the linear regime after many cycles [72, 73], running many MD simulations to achieve similar trends is extremely cumbersome and is not covered in this thesis.

From the linear regression fit from data points of the growth on the fully OH-saturated surface, the slope of the blue dashed line, i.e., the Growth per Cycle (GPC) is extracted to be 1.42 Hf/nm^2. This growth rate is comparable with several experimental studies on ALD of HfO_2 from $HfCl_4/H_2O$, which are reported in Table 5.1. Comparing to the Hf concentration of 2.7×10^{15} Hf/cm^2 at $1nm$ of full-density HfO_2 film, the GPC value of 1.42 Hf/nm^2 could be translated to 0.53Å per cycle.

Table 5.1 *GPC of ALD of* HfO_2 *comparison among various studies.*

Study	**GPC (Hf/nm^2)**
Green et al. [72]	1.26
Delabie et al. [75]	$1.40 - 1.80$
Nyns et al. [14]	$1.20 - 1.50$
This work	*1.42*

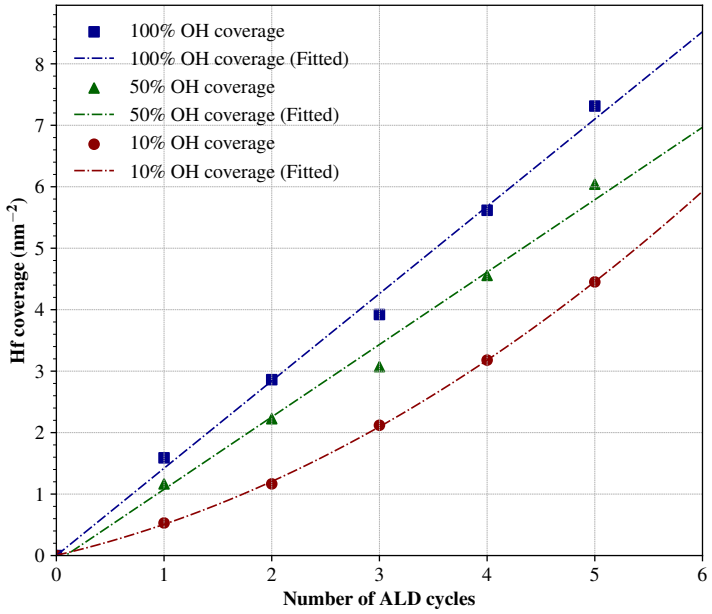

Figure 5.18 *The thickness of the* HfO_2 *film in* Hf/nm^2 *plotted against the number of ALD cycles (simulation data).*

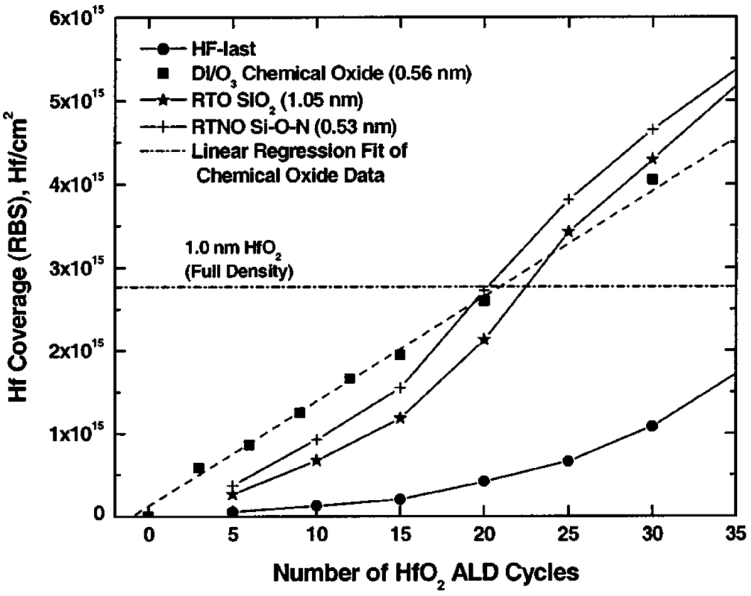

Figure 5.19 *The thickness of the* HfO_2 *film in* Hf/nm^2 *plotted against the number of ALD cycles, experimentally reported by Green et al. [72].*

Chapter 6

Characterisation of the Hafnium Dioxide film

In the previous chapter, the growth mechanism of the ALD process of HfO_2 film on the Si surface from $HfCl_4$ and H_2O was thoroughly investigated. However, it is also important to understand the physical and electrical properties of the deposited film and its influence on the performance of miniature electronic devices which adopt HfO_2 high-κ material. Therefore, in this chapter, the HfO_2 film obtained from MD simulations was analysed with quantum mechanics methods to extract material parameters, which could be used to accurately emulate the operation of devices in Technology Computer-Aided Design (TCAD) software.

TCAD is a computer program that models semiconductor fabrication (Process TCAD) and semiconductor device operation (Device TCAD) through numerical simulations. It has proven its usability in numerous applications, including CMOS, memory, optoelectronics, analogue/radio-frequency, and power electronics. In this work, all device simulations were conducted using the Synopsys Sentaurus[1] modelling suite, while quantum mechanics calculations were done with Synopsys QuantumATK[2] software.

[1] https://www.synopsys.com/silicon/tcad/device-simulation/sentaurus-device.html

[2] https://www.synopsys.com/silicon/quantumatk.html

6.1 Dielectric properties of HfO_2

6.1.1 HfO_2 film structure

Although it would be more precise to extract the dielectric properties from a HfO_2 film that fully covers the Si slab, carrying out that task is impractical. Firstly, after 5 ALD cycles, none of the three slabs was fully covered by a uniform layer of HfO_2. To achieve such a uniform film, many more cycles would be required. Secondly, the computational power needed to perform quantum mechanics calculations on the entire film is enormous. Therefore, in this work, an approximation approach was utilised to facilitate the characterisation of the HfO_2 film.

In this approximation approach, a sample portion of the as-deposited HfO_2 film was taken from the Si surface with 100% initial OH coverage. The sample contained 5 Hf atoms and 10 O atoms to perfectly imitate a stoichiometric HfO_2 structure. The sample was then enclosed inside a three-dimensional cell with PBC imposed on all faces, and geometrically optimised to obtain a stable configuration, which is illustrated in Figure 6.1a. This configuration was considered the unit cell of the HfO_2 film deposited by ALD. To provide a reference point, a unit cell of the monoclinic HfO_2 crystal is shown in Figure 6.1b.

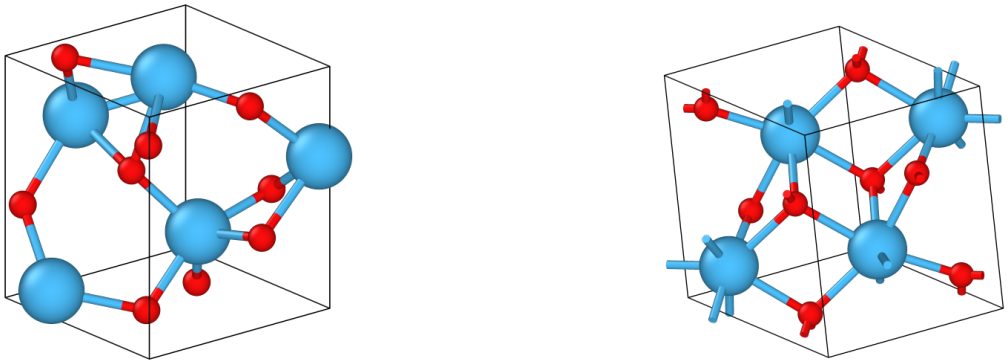

(a) *As-deposited* HfO_2 (b) *Monoclinic* HfO_2

Figure 6.1 *The unit cell of two* HfO_2 *configurations: (a) As-deposited* HfO_2*, (b) Monoclinic* HfO_2*. (Colour:* O *- red,* Hf *- azure).*

The coordination number of Hf atoms in the two unit cells is shown in Figure 6.2. Since monoclinic HfO_2 is crystalline, the Hf coordination number is constant at 7. It means that a Hf atom always forms single bonds with seven neighbouring O atoms and that periodicity is maintained throughout the monoclinic HfO_2 crystal. On the other hand, Hf atoms in the deposited HfO_2 unit cell have varied coordination numbers from 5

to 7, demonstrating a randomly distributed, non-periodic structure.

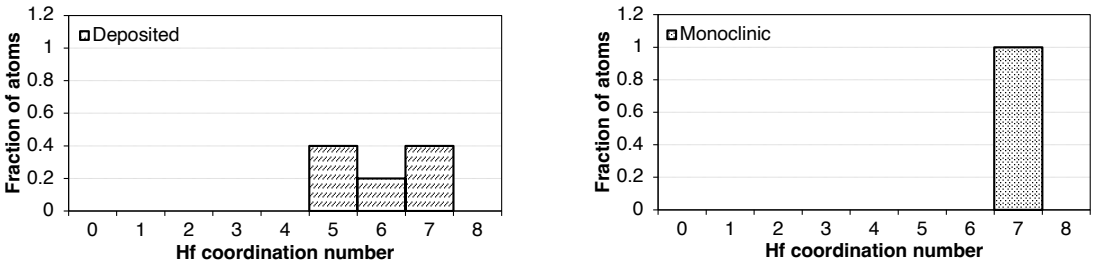

(a) *As-deposited* HfO_2 (b) *Monoclinic* HfO_2

Figure 6.2 *Distribution of the coordination number of* Hf *atoms in the* HfO_2 *unit cell: (a) As-deposited* HfO_2*, (b) Monoclinic* HfO_2*.*

Further analysis of the radial distribution function[3] of Hf-O pairs in the two unit cells shows the same trend in Figure 6.3. While the monoclinic HfO_2 crystal has defined, high peaks at some specific distances, the deposited HfO_2 structure has a more spread-out distribution function with lower peaks. This result signifies that the deposited HfO_2 film had an amorphous structure, which is consistent with previous experimental studies that very thin HfO_2 film deposited by a low-temperature ALD process has an amorphous phase, and only crystallises if followed by a high-temperature anneal [85, 86, 87, 88].

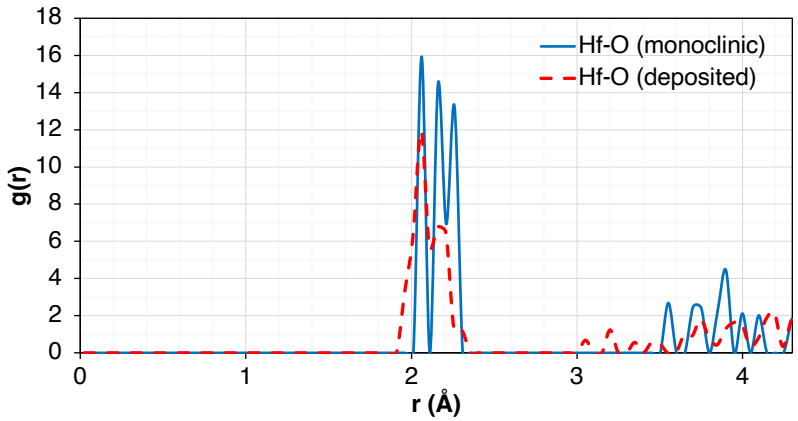

Figure 6.3 *Radial distribution function of* Hf-O *pairs in the two* HfO_2 *unit cells.*

[3]Radial distribution function is the function describing the possibility of finding other matters with respect to the distance from the reference particle.

6.1.2 Relative permittivity analysis

To extract the relative permittivity of the HfO_2 film, DFT and finite difference methods were employed to perform calculations on both HfO_2 unit cells. DFT calculations were carried out with the GGA-PBE exchange-correlation functionals, and the *double-zeta polarised* basis set at 60-Hartree mesh cutoff and a $5 \times 5 \times 5$ Monkhorst-Pack grid. The dynamical matrix was constructed by replicating the unit cell three times in every direction. The dielectric constant tensor of the amorphous and monoclinic HfO_2 in the x, y, and z directions, as well as their averaged values are reported in Table 6.1.

Table 6.1 *DFT-calculated dielectric tensor of* HfO_2 *configurations.*

	Amorphous HfO_2 ($a - HfO_2$)	**Monoclinic HfO_2 ($m - HfO_2$)**
ϵ_{xx}	18.45	25.97
ϵ_{yy}	18.59	21.47
ϵ_{zz}	19.66	17.71
$\epsilon = \frac{\epsilon_{xx}+\epsilon_{yy}+\epsilon_{zz}}{3}$	*18.90*	*21.72*

Both HfO_2 configurations were anisotropic with a different permittivity value along each axis. The relative permittivity of amorphous HfO_2 was found to be 18.9, which is lower than the value reported by Ceresoli et al. [89] at 22 and Wang et al. [90] at 24.5. However, the computed value still falls in the range of 16 to 25 as experimentally proven by Cherkaoui et al. [91]. For the crystalline structure, the value of nearly 22 agrees with the literature [89].

The discrepancy in the dielectric constant value with the other two studies may be due to the different procedures used to obtain the amorphous HfO_2 structure. The authors in [89] and [90] started from a bulk crystalline HfO_2 and ran melt-quench MD simulations to get the amorphous structure. In this work, the amorphous structure was taken from the as-deposited thin film from the ALD process. Thus, this result could be regarded as more reliable to compute the electrical properties of devices having ALD HfO_2 films.

6.2 Device simulations

To correctly model the tunnelling effect of charge carriers through the gate oxide, several parameters of the insulating material had to be provided to Sentaurus Device. Those parameters are listed in Table 6.2. While the static dielectric constant of amorphous HfO_2 was extracted from the quantum mechanics calculation, its band gap and electron effective mass was adopted from studies of Perevalov et al. [92] and Monaghan et al. [93],

respectively. Other parameters were left as is from the material database of Sentaurus Device. The complete parameter set is listed in Appendix C.

Table 6.2 *Parameters of* HfO_2 *material used for simulations in Sentaurus Device.*

	Amorphous HfO_2 ($a - HfO_2$)	**Monoclinic HfO_2 ($m - HfO_2$)**
Static dielectric constant ϵ	18.9	22.0
Band gap E_g	$5.7eV$ [92]	$5.9eV$
Electron effective mass m_e	$0.11m_0$ [93]	$0.42m_0$
Electron affinity χ	$2.05eV$	$2.05eV$

All of the devices to be investigated in this part were simple n-type MOSFETs with the gate length equals $40nm$. Unless explicitly stated otherwise, all nMOSFETs would have the same doping profile in the channel, source/drain region, and polycrystalline Si gate. The maximum voltage supply was $1V$.

6.2.1 HfO_2 versus SiO_2 gate oxide

First, three nMOSFETs with different single-layer gate oxides - SiO_2, $a-HfO_2$, or $m-HfO_2$ - were simulated to evaluate the influence of the dielectric material on the performance of the device. To achieve a $1nm$ of Equivalent Oxide Thickness (EOT), the thickness of the high-κ $a-HfO_2$ and $m-HfO_2$ layers were computed to be:

$$t_{a-HfO_2} = \frac{\epsilon_{a-HfO_2}}{\epsilon_{SiO_2}} \cdot t_{SiO_2} = \frac{18.9}{3.9} \cdot 1nm \approx 4.8nm$$

$$t_{m-HfO_2} = \frac{\epsilon_{m-HfO_2}}{\epsilon_{SiO_2}} \cdot t_{SiO_2} = \frac{22}{3.9} \cdot 1nm \approx 5.6nm$$

The final structure of the three devices are shown in Figure 6.4.

The most important figures of merit of the three MOSFETs are summarised in Table 6.3. Simulation results show that even though the three devices had the same EOT of $1nm$, there were some slight variations in the performance. For example, there were small shifts of the threshold voltage towards higher values when SiO_2 was replaced with HfO_2 as the gate dielectrics. These shifts resulted in smaller on-state drain current densities, from $0.24mA/\mu m$ to $0.22mA/\mu m$ and $0.19mA/\mu m$. Thicker oxide layers also greatly degraded the Sub-threshold Swing (SS) of the device, making off-state leakage currents higher. The leakage current in the $5.6nm$ $m-HfO_2$ device was more than double the same figure in the $1nm$ SiO_2 device. Altogether, the electrostatic control ratio slightly decreased as the thickness of the gate oxide layer increased.

Table 6.3 *Figures of merit of nMOSFETs with three different single-layer gate oxides:* SiO_2, $a-HfO_2$, *or* $m-HfO_2$.

	1nm SiO_2	**4.8nm $a-HfO_2$**	**5.6nm $m-HfO_2$**
$\mathbf{I_{off}}$ $(nA/\mu m)$	2.08	3.12	4.87
$\mathbf{I_{on}}$ $(mA/\mu m)$	0.24	0.22	0.19
$\mathbf{I_{on}/I_{off}}$	1.2×10^5	6.9×10^4	4.0×10^4
$\mathbf{V_{th}}$ (V)	0.425	0.434	0.428
SS $(mV/dec.)$	89.1	106.1	116.0
$\mathbf{I_{g,max}}$ (A/cm^2)	6.83×10^2	7.69×10^{-2}	2.27×10^{-13}

However, the most significant gain in performance when switching from SiO_2 to HfO_2 was the huge reduction in gate current: 4 orders of magnitude with amorphous HfO_2 and 15 orders of magnitude with monoclinic HfO_2. The gate current value on the order of mA/cm^2 and the attenuation factor of 4 when replacing SiO_2 with $a-HfO_2$ at the $40nm$ technology node is in good agreement with previous experimental studies [10, 94], while the 15-order-of-magnitude reduction in $I_{g,max}$ in the $m-HfO_2$ case seems too optimistic.

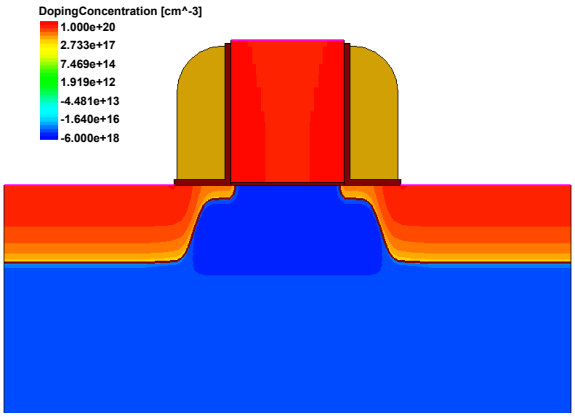

(a) $1nm$ SiO_2

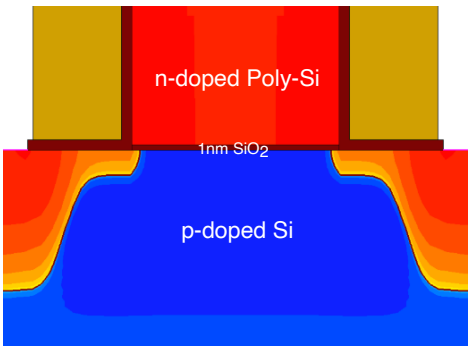

(b) $1nm$ SiO_2 *(zoomed-in)*

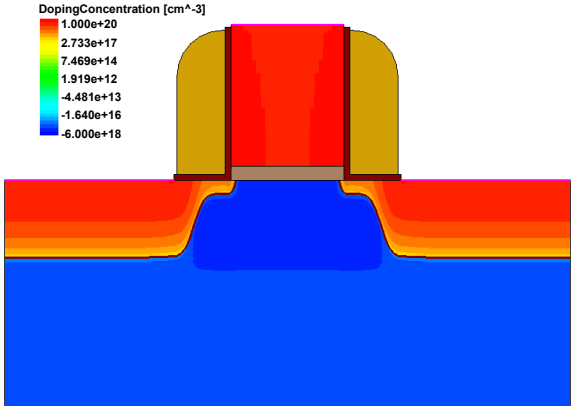

(c) $4.8nm$ a $-$ HfO_2

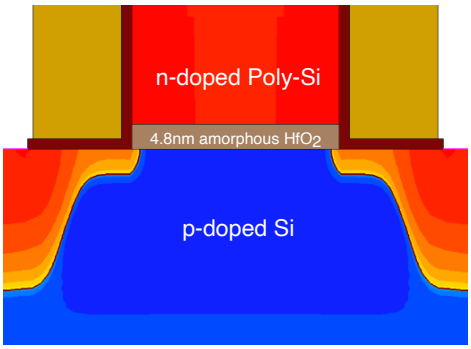

(d) $4.8nm$ a $-$ HfO_2 *(zoomed-in)*

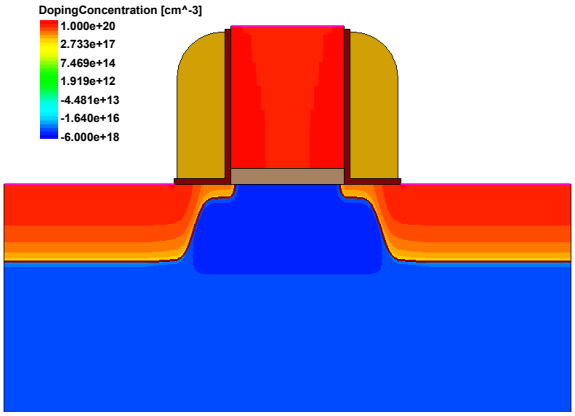

(e) $5.6nm$ m $-$ HfO_2

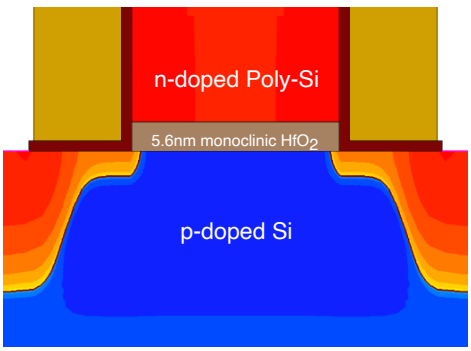

(f) $5.6nm$ m $-$ HfO_2 *(zoomed-in)*

Figure 6.4 *Structure of nMOSFETs with different single-layer gate oxides.*

Thanks to much higher dielectric constant values, the use of HfO_2 as the gate dielectric allows having a thicker insulating layer to obtain the same level of saturation current across the channel. Because the conduction mechanism of the gate current is direct tunnelling through the oxide barrier, its magnitude scales down exponentially as the barrier width, i.e., the gate oxide thickness grows. Thus, while the nMOSFET with $1nm$ SiO_2 gate oxide had a very high gate current density, the device with $4.8nm$ $a-HfO_2$ gate oxide had a value of gate current density well under the limit of $10A/cm^2$ for low-power applications. The gate current density of the three devices over the entire operating voltage range is plotted in Figure 6.5, and their trans-characteristics are depicted in Figure 6.6.

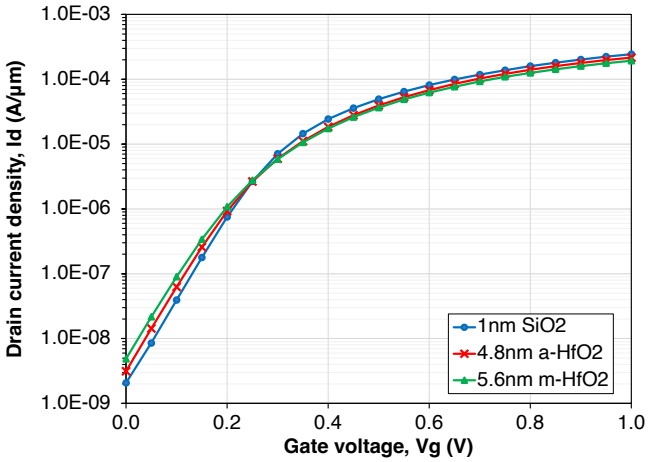

Figure 6.5 *I_d-V_g curve of nMOSFETs with three different single-layer gate oxides:* SiO_2, $a-HfO_2$, *or* $m-HfO_2$.

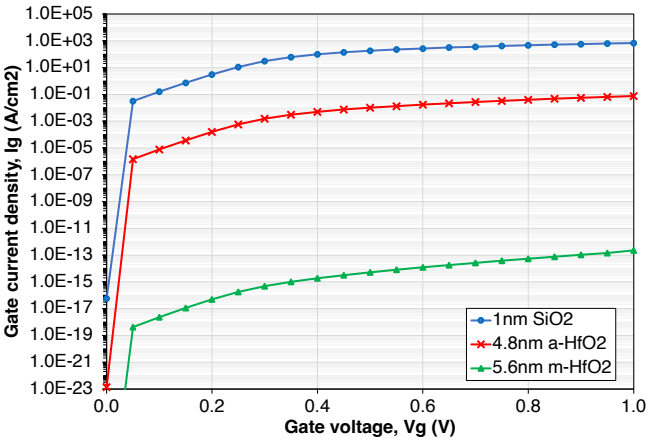

Figure 6.6 *I_g-V_g curve of nMOSFETs with three different single-layer gate oxides:* SiO_2, $a-HfO_2$, *or* $m-HfO_2$.

6.2.2 $SiO_2/a-HfO_2$ gate oxide stack

Figure 6.7 illustrates the band diagram of the gate/oxide/channel vertical structure in two cases: $1nm$ SiO_2 and $4.8nm$ $a-HfO_2$. The tunnelling barrier for electrons from the conduction band of the Si substrate to the conduction band of the polycrystalline Si gate is much higher with the SiO_2 layer (having a band gap of $9eV$) than with the $a-HfO_2$ layer (having a band gap of $5.7eV$). Since the tunnelling current grows at a faster rate with a reduction in the barrier energy than in the barrier width, the gate current may increase excessively if the oxide thickness is shorter than the desired value due to process variations. Additionally, several studies confirmed that there is always an interfacial SiO_2 or $HfSiO_x$ layer spontaneously formed when depositing HfO_2 directly on the Si substrate, which increases the EOT and negatively affects the performance of the device [10, 95]. Therefore, in practice, an interfacial SiO_2 layer is deliberately grown between the HfO_2 film and Si substrate to have better control of the gate oxide stack and maintain a good interface quality.

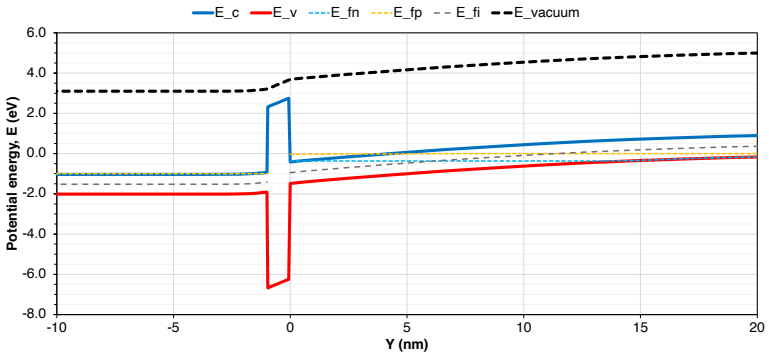

(a) $1nm$ SiO_2

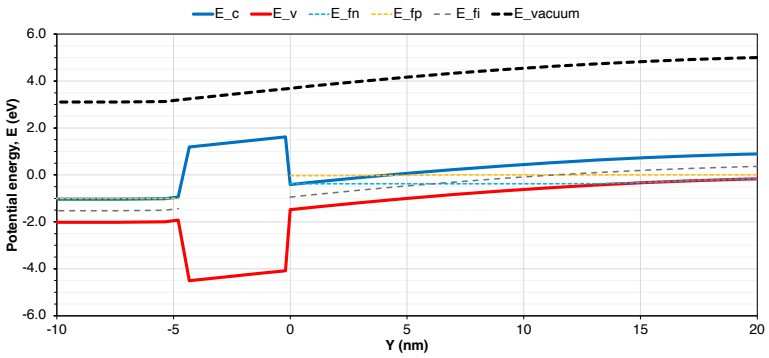

(b) $4.8nm$ $a-HfO_2$

Figure 6.7 *Band diagram of the gate stack of nMOSFETs with (a)* $1nm$ SiO_2 *and (b)* $4.8nm$ $a-HfO_2$ *gate oxide at* $V_{gs} = V_{ds} = 1V$.

In this part, a few combinations of the $SiO_2/a-HfO_2$ tandem were investigated: $0.75nm$ $SiO_2/1.2nm$ $a-HfO_2$, $0.5nm$ $SiO_2/2.4nm$ $a-HfO_2$, and $0.25nm$ $SiO_2/3.6nm$ $a-HfO_2$. These combinations were chosen solely due to the possibility to numerically obtain $1nm$ EOT without considering that some structures are not physically achievable, such as the $0.25nm$ $SiO_2/3.6nm$ $a-HfO_2$ configuration. The results were also compared with the $1nm$ SiO_2 and $4.8nm$ $a-HfO_2$ single-layer gate oxide.

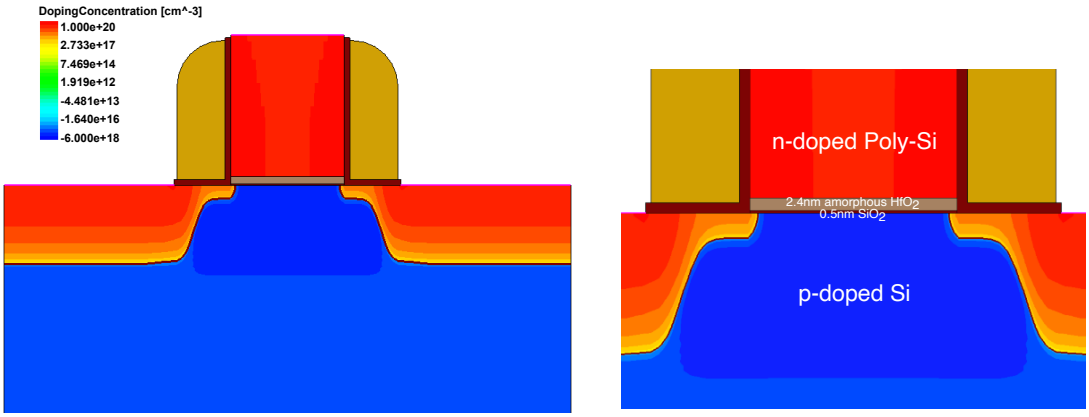

(a) $SiO_2/2.4nm$ $a-HfO_2$ (b) $SiO_2/2.4nm$ $a-HfO_2$ *(zoomed-in)*

Figure 6.8 *Structure of the nMOSFET with* $0.5nm$ $SiO_2/2.4nm$ $a-HfO_2$ *gate oxide.*

The maximum gate current, as well as saturation current and leakage current, are reported in Figure 6.9. Among five structures, the $0.5nm$ $SiO_2/2.4nm$ $a-HfO_2$ gate oxide stack (see Figure 6.8) achieved a decent performance in terms of I_{on}/I_{off} ratio while maintaining the gate current within the limit for low-power devices. However, due to the total physical thickness of the gate oxide stack, in this case, was $2.9nm$, the attenuation of the gate current was only 2 orders of magnitude.

The I_d-V_g curves of the $1nm$ SiO_2 and the $0.5nm$ $SiO_2/2.4nm$ $a-HfO_2$ devices are plotted in Figure 6.10, showing almost identical characteristics. The gate capacitance characteristics in Figure 6.11 also proves that the two gate oxide structures were equivalent. Nonetheless, the $0.5nm$ $SiO_2/2.4nm$ $a-HfO_2$ device had a 100-time smaller gate current density than the $1nm$ SiO_2 one thanks to the thicker physical barrier layer. The energy band diagram of the $0.5nm$ $SiO_2/2.4nm$ $a-HfO_2$ gate stack is depicted in Figure 6.12.

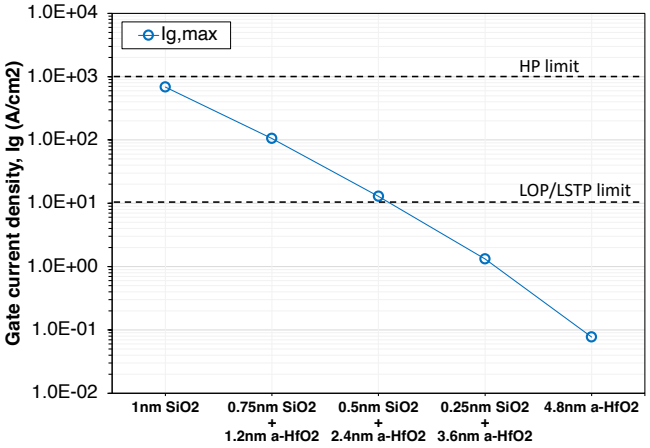

(a) $I_{g,max}$

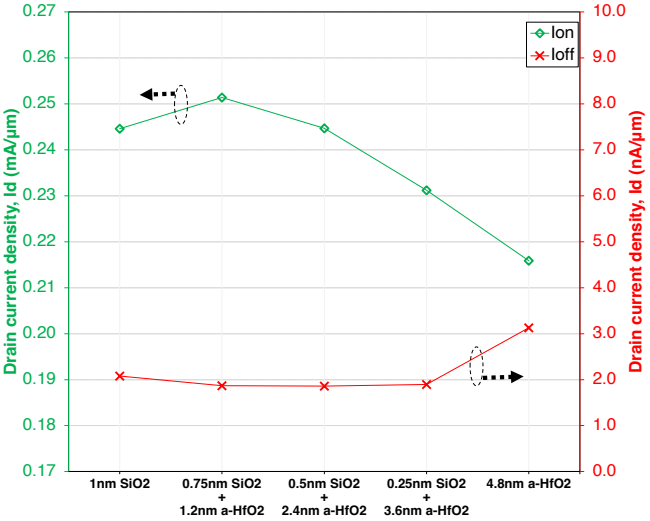

(b) I_{on}, I_{off}

Figure 6.9 *Maximum gate current, saturation current and leakage current of* 5 *nMOSFETs with* 1*nm EOT.*

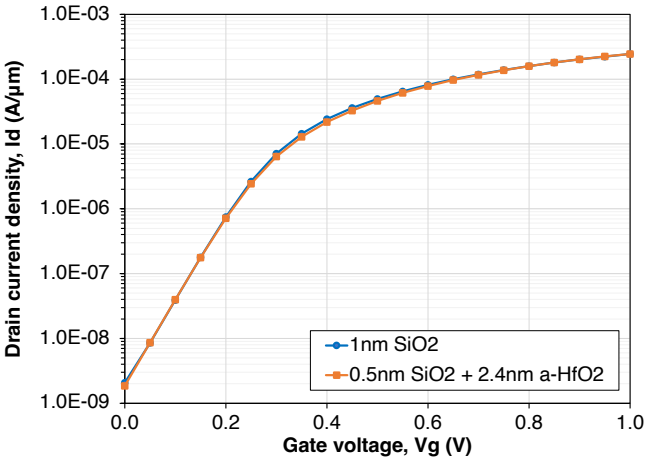

Figure 6.10 *I_d-V_g curve of the $1nm$ SiO_2 and the $0.5nm$ SiO_2/$2.4nm$ $a-HfO_2$ nMOSFETs.*

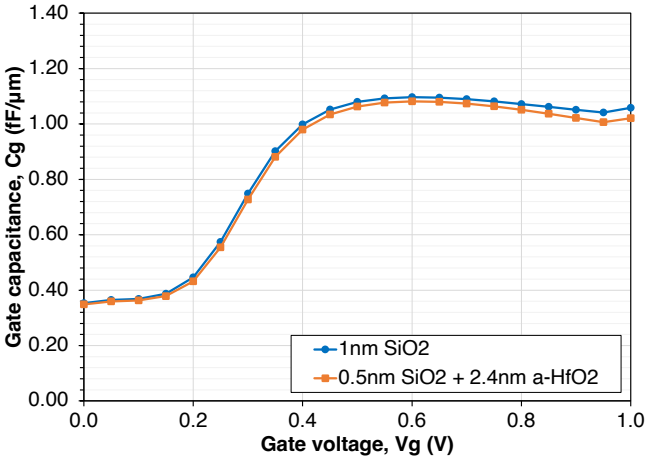

Figure 6.11 *C_g-V_g curve of the $1nm$ SiO_2 and the $0.5nm$ SiO_2/$2.4nm$ $a-HfO_2$ nMOSFETs.*

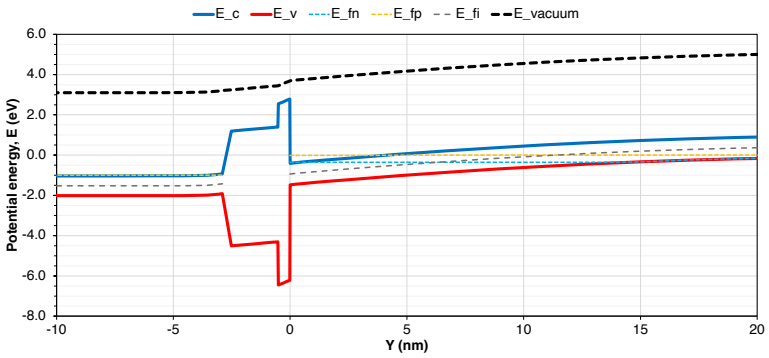

Figure 6.12 *Band diagram of the gate stack of the nMOSFET with* $0.5nm$ $SiO_2/2.4nm$ $a-HfO_2$ *gate oxide at* $V_{gs} = V_{ds} = 1V$.

6.2.3 High-κ/Metal-gate (HKMG)

In Figure 6.7 and Figure 6.12, the energy bands of the polycrystalline Si gate region next to the oxide are bent upwards demonstrating the poly-depletion effect. The poly-depletion effect introduces a depletion layer in the gate at the interface with the gate oxide, which acts as a capacitor in series with the oxide and the channel capacitors. Therefore, the effective potential appearing at the gate/gate oxide interface equals the potential applied at the gate contact minus an extra voltage drop across the poly-depletion capacitor, lowering the drain current under the channel when the device is turned on. With the shrinking of device dimensions, the supply voltage, and the introduction of high-κ dielectrics, Replaced Metal Gate (RMG) technology has been employed to mitigate the poly-depletion effect in polycrystalline Si gate, thus, improving the electrostatic control of the gate over the channel.

In this part, an HKMG structure was examined and compared to its polycrystalline Si counterpart. The nMOSFET was constructed with the same $0.5nm$ $SiO_2/2.4nm$ $a-HfO_2$ gate oxide stack and a titanium nitride (TiN) metal gate. The structure is illustrated in Figure 6.13, while its figures of merit are reported in Table 6.4.

Because the work function of TiN was higher than that of n-doped polycrystalline Si, $4.66eV$ compared to about $4.08eV$, the flat band voltage of the MOS capacitor was higher in the HKMG structure, which in turn raised the threshold voltage of the MOSFET. This resulted in extremely low on-state and off-state drain currents. However, the I_{on}/I_{off} ratio was very high compared to the device with the polycrystalline Si gate, which suggests that the device structure could be optimised to obtain a lower V_{th} and better performance.

Next, the doping profile of the HKMG nMOSFET was modified by lowering the channel doping concentration to reduce the threshold voltage of the transistor. The tweaked

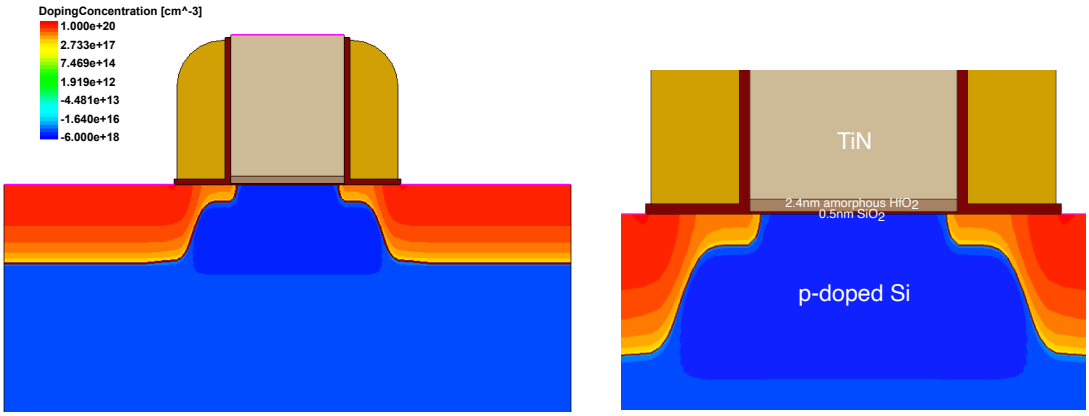

(a) $SiO_2/a-HfO_2$, TiN *gate* (b) $SiO_2/a-HfO_2$, TiN *gate (zoomed-in)*

Figure 6.13 *Structure of the nMOSFET with* $0.5nm$ $SiO_2/2.4nm$ $a-HfO_2$ *gate oxide and* TiN *gate.*

Table 6.4 *Figures of merit of nMOSFETs with polycrystalline* Si *gate and* TiN *gate.*

	Polycrystalline Si	TiN
$\mathbf{I_{off}}$ $(nA/\mu m)$	1.86	4.10×10^{-7}
$\mathbf{I_{on}}$ $(mA/\mu m)$	0.24	0.06
$\mathbf{I_{on}/I_{off}}$	1.3×10^5	1.5×10^{11}
$\mathbf{V_{th}}$ (V)	0.421	0.825
SS $(mV/dec.)$	90.8	72.2
$\mathbf{I_{g,max}}$ (A/cm^2)	12.86	2.30

device structure is shown in Figure 6.14, and the total doping concentration of a one-dimensional cut along the channel of the original and tweaked device is illustrated in Figure 6.15. The acceptor concentration in the p-doped channel was reduced by nearly one order of magnitude while the donor concentration remained the same, making the effective concentration in the source/drain region near the channel appeared a little higher. That is the reason why the source/drain extensions in the modified MOSFET expanded slightly deeper than the original one.

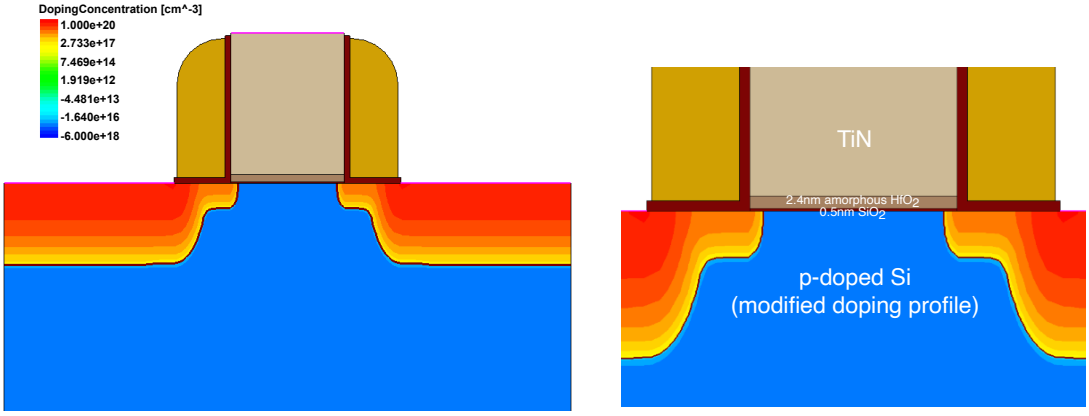

(a) TiN *gate, tweaked* (b) TiN *gate, tweaked (zoomed-in)*

Figure 6.14 *Structure of the nMOSFET with* $0.5nm$ SiO_2/$2.4nm$ $a-HfO_2$ *gate oxide,* TiN *gate, and a modified doping profile.*

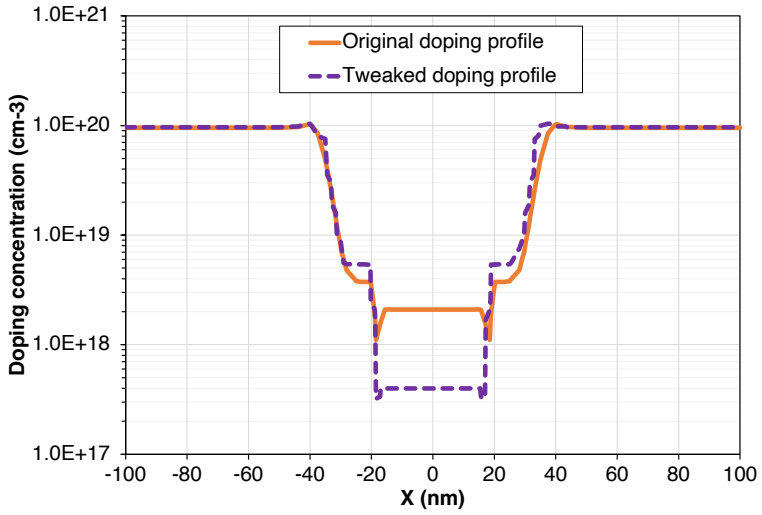

Figure 6.15 *Doping concentration along the channel of nMOSFETs with the original and modified doping profile.*

Table 6.5 summarises the operating characteristics of the tweaked HKMG device and the original polycrystalline Si-gate device. At the threshold voltage of $0.596V$, the HKMG device demonstrated superior performance in terms of 50% higher saturation current, 3-order-of-magnitude less leakage current, better electrostatic control, and smaller Subthreshold Swing, all thanks to the elimination of the poly-depletion effect.

Table 6.5 *Figures of merit of nMOSFETs with polycrystalline* Si *gate (original doping profile) and* TiN *gate (tweaked doping profile).*

	Polycrystalline Si	TiN (tweaked)
$\mathbf{I_{off}}$ $(nA/\mu m)$	1.86	1.80×10^{-3}
$\mathbf{I_{on}}$ $(mA/\mu m)$	0.24	0.35
$\mathbf{I_{on}/I_{off}}$	1.3×10^{5}	1.9×10^{8}
$\mathbf{V_{th}}$ (V)	0.421	0.596
SS $(mV/dec.)$	90.8	77.2
$\mathbf{I_{g,max}}$ (A/cm^2)	12.86	2.92

Furthermore, substituting the polycrystalline Si gate with the TiN metal gate diminished the gate tunnelling current by another order of magnitude. This improvement can be explained by comparing the band diagram of the MOS capacitor in the two cases in Figure 6.12 and Figure 6.16. Because the work function of the polycrystalline Si gate was smaller than the TiN gate, the silicon's conduction band was closer to the conduction band of the $a-HfO_2$ layer. When the gate voltage was applied, the conduction band of the $a-HfO_2$ layer at the polycrystalline Si-gate side was pulled down more aggressively compared to the metal gate device, lowering the effective barrier of the gate oxide stack. Thus, the tunnelling current through the gate dielectrics in the polycrystalline Si-gate MOSFET was larger than in the TiN-gate transistor.

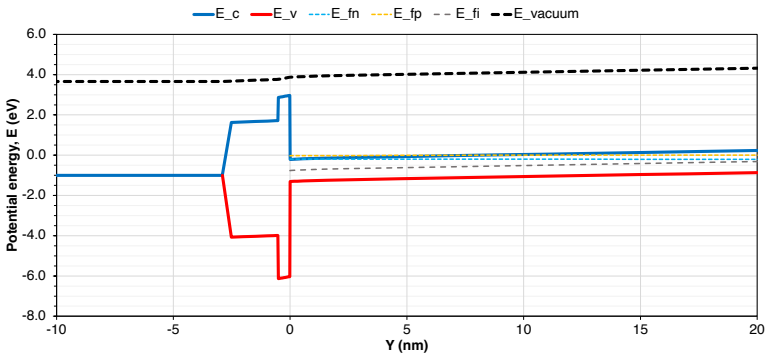

Figure 6.16 *Band diagram of the gate stack of the nMOSFET with* $0.5nm$ $SiO_2/2.4nm$ $a-HfO_2$ *gate oxide,* TiN *gate, and tweaked doping profile at* $V_{gs} = V_{ds} = 1V$.

Finally, the trans-characteristics and output characteristics of the two devices are shown in Figure 6.17 and Figure 6.18, respectively. Overall, the nMOSFET with TiN gate and tweaked doping profile had excellent figures of merit as a scaled device for low-power applications.

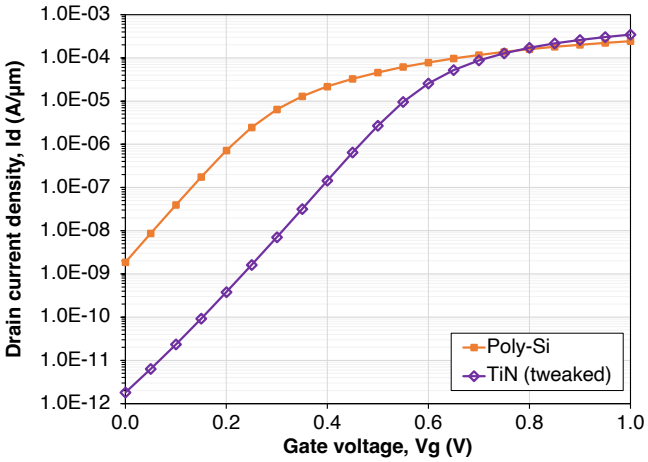

Figure 6.17 *I_d-V_g curve of nMOSFETs with polycrystalline* Si *gate (original doping profile) and* TiN *gate (tweaked doping profile).*

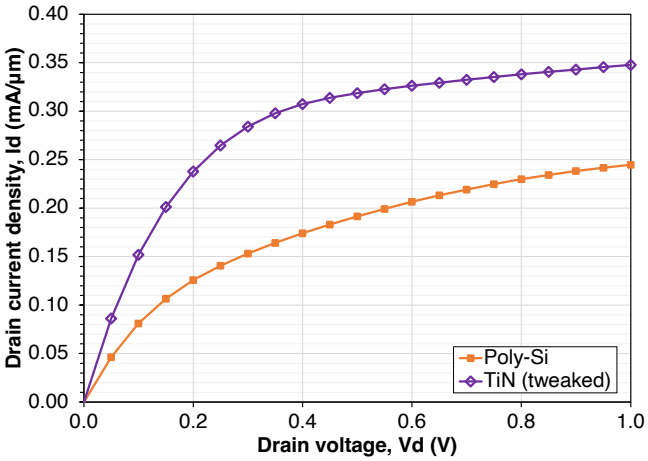

Figure 6.18 *I_d-V_d curve of nMOSFETs with polycrystalline* Si *gate (original doping profile) and* TiN *gate (tweaked doping profile).*

Chapter 7

Conclusions and future work

This thesis has developed a complete procedure to study the characteristics of the ALD of hafnium dioxide thin film on silicon substrates and its influence on the performance of nanoscale microelectronic devices. The deposition mechanism was thoroughly investigated with quantum mechanics computations involving various chemical species and surface reactions. Then, an empirical force field was generalised, enabling molecular simulations of the ALD process on larger and longer scales. Simulations were able to moderately describe the growth mechanism of the HfO_2 film on different surface conditions and predict the growth rate of 1.42 Hf/nm^2 (or 0.53Å) per cycle, which is in good agreement with reported data from experiments. Next, quantum mechanics methods were employed again to extract the physical and electrical properties of the deposited thin film. The extracted quantities were utilised to construct a material parameter set to correctly model the operation of transistors with high-κ gate dielectrics in TCAD simulations. Results showed that by substituting SiO_2 with HfO_2, the gate tunnelling current was reduced by 3 - 4 orders of magnitude, which is in accordance with experimental and modelled statistics. The use of high-κ materials as gate dielectrics, therefore, has allowed device dimensions to be scaled down continuously but with power dissipation still kept in limit, especially for low-power applications.

However, the model developed in this work still has some caveats. First, the reactive force field was trained only with chemical reaction data. While this is adequate, other properties, such as mechanical stress, can play a crucial role in the deposition process and could be incorporated into the force field's parameters. Second, to shorten the simulation time, the flow rate of precursor molecules was set to an unrealistically high value. The consequence was that the surface's temperature rose very quickly due to continuous collisions with gas molecules, which also accelerated undesirable side reactions. Finally, due

to limited computational resources, the characterisation of the HfO_2 film was done with small-sized basis sets and loose constraints regarding a large-core element like hafnium. Thus, using a more sophisticated analysis would shift the extracted values, and eventually, alter the results of device simulations by a small extent.

For the next steps, there are a number of improvements and extensions that can be made. The developed reactive force field serves as a baseline so that it can be re-parameterised with additional elements, enabling simulations of the ALD process on different types of substrate and with various precursor species. With computer simulations, a lot of time and effort to conduct experiments would be saved. Furthermore, the extracted parameter of amorphous HfO_2 film can be utilised to accurately model the operation and measure figures of merit of more advanced device structures, e.g., finFET, GAA-FET, TFET, and so on.

Overall, this work has proven the possibility to combine quantum mechanics, molecular dynamics and TCAD simulations to accurately model the characteristics of microelectronic devices, which is becoming more and more important as devices are breaking into the sub-nanometre regime.

Bibliography

[1] "IRDS™ 2022: Executive summary - IEEE IRDS™."

[2] D. Frank, R. Dennard, E. Nowak, P. Solomon, Y. Taur, and H.-S. P. Wong, "Device scaling limits of Si MOSFETs and their application dependencies," vol. 89, no. 3, pp. 259–288. Conference Name: Proceedings of the IEEE.

[3] D. A. Muller, T. Sorsch, S. Moccio, F. H. Baumann, K. Evans-Lutterodt, and G. Timp, "The electronic structure at the atomic scale of ultrathin gate oxides," vol. 399, no. 6738, pp. 758–761. Number: 6738 Publisher: Nature Publishing Group.

[4] H. Wong and H. Iwai, "On the scaling issues and high-κ replacement of ultrathin gate dielectrics for nanoscale MOS transistors," vol. 83, no. 10, pp. 1867–1904.

[5] S.-H. Lo, D. Buchanan, Y. Taur, and W. Wang, "Quantum-mechanical modeling of electron tunneling current from the inversion layer of ultra-thin-oxide nMOSFET's," vol. 18, no. 5, pp. 209–211. Conference Name: IEEE Electron Device Letters.

[6] J. C. Ranuárez, M. Deen, and C.-H. Chen, "A review of gate tunneling current in mos devices," *Microelectronics Reliability*, vol. 46, no. 12, pp. 1939–1956, 2006.

[7] G. D. Wilk, R. M. Wallace, and J. M. Anthony, "High-κ gate dielectrics: Current status and materials properties considerations," vol. 89, no. 10, pp. 5243–5275. Publisher: American Institute of Physics.

[8] H. Y. Yang, H. Niimi, and G. Lucovsky, "Tunneling currents through ultrathin oxide/nitride dual layer gate dielectrics for advanced microelectronic devices," vol. 83, no. 4, pp. 2327–2337. Publisher: American Institute of Physics.

[9] E. Bersch, S. Rangan, R. A. Bartynski, E. Garfunkel, and E. Vescovo, "Band offsets of ultrathin high-κ oxide films with Si," vol. 78, no. 8, p. 085114. Publisher: American Physical Society.

[10] L. Kang, K. Onishi, Y. Jeon, B. H. Lee, C. Kang, W.-J. Qi, R. Nieh, S. Gopalan, R. Choi, and J. Lee, "MOSFET devices with polysilicon on single-layer HfO_2 high-k

dielectrics," in *International Electron Devices Meeting 2000. Technical Digest. IEDM (Cat. No.00CH37138)*, pp. 35–38.

[11] D. Sibanda, S. T. Oyinbo, and T.-C. Jen, "A review of atomic layer deposition modelling and simulation methodologies: Density functional theory and molecular dynamics:," vol. 11, no. 1, pp. 1332–1363. Publisher: De Gruyter.

[12] R. L. Puurunen, "Surface chemistry of atomic layer deposition: A case study for the trimethylaluminum/water process," vol. 97, no. 12, p. 121301. Publisher: American Institute of Physics.

[13] C. S. Hwang, ed., *Atomic Layer Deposition for Semiconductors*. Springer US.

[14] L. Nyns, A. Delabie, M. Caymax, M. M. Heyns, S. V. Elshocht, C. Vinckier, and S. D. Gendt, "HfO_2 atomic layer deposition using $HfCl_4/H_2O$: The first reaction cycle," vol. 16, no. 4, p. 257. Publisher: IOP Publishing.

[15] P. Hohenberg and W. Kohn, "Inhomogeneous electron gas," vol. 136, no. 3, pp. B864–B871. Publisher: American Physical Society.

[16] V. Sahni, K. P. Bohnen, and M. K. Harbola, "Analysis of the local-density approximation of density-functional theory," vol. 37, no. 6, pp. 1895–1907. Publisher: American Physical Society.

[17] J. P. Perdew, K. Burke, and M. Ernzerhof, "Generalized gradient approximation made simple," vol. 77, no. 18, pp. 3865–3868. Publisher: American Physical Society.

[18] R. G. Parr, "Density functional theory of atoms and molecules," in *Horizons of Quantum Chemistry* (K. Fukui and B. Pullman, eds.), Académie Internationale Des Sciences Moléculaires Quantiques / International Academy of Quantum Molecular Science, pp. 5–15, Springer Netherlands.

[19] R. G. Parr and Y. Weitao, *Density-Functional Theory of Atoms and Molecules*. Oxford University Press. Google-Books-ID: mGOpScSIwU4C.

[20] W. Koch and M. C. Holthausen, *A Chemist's Guide to Density Functional Theory*. John Wiley & Sons. Google-Books-ID: qm5cCwAAQBAJ.

[21] L. Verlet, "Computer "experiments" on classical fluids. i. thermodynamical properties of lennard-jones molecules," vol. 159, no. 1, pp. 98–103. Publisher: American Physical Society.

[22] D. Frenkel and B. Smit, *Understanding Molecular Simulation: From Algorithms to Applications*. Academic Press, 2nd edition ed.

[23] H. C. Andersen, "Molecular dynamics simulations at constant pressure and/or temperature," vol. 72, no. 4, pp. 2384–2393. Publisher: American Institute of Physics.

[24] H. J. C. Berendsen, J. P. M. Postma, W. F. van Gunsteren, A. DiNola, and J. R. Haak, "Molecular dynamics with coupling to an external bath," vol. 81, no. 8, pp. 3684–3690. Publisher: American Institute of Physics.

[25] S. Nosé, "A unified formulation of the constant temperature molecular dynamics methods," vol. 81, no. 1, pp. 511–519. Publisher: American Institute of Physics.

[26] W. G. Hoover, "Canonical dynamics: Equilibrium phase-space distributions," vol. 31, no. 3, pp. 1695–1697. Publisher: American Physical Society.

[27] M. Parrinello and A. Rahman, "Crystal structure and pair potentials: A molecular-dynamics study," vol. 45, no. 14, pp. 1196–1199. Publisher: American Physical Society.

[28] G. J. Martyna, M. E. Tuckerman, D. J. Tobias, and M. L. Klein, "Explicit reversible integrators for extended systems dynamics," vol. 87, no. 5, pp. 1117–1157. Publisher: Taylor & Francis _eprint: https://doi.org/10.1080/00268979600100761.

[29] A. P. Thompson, H. M. Aktulga, R. Berger, D. S. Bolintineanu, W. M. Brown, P. S. Crozier, P. J. in 't Veld, A. Kohlmeyer, S. G. Moore, T. D. Nguyen, R. Shan, M. J. Stevens, J. Tranchida, C. Trott, and S. J. Plimpton, "LAMMPS - a flexible simulation tool for particle-based materials modeling at the atomic, meso, and continuum scales," vol. 271, p. 108171.

[30] A. Stukowski, "Visualization and analysis of atomistic simulation data with OVITO–the open visualization tool," vol. 18, no. 1, p. 015012.

[31] J. E. Jones and S. Chapman, "On the determination of molecular fields. —II. from the equation of state of a gas," vol. 106, no. 738, pp. 463–477. Publisher: Royal Society.

[32] F. H. Stillinger and T. A. Weber, "Computer simulation of local order in condensed phases of silicon," vol. 31, no. 8, pp. 5262–5271. Publisher: American Physical Society.

[33] D. W. Brenner, "Relationship between the embedded-atom method and tersoff potentials," vol. 63, no. 9, pp. 1022–1022. Publisher: American Physical Society.

[34] K. Albe, K. Nordlund, and R. S. Averback, "Modeling the metal-semiconductor interaction: Analytical bond-order potential for platinum-carbon," vol. 65, no. 19, p. 195124. Publisher: American Physical Society.

[35] J. Tersoff, "New empirical approach for the structure and energy of covalent systems," vol. 37, pp. 6991–7000. ADS Bibcode: 1988PhRvB..37.6991T.

[36] D. W. Brenner, "Empirical potential for hydrocarbons for use in simulating the chemical vapor deposition of diamond films," vol. 42, pp. 9458–9471. ADS Bibcode:

1990PhRvB..42.9458B.

[37] A. C. T. van Duin, S. Dasgupta, F. Lorant, and W. A. Goddard, "ReaxFF: a reactive force field for hydrocarbons," vol. 105, no. 41, pp. 9396–9409. Publisher: American Chemical Society.

[38] J. Byggmästar, "Development of interatomic potentials in the tersoff-albe formalism for metal compounds," 2016.

[39] J. Behler and M. Parrinello, "Generalized neural-network representation of high-dimensional potential-energy surfaces," vol. 98, no. 14, p. 146401. Publisher: American Physical Society.

[40] A. P. Bartók, M. C. Payne, R. Kondor, and G. Csányi, "Gaussian approximation potentials: The accuracy of quantum mechanics, without the electrons," vol. 104, no. 13, p. 136403. Publisher: American Physical Society.

[41] A. V. Shapeev, "Moment tensor potentials: a class of systematically improvable interatomic potentials," vol. 14, no. 3, pp. 1153–1173.

[42] I. Novoselov, A. Yanilkin, A. Shapeev, and E. Podryabinkin, "Moment tensor potentials as a promising tool to study diffusion processes," vol. 164, pp. 46–56.

[43] I. S. Novikov, K. Gubaev, E. V. Podryabinkin, and A. V. Shapeev, "The MLIP package: moment tensor potentials with MPI and active learning," vol. 2, no. 2, p. 025002. Publisher: IOP Publishing.

[44] J. C. Fogarty, H. M. Aktulga, A. Y. Grama, A. C. T. van Duin, and S. A. Pandit, "A reactive molecular dynamics simulation of the silica-water interface," vol. 132, no. 17, p. 174704. Publisher: American Institute of Physics.

[45] F. Weigend and R. Ahlrichs, "Balanced basis sets of split valence, triple zeta valence and quadruple zeta valence quality for h to rn: Design and assessment of accuracy," vol. 7, no. 18, pp. 3297–3305. Publisher: The Royal Society of Chemistry.

[46] D. Andrae, U. Häußermann, M. Dolg, H. Stoll, and H. Preuß, "Energy-adjusted ab initio pseudopotentials for the second and third row transition elements," vol. 77, no. 2, pp. 123–141.

[47] X. Xu and D. G. Truhlar, "Accuracy of effective core potentials and basis sets for density functional calculations, including relativistic effects, as illustrated by calculations on arsenic compounds," vol. 7, no. 9, pp. 2766–2779. Publisher: American Chemical Society.

[48] R. D. Fenno, M. D. Halls, and K. Raghavachari, "Hafnium oxide and zirconium oxide atomic layer deposition: Initial precursor and potential side-reaction product

pathways with H/Si(100)-2×1," vol. 109, no. 11, pp. 4969–4976. Publisher: American Chemical Society.

[49] A. Estève, M. Djafari Rouhani, L. Jeloaica, and D. Estève, "DFT investigation of $HfCl_4$ decomposition on hydroxylated SiO_2: first stage of HfO_2 atomic layer deposition," vol. 27, no. 1, pp. 75–80.

[50] L. Jeloaica, A. Estève, M. Djafari Rouhani, and D. Estève, "Density functional theory study of $HfCl_4$, $ZrCl_4$, and $Al(CH_3)_3$ decomposition on hydroxylated SiO_2: Initial stage of high-k atomic layer deposition," vol. 83, no. 3, pp. 542–544. Publisher: American Institute of Physics.

[51] J. Ren, Y.-T. Zhang, and D. W. Zhang, "Density functional theory study of initial stage of HfO_2 atomic layer deposition on hydroxylated SiO_2 surface," vol. 803, no. 1, pp. 23–28.

[52] A. Dkhissi, A. Estève, C. Mastail, S. Olivier, G. Mazaleyrat, L. Jeloaica, and M. Djafari Rouhani, "Multiscale modeling of the atomic layer deposition of HfO_2 thin film grown on silicon: How to deal with a kinetic monte carlo procedure," vol. 4, no. 11, pp. 1915–1927. Publisher: American Chemical Society.

[53] B.-E. Park, I.-K. Oh, C. W. Lee, G. Lee, Y.-H. Shin, C. Lansalot-Matras, W. Noh, H. Kim, and H.-B.-R. Lee, "Effects of Cl-based ligand structures on atomic layer deposited HfO_2," vol. 120, no. 11, pp. 5958–5967. Publisher: American Chemical Society.

[54] W. Chen, H.-L. Lu, D. W. Zhang, M. Xu, J. Ren, J.-Y. Zhang, J.-T. Wang, and L.-K. Wang, "Density functional theory study of adsorption and dissociation of $HfCl_4$ and H_2O on GeSi(100)-(2×1): Initial stage of atomic layer deposition of HfO_2 on SiGe surface," vol. 86, no. 14, p. 142901. Publisher: American Institute of Physics.

[55] M. Deminsky, A. Knizhnik, I. Belov, S. Umanskii, E. Rykova, A. Bagatur'yants, B. Potapkin, M. Stoker, and A. Korkin, "Mechanism and kinetics of thin zirconium and hafnium oxide film growth in an ALD reactor," vol. 549, no. 1, pp. 67–86.

[56] B. G. Willis, A. Mathew, L. S. Wielunski, and R. L. Opila, "Adsorption and reaction of $HfCl_4$ with H_2O-terminated Si(100)-2×1," vol. 112, no. 6, pp. 1994–2003. Publisher: American Chemical Society.

[57] G. Henkelman, B. P. Uberuaga, and H. Jónsson, "A climbing image nudged elastic band method for finding saddle points and minimum energy paths," vol. 113, no. 22, pp. 9901–9904. Publisher: American Institute of Physics.

[58] Z. Fang and D. A. Dixon, "Hydrolysis of $ZrCl_4$ and $HfCl_4$: The initial steps in the high-temperature oxidation of metal chlorides to produce ZrO_2 and HfO_2," vol. 117,

no. 15, pp. 7459–7474. Publisher: American Chemical Society.

[59] R. Salomon-Ferrer, A. W. Götz, D. Poole, S. Le Grand, and R. C. Walker, "Routine microsecond molecular dynamics simulations with AMBER on GPUs. 2. explicit solvent particle mesh ewald," vol. 9, no. 9, pp. 3878–3888. Publisher: American Chemical Society.

[60] D. E. Shaw, J. Grossman, J. A. Bank, B. Batson, J. A. Butts, J. C. Chao, M. M. Deneroff, R. O. Dror, A. Even, C. H. Fenton, A. Forte, J. Gagliardo, G. Gill, B. Greskamp, C. R. Ho, D. J. Ierardi, L. Iserovich, J. S. Kuskin, R. H. Larson, T. Layman, L.-S. Lee, A. K. Lerer, C. Li, D. Killebrew, K. M. Mackenzie, S. Y.-H. Mok, M. A. Moraes, R. Mueller, L. J. Nociolo, J. L. Peticolas, T. Quan, D. Ramot, J. K. Salmon, D. P. Scarpazza, U. B. Schafer, N. Siddique, C. W. Snyder, J. Spengler, P. T. P. Tang, M. Theobald, H. Toma, B. Towles, B. Vitale, S. C. Wang, and C. Young, "Anton 2: Raising the bar for performance and programmability in a special-purpose molecular dynamics supercomputer," in *SC '14: Proceedings of the International Conference for High Performance Computing, Networking, Storage and Analysis*, pp. 41–53. ISSN: 2167-4337.

[61] S.-Y. Kim and A. C. T. van Duin, "Simulation of titanium metal/titanium dioxide etching with chlorine and hydrogen chloride gases using the ReaxFF reactive force field," vol. 117, no. 27, pp. 5655–5663.

[62] T. Cheng, A. Jaramillo-Botero, W. A. I. Goddard, and H. Sun, "Adaptive accelerated ReaxFF reactive dynamics with validation from simulating hydrogen combustion," vol. 136, no. 26, pp. 9434–9442. Publisher: American Chemical Society.

[63] D. H. Kim, S. J. Kwak, J. H. Jeong, S. Yoo, S. K. Nam, Y. Kim, and W. B. Lee, "Molecular dynamics simulation of silicon dioxide etching by hydrogen fluoride using the reactive force field," vol. 6, no. 24, pp. 16009–16015. Publisher: American Chemical Society.

[64] A. F. Voter, "A method for accelerating the molecular dynamics simulation of infrequent events," vol. 106, no. 11, pp. 4665–4677. Publisher: American Institute of Physics.

[65] M. R. Sørensen and A. F. Voter, "Temperature-accelerated dynamics for simulation of infrequent events," vol. 112, no. 21, pp. 9599–9606. Publisher: American Institute of Physics.

[66] A. F. Voter, "Parallel replica method for dynamics of infrequent events," vol. 57, no. 22, pp. R13985–R13988. Publisher: American Physical Society.

[67] M. J. Mees, G. Pourtois, E. C. Neyts, B. J. Thijsse, and A. Stesmans, "Uniform-acceptance force-bias monte carlo method with time scale to study solid-state diffusion," vol. 85, no. 13, p. 134301. Publisher: American Physical Society.

[68] S. Bradley, *Computational Modelling of Oxygen Defects and Interfaces in Monoclinic* HfO_2. UCL (University College London).

[69] N. Hansen, "The CMA evolution strategy: A tutorial," no. arXiv:1604.00772.

[70] M. Ritala, M. Leskelä, L. Niinistö, T. Prohaska, G. Friedbacher, and M. Grasserbauer, "Development of crystallinity and morphology in hafnium dioxide thin films grown by atomic layer epitaxy," vol. 250, no. 1, pp. 72–80.

[71] J. Aarik, A. Aidla, A. A. Kiisler, T. Uustare, and V. Sammelselg, "Influence of substrate temperature on atomic layer growth and properties of HfO_2 thin films," vol. 340, no. 1, pp. 110–116.

[72] M. L. Green, M.-Y. Ho, B. Busch, G. D. Wilk, T. Sorsch, T. Conard, B. Brijs, W. Vandervorst, P. I. Räisänen, D. Muller, M. Bude, and J. Grazul, "Nucleation and growth of atomic layer deposited HfO_2 gate dielectric layers on chemical oxide (Si–O–H) and thermal oxide (SiO_2 or Si–O–N) underlayers," vol. 92, no. 12, pp. 7168–7174. Publisher: American Institute of Physics.

[73] M. A. Alam and M. L. Green, "Mathematical description of atomic layer deposition and its application to the nucleation and growth of HfO_2 gate dielectric layers," vol. 94, no. 5, pp. 3403–3413. Publisher: American Institute of Physics.

[74] E. P. Gusev, C. Cabral, M. Copel, C. D'Emic, and M. Gribelyuk, "Ultrathin HfO_2 films grown on silicon by atomic layer deposition for advanced gate dielectrics applications," vol. 69, no. 2, pp. 145–151.

[75] A. Delabie, M. Caymax, B. Brijs, D. Brunco, T. Conard, E. Sleeckx, L.-A. Ragnarsson, S. Van Elshocht, S. De Gendt, and M. Heyns, "Growth studies and reaction mechanism of the atomic layer deposition of hafnium oxide," vol. 1, no. 5, pp. 433–446.

[76] M. Cho, R. Degraeve, G. Pourtois, A. Delabie, L.-A. Ragnarsson, T. Kauerauf, G. Groeseneken, S. De Gendt, M. Heyns, and C. S. Hwang, "Study of the reliability impact of chlorine precursor residues in thin atomic-layer-deposited HfO_2 layers," vol. 54, no. 4, pp. 752–758. Conference Name: IEEE Transactions on Electron Devices.

[77] Y. Zheng, S. Hong, G. Psofogiannakis, G. B. Rayner, S. Datta, A. C. van Duin, and R. Engel-Herbert, "Modeling and in situ probing of surface reactions in atomic layer deposition," vol. 9, no. 18, pp. 15848–15856. Publisher: American Chemical Society.

[78] D. Romine and R. Sakidja, "Modeling atomic layer deposition of alumina using reactive force field molecular dynamics," vol. 7, no. 9, pp. 185–189.

[79] A. Ramstad, G. Brocks, and P. J. Kelly, "Theoretical study of the Si(100) surface reconstruction," vol. 51, no. 20, pp. 14504–14523.

[80] C.-S. Guo, K. Hermann, and Y. Zhao, "Dynamics and energetics of reconstruction at the Si(100) surface," vol. 118, no. 44, pp. 25614–25619. Publisher: American Chemical Society.

[81] E. Hildebrandt, J. Kurian, M. M. Müller, T. Schroeder, H.-J. Kleebe, and L. Alff, "Controlled oxygen vacancy induced p-type conductivity in HfO_{2x} thin films," vol. 99, no. 11, p. 112902. Publisher: American Institute of Physics.

[82] N. Kaiser, T. Vogel, A. Zintler, S. Petzold, A. Arzumanov, E. Piros, R. Eilhardt, L. Molina-Luna, and L. Alff, "Defect-stabilized substoichiometric polymorphs of hafnium oxide with semiconducting properties," vol. 14, no. 1, pp. 1290–1303. Publisher: American Chemical Society.

[83] J. Park, M. Cho, S. K. Kim, T. J. Park, S. W. Lee, S. H. Hong, and C. S. Hwang, "Influence of the oxygen concentration of atomic-layer-deposited HfO_2 films on the dielectric property and interface trap density," vol. 86, no. 11, p. 112907. Publisher: American Institute of Physics.

[84] J. Park, T. J. Park, M. Cho, S. K. Kim, S. H. Hong, J. H. Kim, M. Seo, C. S. Hwang, J. Y. Won, R. Jeong, and J.-H. Choi, "Influence of the oxygen concentration of atomic-layer-deposited HfO_2 gate dielectric films on the electron mobility of polycrystalline-si gate transistors," vol. 99, no. 9, p. 094501. Publisher: American Institute of Physics.

[85] K. Tapily, J. Jakes, P. R. Shrestha, D. Gu, H. Baumgart, and A. Elmustafa, "Comparison of nanomechanical behavior of the amorphous and crystalline phases of ALD HfO_2," vol. 16, no. 4, p. 269. Publisher: IOP Publishing.

[86] X.-Y. Zhang, C.-H. Hsu, S.-Y. Lien, W.-Y. Wu, S.-L. Ou, S.-Y. Chen, W. Huang, W.-Z. Zhu, F.-B. Xiong, and S. Zhang, "Temperature-dependent HfO_2/si interface structural evolution and its mechanism," vol. 14, p. 83.

[87] S. Li, Y. Zhang, D. Yang, W. Yang, X. Chen, H. Zhao, J. Hou, and P. Yang, "Structure and optical properties of HfO_2 films on Si(100) substrates prepared by ALD at different temperatures," vol. 584, p. 412065.

[88] X.-Y. Zhang, J. Han, D.-C. Peng, Y.-J. Ruan, W.-Y. Wu, D.-S. Wuu, C.-J. Huang, S.-Y. Lien, and W.-Z. Zhu, "Crystallinity effect on electrical properties of PEALD–HfO_2 thin films prepared by different substrate temperatures," vol. 12, no. 21, p. 3890. Number: 21 Publisher: Multidisciplinary Digital Publishing Institute.

[89] D. Ceresoli and D. Vanderbilt, "Structural and dielectric properties of amorphous ZrO_2 and HfO_2," vol. 74, no. 12, p. 125108. Publisher: American Physical Society.

[90] Y. Wang, F. Zahid, J. Wang, and H. Guo, "Structure and dielectric properties of amorphous high-κ oxides: HfO_2, ZrO_2, and their alloys," vol. 85, no. 22, p. 224110. Publisher: American Physical Society.

[91] K. Cherkaoui, S. Monaghan, M. A. Negara, M. Modreanu, P. K. Hurley, D. O'Connell, S. McDonnell, G. Hughes, S. Wright, R. C. Barklie, P. Bailey, and T. C. Q. Noakes, "Electrical, structural, and chemical properties of HfO_2 films formed by electron beam evaporation," vol. 104, no. 6, p. 064113. Publisher: American Institute of Physics.

[92] T. V. Perevalov, V. A. Gritsenko, S. B. Erenburg, A. M. Badalyan, H. Wong, and C. W. Kim, "Atomic and electronic structure of amorphous and crystalline hafnium oxide: X-ray photoelectron spectroscopy and density functional calculations," vol. 101, no. 5, p. 053704. Publisher: American Institute of Physics.

[93] S. Monaghan, P. K. Hurley, K. Cherkaoui, M. A. Negara, and A. Schenk, "Determination of electron effective mass and electron affinity in HfO_2 using MOS and MOSFET structures," vol. 53, no. 4, pp. 438–444.

[94] L. Kang, B.-H. Lee, W.-J. Qi, Y.-J. Jeon, R. Nieh, S. Gopalan, K. Onishi, and J. C. Lee, "Highly reliable thin hafnium oxide gate dielectric," vol. 592, no. 1, pp. 101–106.

[95] S. Lee, H. Luan, W. Bai, C. Lee, T. Jeon, Y. Senzaki, D. Roberts, and D. Kwong, "High quality ultra thin CVD HfO_2 gate stack with poly-Si gate electrode," in *International Electron Devices Meeting 2000. Technical Digest. IEDM (Cat. No.00CH37138)*, pp. 31–34.

Appendix A

ReaxFF potential functions

ReaxFF is a bond order based force fields that was developed to model chemical reactions, thanks to its ability to determine bonds between atoms on-the-fly during the simulation. In a ReaxFF simulation, the total energy of the system is the sum of two-body, three-body, four-body, long distance interactions as well as correction and system-specific terms:

$$\begin{aligned} E_{system} = E_{bond} + E_{angle} + E_{torsion} + E_{vdW} + E_{Coulomb} \\ + E_{correction} + E_{specific} \end{aligned} \tag{0}$$

Equation (0) can be further decomposed into various energy contributions as shown in Equation (1). The calculation of each potential energy component in Equation (1) is given in subsequent equations.

$$\begin{aligned} E_{system} = E_{bond} + E_{lp} + E_{over} + E_{under} + E_{val} + E_{pen} + E_{coa} \\ + E_{tors} + E_{conj} + E_{H-bond} + E_{C2} + E_{triple} \\ + E_{vdW} + E_{Coulomb} \end{aligned} \tag{1}$$

Bond order and bond energy

In essence, ReaxFF treats the (uncorrected) bond order $BO_{ij}^{'}$ between two atoms as a sum of three bonding components - *sigma*, *pi*, and *double-pi* bonds. These three components are determined solely from the interatomic distance r_{ij} as shown in Equation (2).

$$\begin{aligned} BO_{ij}^{'} &= BO_{ij}^{'\sigma} + BO_{ij}^{'\pi} + BO_{ij}^{'\pi\pi} \\ &= exp\left[p_{bo1}\left(\frac{r_{ij}}{r_0^{\sigma}}\right)^{p_{bo2}}\right] + exp\left[p_{bo3}\left(\frac{r_{ij}}{r_0^{\pi}}\right)^{p_{bo4}}\right] + exp\left[p_{bo5}\left(\frac{r_{ij}}{r_0^{\pi\pi}}\right)^{p_{bo6}}\right] \end{aligned} \tag{2}$$

From the uncorrected bond order $BO_{ij}^{'}$, and over-coordination term $\Delta_i^{'}$ is computed for every atom by taking the difference between the total computed bond order with neighbouring atoms and the number of its valence electrons Val_i (Equation (3a)). For atom types having lone electron pairs, a second over-coordination term $\Delta_i^{'boc}$ is defined in Equation (3b) to provide more flexibility in correcting the bond order.

$$\Delta_i^{'} = \left(\sum_{\substack{j \\ r_{ij} \leq r_{cut}}} BO_{ij}^{'}\right) - \mathrm{Val}_i \tag{3a}$$

$$\Delta_i^{'boc} = \left(\sum_{\substack{j \\ r_{ij} \leq r_{cut}}} BO_{ij}^{'}\right) - \mathrm{Val}_i^{boc} \tag{3b}$$

Then, the corrected bond order BO_{ij} between a pair of atoms is computed from a series of equations (4a) - (4f).

$$\begin{aligned} BO_{ij}^{\sigma} &= BO_{ij}^{'\sigma} \cdot f_1(\Delta_i^{'}, \Delta_j^{'}) \cdot f_4(\Delta_i^{'}, BO_{ij}^{'}) \cdot f_5(\Delta_j^{'}, BO_{ij}^{'}) \\ BO_{ij}^{\pi} &= BO_{ij}^{'\pi} \cdot [f_1(\Delta_i^{'}, \Delta_j^{'})]^2 \cdot f_4(\Delta_i^{'}, BO_{ij}^{'}) \cdot f_5(\Delta_j^{'}, BO_{ij}^{'}) \\ BO_{ij}^{\pi\pi} &= BO_{ij}^{'\pi\pi} \cdot [f_1(\Delta_i^{'}, \Delta_j^{'})]^2 \cdot f_4(\Delta_i^{'}, BO_{ij}^{'}) \cdot f_5(\Delta_j^{'}, BO_{ij}^{'}) \\ BO_{ij} &= BO_{ij}^{\sigma} + BO_{ij}^{\pi} + BO_{ij}^{\pi\pi} \end{aligned} \tag{4a}$$

$$f_1(\Delta_i^{'}, \Delta_j^{'}) = \frac{1}{2}\left[\frac{Val_i + f_2(\Delta_i^{'}, \Delta_j^{'})}{Val_i + f_2(\Delta_i^{'}, \Delta_j^{'}) + f_3(\Delta_i^{'}, \Delta_j^{'})} + \frac{Val_j + f_2(\Delta_i^{'}, \Delta_j^{'})}{Val_j + f_2(\Delta_i^{'}, \Delta_j^{'}) + f_3(\Delta_i^{'}, \Delta_j^{'})}\right] \tag{4b}$$

$$f_2(\Delta_i^{'}, \Delta_j^{'}) = \exp\left(-p_{boc1} \cdot \Delta_i^{'}\right) + \exp\left(-p_{boc1} \cdot \Delta_j^{'}\right) \tag{4c}$$

$$f_3(\Delta_i^{'}, \Delta_j^{'}) = -\frac{1}{p_{boc2}} \ln\left\{\frac{1}{2}\left[\exp\left(-p_{boc2} \cdot \Delta_i^{'}\right) + \exp\left(-p_{boc2} \cdot \Delta_j^{'}\right)\right]\right\} \tag{4d}$$

$$f_4(\Delta_i^{'}, BO_{ij}^{'}) = \frac{1}{1 + \exp\left\{-p_{boc3}\left[p_{boc4} \cdot (BO_{ij}^{'})^2 - \Delta_i^{'boc}\right] + p_{boc5}\right\}} \tag{4e}$$

$$f_5(\Delta_j^{'}, BO_{ij}^{'}) = \frac{1}{1 + \exp\left\{-p_{boc3}\left[p_{boc4} \cdot (BO_{ij}^{'})^2 - \Delta_j^{'boc}\right] + p_{boc5}\right\}} \tag{4f}$$

The corrected over-coordination term Δ_i can be derived from the corrected bond order BO_{ij} using Equation (5).

$$\Delta_i = \left(\sum_{\substack{j \\ r_{ij} \leq r_{cut}}} BO_{ij}\right) - \mathrm{Val}_i \tag{5}$$

For a bond between every pair of atoms within a cutoff distance, the bonding energy is computed as in Equation (6).

$$E_{bond} = -D_e^{\sigma} \cdot BO_{ij}^{\sigma} \cdot \exp\left\{p_{be1}\left[1 - (BO_{ij}^{\sigma})^{p_{be2}}\right]\right\} - D_e^{\pi} \cdot BO_{ij}^{\pi} - D_e^{\pi\pi} \cdot BO_{ij}^{\pi\pi} \tag{6}$$

Lone-pair energy

In Equation (7), the difference between the total order of all bonds connecting atom i with neighbouring atoms and the number of electrons in the outer shell of atom i is computed. This difference is then used to determine the number of lone electron pairs n_i^{lp} and the lone pair deviation term Δ_i^{lp} as written in Equation (8) and (9), respectively. If the lone pair deviation term is greater than zero, the potential energy of atom i is compensated by a lone pair energy penalty E_{lp} (Equation (10)).

$$\Delta_i^e = \left(\sum_{\substack{j \\ r_{ij} \leq r_{cut}}} BO_{ij}\right) - \mathrm{Val}_i^e \tag{7}$$

$$n_i^{lp} = \left\lfloor \frac{\Delta_i^e}{2} \right\rfloor + \exp\left[-p_{lp1} \left(2 + \Delta_i^e - 2 \cdot \left\lfloor \frac{\Delta_i^e}{2} \right\rfloor \right)^2 \right] \tag{8}$$

$$\Delta_i^{lp} = n_{i,opt}^{lp} - n_i^{lp} \tag{9}$$

$$E_{lp} = \frac{p_{lp2} \cdot \Delta_i^{lp}}{1 + \exp\left(-75 \cdot \Delta_i^{lp}\right)} \tag{10}$$

Over/under-coordination energy

From the corrected over-coordination term Δ_i and the lone pair deviation term Δ_i^{lp}, a more precise correction term for atom i is derived in Equation (11a).

$$\Delta_i^{lpcorr} = \Delta_i - \frac{\Delta_i^{lp}}{1 + p_{ovun3} \cdot \exp\left\{ p_{ovun4} \cdot \left[\sum_{\substack{j \\ r_{ij} \le r_{cut}}} (\Delta_j - \Delta_j^{lp}) \cdot (BO_{ij}^{\pi} + BO_{ij}^{\pi\pi}) \right] \right\}} \tag{11a}$$

If an atom is over-coordinated ($\Delta_i > 0$), an energy penalty E_{over} is imposed on the system (Equation (11b)). In constrast, if an atom is under-coordinated ($\Delta_i < 0$), an energy compensation E_{under} is added to the total potential energy by taking into account the effect of π-bond resonance (Equation (12)).

$$E_{over} = \frac{\left(\sum_{\substack{j \\ r_{ij} \le r_{cut}}} p_{ovun1} \cdot D_e^{\sigma} \cdot BO_{ij} \right)}{\Delta_i^{lpcorr} + Val_i} \cdot \frac{\Delta_i^{lpcorr}}{1 + \exp\left(p_{ovun2} \cdot \Delta_i^{lpcorr}\right)} \tag{11b}$$

$$\begin{aligned} E_{under} = -p_{ovun5} \cdot \frac{1 - \exp\left(p_{ovun6} \cdot \Delta_i^{lpcorr}\right)}{1 + \exp\left(-p_{ovun2} \cdot \Delta_i^{lpcorr}\right)} \\ \cdot \frac{1}{1 + p_{ovun7} \cdot \exp\left\{ p_{ovun8} \cdot \left[\sum_{\substack{j \\ r_{ij} \le r_{cut}}} (\Delta_j - \Delta_j^{lp}) \cdot (BO_{ij}^{\pi} + BO_{ij}^{\pi\pi}) \right] \right\}} \end{aligned} \tag{12}$$

Bond angle energy

Valence angle term

The main contribution to the three-body interactions is evaluated from the valence angle between the central atom j and two adjacent atoms i and k. This valence angle energy term is calculated as in Equation (13a) where Θ_0 denotes the equilibrium angle. Θ_0 depends on the sum of π-bond order SBO of the central atom (Equation (13g)). The term SBO_2 in Equation (13e) is introduced to avoid singularities when $SBO = 0$ or $SBO = 2$.

$$E_{val} = f_7(BO_{ij}) \cdot f_7(BO_{jk}) \cdot f_8(\Delta_j) \cdot \left\{ p_{val1} - p_{val1} \cdot \exp\left[-p_{val2} \cdot (\Theta_0 - \Theta_{ijk})^2 \right] \right\} \quad (13a)$$

$$\begin{aligned} f_7(BO_{ij}) &= 1 - \exp\left[-p_{val3} \cdot (BO_{ij})^{p_{val4}} \right] \\ f_7(BO_{jk}) &= 1 - \exp\left[-p_{val3} \cdot (BO_{jk})^{p_{val4}} \right] \end{aligned} \quad (13b)$$

$$\Delta_j^{angle} = \left(\sum_{\substack{n \\ r_{jn} \le r_{cut}}} BO_{jn} \right) - \mathrm{Val}_j^{angle} \quad (13c)$$

$$f_8(\Delta_j) = p_{val5} - (p_{val5} - 1) \cdot \frac{2 + \exp\left(p_{val6} \cdot \Delta_j^{angle} \right)}{1 + \exp\left(p_{val6} \cdot \Delta_j^{angle} \right) + \exp\left(-p_{val7} \cdot \Delta_j^{angle} \right)} \quad (13d)$$

$$SBO = \left[\sum_{\substack{n \\ r_{jn} \le r_{cut}}} (BO_{jn}^{\pi} + BO_{jn}^{\pi\pi}) \right] + \left[1 - \prod_{\substack{n \\ r_{jn} \le r_{cut}}} (-BO_{jn})^8 \right] \cdot \left(-\Delta_j^{angle} - p_{val8} \cdot n_j^{lp} \right) \quad (13e)$$

$$SBO_2 = \begin{cases} 0 & if \quad SBO \le 0 \\ (SBO)^{p_{val9}} & if \quad 0 < SBO < 1 \\ 2 - (2 - SBO)^{p_{val9}} & if \quad 1 < SBO < 2 \\ 2 & if \quad SBO > 2 \end{cases} \quad (13f)$$

$$\Theta_0 = \pi - \Theta_{0,0} \cdot \{1 - \exp\left[-p_{val10} \cdot (2 - SBO_2) \right]\} \quad (13g)$$

Penalty term

For configurations in which two double bonds share the same central atom, a penalty energy term E_{pen} is deduced from the system to improve the stability of the system (Equation (14a)).

$$E_{pen} = p_{pen1} \cdot f_9(\Delta_j) \cdot \exp\left[-p_{pen2} \cdot (BO_{ij} - 2)^2\right] \cdot \exp\left[-p_{pen2} \cdot (BO_{jk} - 2)^2\right] \tag{14a}$$

$$f_9(\Delta_j) = \frac{2 + \exp\left(-p_{pen3} \cdot \Delta_j\right)}{1 + \exp\left(-p_{pen3} \cdot \Delta_j\right) + \exp\left(p_{pen4} \cdot \Delta_j\right)} \tag{14b}$$

Three-body conjugation term

The three-body conjugation energy E_{coa}, given in Equation (15), is a special term added to correctly describe the stability of systems containing $-NO_2$ groups.

$$\begin{aligned} E_{coa} = p_{coa1} \cdot & \frac{1}{1 + \exp\left(p_{coa2} \cdot \Delta_j^{angle}\right)} \\ & \cdot \exp\left\{-p_{coa3} \cdot \left[-BO_{ij} + \left(\sum_{\substack{n \\ r_{in} \leq r_{cut}}} BO_{in}\right)\right]^2\right\} \\ & \cdot \exp\left\{-p_{coa3} \cdot \left[-BO_{jk} + \left(\sum_{\substack{n \\ r_{kn} \leq r_{cut}}} BO_{kn}\right)\right]^2\right\} \\ & \cdot \exp\left[-p_{coa4} \cdot (BO_{ij} - 1.5)^2\right] \cdot \exp\left[-p_{coa4} \cdot (BO_{jk} - 1.5)^2\right] \end{aligned} \tag{15}$$

Torsion angle energy

Rotation barrier term

Equation (16a) - (16c) show the computation of four-body interactions in a dihedral angle, where V_1, V_2, and $V3$ are torsional barrier angles.

$$\begin{aligned} E_{tors} = & f_{10}(BO_{ij}, BO_{jk}, BO_{kl}) \cdot \sin\Theta_{ijk} \cdot \sin\Theta_{jkl} \\ & \cdot \left\{ \frac{1}{2} V_1 \cdot (1 + \cos\omega_{ijkl}) \right. \\ & + \frac{1}{2} V_2 \cdot \exp\left[p_{tor1} \cdot (BO_{jk}^{\pi} - 1 + f_{11}(\Delta_j, \Delta_k))^2 \right] \cdot (1 - \cos 2\omega_{ijkl}) \\ & \left. + \frac{1}{2} V_3 \cdot (1 + \cos 3\omega_{ijkl}) \right\} \end{aligned} \tag{16a}$$

$$\begin{aligned} f_{10}(BO_{ij}, BO_{jk}, BO_{kl}) = & \left[1 - \exp\left(-p_{tor2} \cdot BO_{ij}\right)\right] \\ & \cdot \left[1 - \exp\left(-p_{tor2} \cdot BO_{jk}\right)\right] \\ & \cdot \left[1 - \exp\left(-p_{tor2} \cdot BO_{kl}\right)\right] \end{aligned} \tag{16b}$$

$$f_{11}(\Delta_j, \Delta_k) = \frac{2 + \exp\left[-p_{tor3} \cdot \left(\Delta_j^{angle} + \Delta_k^{angle}\right)\right]}{1 + \exp\left[-p_{tor3} \cdot \left(\Delta_j^{angle} + \Delta_k^{angle}\right)\right] + \exp\left[p_{tor4} \cdot \left(\Delta_j^{angle} + \Delta_k^{angle}\right)\right]} \tag{16c}$$

Four-body conjugation term

Equation (17a) and (17b) describe the additional energy term when successive bonds have the same order of 1.5 as seen in aromatic molecules.

$$E_{conj} = f_{12}(BO_{ij}, BO_{jk}, BO_{kl}) \cdot p_{cot1} \cdot \left[1 + \left(\cos^2\omega_{ijkl} - 1\right) \cdot \sin\Theta_{ijk} \cdot \sin\Theta_{jkl}\right] \tag{17a}$$

$$f_{12}(BO_{ij}, BO_{jk}, BO_{kl}) = \exp\left[-p_{cot2} \cdot \left(BO_{ij} - \frac{3}{2}\right)^2\right] \cdot \exp\left[-p_{cot2} \cdot \left(BO_{jk} - \frac{3}{2}\right)^2\right] \cdot \exp\left[-p_{cot2} \cdot \left(BO_{kl} - \frac{3}{2}\right)^2\right] \tag{17b}$$

Hydrogen bond energy

Hydrogen bonds are extremely necessary in describing the inter-molecular forces when a molecule consists of H atoms bonded to atoms with large electronegativity, such as O, F, or Cl. Hydrogen bonds energy in a $X - \mathrm{H} \cdot Z$ system is computed as in Equation (18).

$$E_{H-bond} = p_{hb1} \cdot \left[1 - \exp\left(p_{hb2} \cdot BO_{\mathrm{XH}}\right)\right] \cdot \exp\left[p_{hb3}\left(\frac{r_0^{hb}}{r_{\mathrm{HZ}}} + \frac{r_{\mathrm{HZ}}}{r_0^{hb}} - 2\right)\right] \cdot \sin^8\left(\frac{\Theta_{\mathrm{XHZ}}}{2}\right) \tag{18}$$

C2 correction energy

E_{C2} is a correction term added to destabilise C_2 molecules since ReaxFF erroneously overestimates the strength of the triple bond between two carbon atoms.

$$E_{C2} = \begin{cases} k_{c2} \cdot \left[BO_{ij} - \Delta_i - 0.04 \cdot (\Delta_i)^4 - 3\right]^2 & if \quad BO_{ij} - \Delta_i - 0.04 \cdot (\Delta_i)^4 > 3 \\ 0 & if \quad BO_{ij} - \Delta_i - 0.04 \cdot (\Delta_i)^4 \leq 3 \end{cases} \tag{19}$$

Triple-bond correction energy

E_{trip} is a correction term added to enhance the triple bond's strength in a CO molecule, making it very stable and inert.

$$E_{trip} = p_{trip1} \cdot \exp\left[-p_{trip2} \cdot (BO_{ij} - 2.5)^2\right] \cdot \frac{\exp\left\{-p_{trip4} \cdot \left[\left(\sum_{\substack{n \\ r_{in} \leq r_{cut}}} BO_{in}\right) - BO_{ij}\right]\right\} + \exp\left\{-p_{trip4} \cdot \left[\left(\sum_{\substack{n \\ r_{jn} \leq r_{cut}}} BO_{jn}\right) - BO_{ij}\right]\right\}}{1 + 25 \cdot \exp\left[p_{trip3} \cdot (\Delta_i + \Delta_j)\right]} \tag{20}$$

Non-bonded interactions

Apart from bonded interactions, potential energy between non-bonded pairs are also computed in ReaxFF. It includes repulsive forces due to Pauli exclusion principle when two atoms get close to each other, attractive forces due to dispersion at long distances, and electrostatic forces between partially charged bodies. All these terms are represented by van der Waals energy term E_{vdW} (Equation (23a)) and Coulomb energy term $E_{Coulomb}$ (Equation (24)).

To avoid discontinuities when particles enter or leave the cutoff radius, a taper function is introduced with its coefficients carefully designed, as shown in Equation (21) and (22).

$$Tap = Tap_7 \cdot r_{ij}^7 + Tap_6 \cdot r_{ij}^6 + Tap_5 \cdot r_{ij}^5 + Tap_4 \cdot r_{ij}^4 + Tap_3 \cdot r_{ij}^3 + Tap_2 \cdot r_{ij}^2 + Tap_1 \cdot r_{ij} + Tap_0 \tag{21}$$

$$\begin{cases} Tap_7 = {}^{20}/_{R_{cut}^7} \\ Tap_6 = {}^{-70}/_{R_{cut}^6} \\ Tap_5 = {}^{84}/_{R_{cut}^5} \\ Tap_4 = {}^{-35}/_{R_{cut}^4} \\ Tap_3 = 0 \\ Tap_2 = 0 \\ Tap_1 = 0 \\ Tap_0 = 1 \end{cases} \tag{22}$$

van der Waals interactions

$$E_{vdW} = Tap \cdot D_{ij} \cdot \left\{ \exp\left[\alpha_{ij} \cdot \left(1 - \frac{f_{13}(r_{ij})}{r_{vdW}}\right)\right] - 2 \cdot \exp\left[\frac{1}{2} \cdot \alpha_{ij} \cdot \left(1 - \frac{f_{13}(r_{ij})}{r_{vdW}}\right)\right]\right\} \tag{23a}$$

$$f_{13}(r_{ij}) = \left[r_{ij}^{p_{vdW1}} + \left(\frac{1}{\gamma_{vdW}}\right)^{p_{vdW1}}\right]^{1/p_{vdW1}} \tag{23b}$$

Coulomb interactions

$$E_{Coulomb} = Tap \cdot C \cdot \frac{q_i \cdot q_j}{\left[r_{ij}^3 + \left(\frac{1}{\gamma_{ij}}\right)^3\right]^{1/3}} \tag{24}$$

Appendix B

ReaxFF parameters for the Si/O/H/Hf/Cl element set

```
   Deposition of HfO2 on Si from HfCl4/H2O (Si/O/H/Hf/Cl) - 2023
39 ! Nr of general parameters
  50.0000 !p_boc1: Overcoordination parameter
   9.5469 !p_boc2: Overcoordination parameter
   1.6725 !p_coa2: Valency angle conjugation parameter
   1.7224 !p_trip4: Triple bond stabilisation parameter
   6.8702 !p_trip3: Triple bond stabilisation parameter
  60.4850 !k_c2: C2-correction
   1.0588 !p_ovun6: Undercoordination parameter
   4.6000 !p_trip2: Triple bond stabilisation parameter
  12.1176 !p_ovun7: Undercoordination parameter
  13.3056 !p_ovun8: Undercoordination parameter
 -70.5044 !p_trip1: Triple bond stabilisation parameter
   0.0000 !swa: Lower Taper-radius
  10.0000 !R_cut: Upper Taper-radius
   2.8793 !Not used
  33.8667 !p_val6: Valency undercoordination
   6.0891 !p_lp1: Valency angle/lone pair parameter
   1.0563 !p_val9: Valency angle
   2.0384 !p_val10: Valency angle parameter
   6.1431 !Not used
   6.9290 !p_pen2: Double bond/angle parameter
   0.3989 !p_pen3: Double bond/angle parameter: overcoord
   3.9954 !p_pen4: Double bond/angle parameter: overcoord
  -2.4837 !Not used
```

```
   5.7796 !p_tor2: Torsion/BO parameter
  10.0000 !p_tor3: Torsion overcoordination
   1.9487 !p_tor4: Torsion overcoordination
  -1.2327 !Not used
   2.1645 !p_cot2: Conjugation
   1.5591 !p_vdW1: van de Waals shielding
   0.1000 !cutoff: Cutoff for bond order (*100)
   1.7602 !p_coa4: Valency angle conjugation parameter
   0.6991 !p_ovun4: Overcoordination parameter
  50.0000 !p_ovun3: Overcoordination parameter
   1.8512 !p_val8: Valency/lone pair parameter
   0.5000 !Not used
  20.0000 !Not used
   5.0000 !Molecular energy (not used)
   0.0000 !Molecular energy (not used)
   0.7903 !p_coa3: Valency angle conjugation parameter
 5 ! Nr of atoms; r_0^sigma;Val_i;atomic mass;r_vdW;D_ij;gammaEEM;r_0^pi;Val_i^e
                  alpha_ij;gamma_w;Val_i^angle;p_ovun5;n.u.;chiEEM;etaEEM;n.u.
                  r_0^pipi;p_lp2;heat increment;p_boc4;p_boc3;p_boc5;n.u.;n.u.
                  p_ovun2;p_val3;n.u.;Val_i^boc;p_val5;n.u.;n.u.;n.u.
Cl   1.6477   1.0000  35.4500   2.2422   0.2846   0.3500  -1.0000   7.0000
    13.5146  10.1330   1.0000   0.0000   0.0000  10.0000   6.0649   2.0000
    -1.0000   2.0165 143.1770   6.2293   5.2294   0.1542   0.8563   0.0000
   -10.2080   2.9867   1.0338   6.2998   2.5791   0.0000   0.0000   0.0000
H    0.5663   1.0000   1.0080   1.1516   0.0881   0.8203  -0.1000   1.0000
     9.6259  33.2894   1.0000   0.0000 121.1250   3.7248   9.6093   1.0000
    -0.1000   0.0000  55.1878   3.0408   2.4197   0.0003   1.0698   0.0000
   -19.4571   4.2733   1.0338   1.0000   2.8793   0.0000   0.0000   0.0000
Hf   2.3136   4.0000 178.4900   2.4158   0.3925   1.0000  -1.0000   4.0000
    11.0252  50.0000   4.0000  -5.0000   0.0000  -0.8117   6.7682   0.0000
    -1.0000   0.0000 143.1770  49.4453   0.3333   0.0000   0.8563   0.0000
    -2.9768   3.5000   1.0338   8.0000   2.2632   0.0000   0.0000   0.0000
O    1.2165   2.0000  15.9990   2.3354   0.1030   1.0898   1.1373   6.0000
    11.8167  13.8449   4.0000  37.5000 116.0768   8.5000   8.3122   2.0000
     0.9049   0.4056  68.0152   3.5027   0.7640   0.0021   0.9745   0.0000
    -3.5500   2.9000   1.0493   4.0000   2.9225   0.0000   0.0000   0.0000
Si   2.0175   4.0000  28.0600   2.0473   0.1835   0.6587   0.9641   4.0000
    12.3588   1.2523   4.0000  21.7115 139.9309   2.4081   6.4081   0.0000
    -1.0000   0.0000 128.2031   8.7895  23.9298   0.8381   0.8563   0.0000
    -4.7525   2.1607   1.0338   6.2998   2.5791   0.0000   0.0000   0.0000
15 ! Nr of bonds; D_e^sigma;D_e^pi;D_e^pipi;p_be1;p_bo5;13corr;p_bo6;p_ovun1
                  p_be2;p_bo3;p_bo4;n.u.;p_bo1;p_bo2;n.u.;n.u.
```

```
 1  1   0.2500   0.0000   0.0000   0.1803  -0.2000   0.0000  16.0000   0.3356
        0.9228  -0.2000  15.0000   1.0000  -0.1178   5.6715   0.0000   0.0000
 1  2 158.1442   0.0000   0.0000  -0.4971  -0.2000   0.0000  16.0000   1.2524
        6.5464  -0.2000  15.0000   1.0000  -0.1758   4.9825   0.0000   0.0000
 1  3  77.0704   0.0000   0.0000  -1.9742  -0.2000   0.0000  16.0000   0.8400
        0.3447  -0.2000  15.0000   1.0000  -0.1061   7.4054   0.0000   0.0000
 1  4   0.0000   0.0000   0.0000   0.5000  -0.2000   0.0000  16.0000   0.5000
        1.0001  -0.2000  15.0000   1.0000  -0.1000  10.0000   0.0000   0.0000
 1  5   0.0000   0.0000   0.0000  -0.6307  -0.2000   0.0000  16.0000   0.5805
        0.6328  -0.2000  15.0000   1.0000  -0.0608   8.5378   0.0000   0.0000
 2  2 136.3025   0.0000   0.0000  -0.5315   0.0000   1.0000   6.0000   0.4220
        5.6971   1.0000   0.0000   1.0000  -0.1067   4.9745   0.0000   0.0000
 2  3   0.0000   0.0000   0.0000  -0.2872  -0.3000   1.0000  36.0000   0.0082
        1.7973  -0.2500  20.0000   1.0000  -0.2578   6.5219   1.0000   0.0000
 2  4 170.9685   0.0000   0.0000  -0.1998   0.0000   1.0000   6.0000   0.1772
        0.3703   1.0000   0.0000   0.0000  -0.0713   3.6534   0.0000   0.0000
 2  5 305.3099   0.0000   0.0000  -2.4945   0.0000   1.0000   6.0000   0.7559
       10.0949   1.0000   0.0000   1.0000  -0.0619   4.3886   0.0000   0.0000
 3  3  65.8247   0.0000   0.0000  -0.6871  -0.2000   0.0000  16.0000   0.3072
        2.7169  -0.2000  15.0000   1.0000  -0.0799   5.8662   0.0000   0.0000
 3  4 202.3617   0.0000   0.0000   1.2468  -0.3000   0.0000  36.0000   0.0120
        0.2392  -0.2000  15.0000   1.0000  -0.2211   4.5049   0.0000   0.0000
 3  5 159.5204   0.0000   0.0000  -0.4655  -0.2000   0.0000  16.0000   0.6024
       11.6794  -0.2000  15.0000   1.0000  -0.1108   4.0729   0.0000   0.0000
 4  4 172.8659 172.0210  50.8293   0.2506  -0.1000   1.0000  29.7503   0.6051
        0.3451  -0.0819   8.3259   1.0000  -0.1456   5.3821   1.0000   0.0000
 4  5 244.0393  42.7900  43.3991  -0.5725  -0.3000   1.0000  36.0000   0.6670
        8.9222  -0.9893  26.7413   1.0000  -0.1438   7.8645   1.0000   0.0000
 5  5  78.0276  54.0531  30.0000   0.5398  -0.3000   1.0000  16.0000   0.0476
        0.2865  -0.8055   7.1248   1.0000  -0.0681   8.6957   0.0000   0.0000
10 ! Nr of off-diagonal terms; D_ij;r_vdW;alpha_ij;r_0^sigma;r_0^pi;r_0^pipi
 1  2   0.1700   1.1950  11.3621   1.4349  -1.0000  -1.0000
 1  3   0.1585   1.8050  13.9224   2.2900  -1.0000  -1.0000
 1  4   0.1026   1.6635  12.0379  -1.0000  -1.0000  -1.0000
 1  5   0.1964   3.8864   6.9564   1.0505  -1.0000  -1.0000
 2  3   0.1464   2.2181  10.6772   0.0036  -1.0000  -1.0000
 2  4   0.0367   1.1322  12.3779   0.6158  -1.0000  -1.0000
 2  5   0.0629   1.2607  13.7341   0.9890  -1.0000  -1.0000
 3  4   0.1607   1.6222  13.2211   1.7478  -1.0000  -1.0000
 3  5   0.3774   1.9810   8.7486   0.9748  -1.0000  -1.0000
 4  5   0.1481   2.0087  11.4016   1.6240   0.6583  -1.0000
27 ! Nr of angles; Theta_0,0;p_val1;p_val2;p_coa1;p_val7;p_pen1;p_val4
```

```
2  4  2  81.9740  13.3675   2.8802   0.0000   1.7194   0.0000   2.1667
3  3  3   0.0000   0.0000   0.0000   0.0000   0.0000   0.0000   0.0000
1  3  1  84.8493  25.4968   0.6325   0.0000   1.8148   0.0000   2.1840
1  3  4  86.5378  15.4031   3.0788   0.0000   0.1012   0.0000   1.6302
4  3  4  39.4039   5.9356   2.5017   0.0000   0.3847   0.0000   0.9076
3  4  3  57.7712   6.8540   4.7040   0.0000   2.4847   0.0000   1.3442
1  2  4 107.2667  28.5579   4.5987   0.0000   1.6114   0.0000   0.9400
3  1  3  45.3873  48.6972   1.8840   0.0000   0.0952   0.0000   0.5118
2  2  2   0.0000  27.9213   5.8635   0.0000   0.0000   0.0000   1.0400
2  2  4   0.0000   5.5977   4.1450   0.0000   0.0000   0.0000   1.0489
4  2  4   0.0000  15.0000   2.8900   0.0000   0.0000   0.0000   2.8774
2  4  4  75.6935  50.0000   2.0000   0.0000   1.0000   0.0000   1.1680
4  4  4  80.7324  30.4554   0.9953   0.0000   1.6310  50.0000   1.0783
2  4  3 143.4851  22.0933   4.2136   0.0000   3.2587   0.0000   1.2977
2  4  5  38.3583  10.0310   3.8265   0.0000   1.8383   0.0000   0.4498
4  4  5  85.4020  18.1749   1.2713   0.0000   2.6177   0.0000   1.0400
5  4  5  39.8239   1.2281   0.2412   0.0000   3.7260   0.0000   1.0400
2  5  2  76.2323   8.3975   4.6282   0.0000   4.0000   0.0000   1.8201
2  5  4  63.6178  19.8129   5.4458   0.0000   0.5983   0.0000   1.0400
2  5  5  68.3958  25.8266   1.6195   0.0000   0.0100   0.0000   1.0000
4  5  4  78.2491  11.8348   0.1760   0.0000   0.4141   0.0000   1.0400
4  5  5  62.7869  22.7434   0.9688   0.0000   3.5470   0.0000   1.0400
5  5  5  71.0490  32.4076   1.2648   0.0000   0.0133   0.0000   1.2899
3  4  5  39.8239   1.2281   0.2412   0.0000   3.7260   0.0000   1.0400
2  1  2  64.4004  29.0673   7.1444   0.0000   1.0833   0.0000   0.6199
1  2  2   0.0000  12.5125   1.7451   0.0000   0.0000   0.0000   1.2995
1  2  1 119.1771  22.2363   3.1806   0.0000   1.0497   0.0000   0.8069
5 ! Nr of torsions; V_1;V_2;V_3;p_tor1;p_cot1;n.u.;n.u.
2  5  5  2   0.0000   0.0000   0.0640  -2.4426   0.0000   0.0000   0.0000
2  5  5  5   0.0000   0.0000   0.1587  -2.4426   0.0000   0.0000   0.0000
2  4  4  2   2.2500  -6.2288   1.0000  -2.6189  -1.0000   0.0000   0.0000
2  4  4  4   0.4723 -12.4144  -1.0000  -2.5000  -1.0000   0.0000   0.0000
4  4  4  4  -2.5000 -25.0000   1.0000  -2.5000  -1.0000   0.0000   0.0000
3 ! Nr of hydrogen bonds; r_hb^0;p_hb1;p_hb2;p_hb3
4  2  4   2.1200  -3.5800   1.4500  19.5000
1  2  4   2.4000  -0.8644   1.4500  19.5000
4  2  1   1.8437  -4.0000   1.4500  19.5000
```

Appendix C

Sentaurus Device parameters

```
#define ParFileDir .

Material="TiN" {
  #includeext "ParFileDir/TiN.par"

  BarrierTunneling "GOX" {
    mt = 1.0, 1.0
  }
}

Material="HfO2" {
  #includeext "ParFileDir/HfO2.par"

  Epsilon {
    epsilon = 18.9 # [1]
  }

  Epsilon_Inf {
    epsilon_inf = 4.33 # [1]
  }

  Epsilon_aniso {
    epsilon = 18.9 # [1]
  }
```

```
  Epsilon_Inf_aniso {
    epsilon_inf = 4.33 # [1]
  }

  Bandgap {
    Chi0 = 2.05 # [eV]
    Eg0 = 5.7 # [eV]
  }

  eDOSMass {
    mm = 0.11 # [1]
  }

  BarrierTunneling "GOX" {
    mt = 0.11, 1.00
  }
}

Material="Si3N4" {
  #includeext "ParFileDir/Si3N4.par"
}

Material="SiO2" {
  #includeext "ParFileDir/SiO2.par"

  BarrierTunneling "GOX" {
    mt = 0.50, 0.77
  }
}

Material="Silicon" {
  #includeext "ParFileDir/Silicon.par"

  BarrierTunneling "GOX" {
    mt = 0.19, 0.16
  }
}
```